Multiwavelength Observations of Solar Magnetic Phenomena and Particle Acceleration

A dissertation submitted to the University of Dublin for the degree of *Philosophæ Doctor (PhD)*

Brendan P. Clarke
Trinity College Dublin, August 2022

DIAS
Institiúid Ard-Léinn Bhaile Átha Cliath | Dublin Institute for Advanced Studies

Trinity College Dublin
Coláiste na Tríonóide, Baile Átha Cliath
The University of Dublin

Declaration

I declare that this thesis has not been submitted as an exercise for a degree at this or any other university and it is entirely my own work.

I agree to deposit this thesis in the University's open access institutional repository or allow the library to do so on my behalf, subject to Irish Copyright Legislation and Trinity College Library conditions of use and acknowledgement.

Name: Brendan Clarke

Signature: ..... **Date:** .....

Summary

The solar magnetic field is instrumental in controlling the dynamics and topology of all coronal phenomena. The magnetic flux we observe varies by a factor of $\sim$8 over a twenty-two year cycle causing a modulation in the Sun's radiation output over a broad range of wavelengths. This variation is a consequence of the evolution of the solar magnetic field from a poloidal magnetic configuration to a toroidal field produced due to the influence of differential rotation.

Energetic events such as solar flares and coronal mass ejections (CMEs) are produced when this magnetic energy is released from the Sun's atmosphere in the form of thermal and kinetic energy. Modern instrumentation has allowed us to conduct detailed studies of these events. However, many questions remain unanswered. In this work, a range of phenomena associated with particle acceleration in the solar atmosphere are investigated from a multi-wavelength perspective.

Firstly, an analysis of short solar radio bursts, known as S-bursts, is presented. To date, our knowledge of the solar magnetic field is only known in detail at the photosphere based on measurements of the Zeeman splitting of spectral lines. Potential field source surface (PFSS) extrapolations are typically used to estimate the coronal magnetic field. Here, we measure the properties of over 3000 S-bursts and show that S-bursts can be used to remote sense the coronal magnetic field at various altitudes.

Secondly, an M-class solar flare exhibiting pronounced and broadband quasi periodic pulsations (QPPs) in its emission is investigated. QPPs have been studied for several decades, however, their origin remains unknown. Evidence is presented that the mechanism responsible for their generation is oscillatory magnetic reconnection that results in intermittent particle acceleration. This gives rise to QPPs that span in energy from the low frequency radio domain through to the high energy X-ray regime. It is shown that the source of these QPPs originates from near the energy release site of the flare. The QPPs then manifest across vast distances, from the flare footpoints through to interplanetary space. This work shines light onto the nature of energy release in flares.

Finally, analysis of co-observed X-ray and radio data is presented using modern instrumentation. Combining the high cadence data available from The Spectrometer Telescope for Imaging X-rays (STIX) and I-LOFAR provides a unique opportunity to investigate the nature of high energy electrons accelerated during solar flares. It is shown that X-ray photon spectral index correlates with the beam speeds of associated type III radio burst sources. Software that was developed as part of this work is also presented.

For Mum and Dad.

Acknowledgements

Firstly, I'd like to thank my supervisor, Peter Gallagher. I really appreciated him taking me on as a student and for the opportunities I have been granted working with him and his group. His guidance, enthusiasm, and motivation made my experience over the past four years rewarding, exciting, and a positive challenge that I am delighted to have undertaken.

Secondly, I'd like to thank my fellow PhD students throughout the years who provided an invaluable source of camaraderie and whose positivity, work ethic, and encouragement inspired me to keep going. I will no doubt look back fondly on all the great times I had working with the friends I made at Trinity and DIAS. In particular, I'd like to thank Diana Morosan and Laura Hayes for being patient and friendly mentors, as well as friends, who really helped me get my major projects going. To Aoife, Ciara, and Pearse, I'm lucky to have traversed the PhD path with you all and I appreciate having had you as supports having gone through the experience together. To all the other members of the Astrophysics Research Group, I am hugely grateful for having been able to work with you.

A sincere thank you to my parents, Ann and Conor, whose continuous love, support, and reassurance made it all possible. To my brother Rob, your patience with me as a broke student and housemate will always be appreciated and I couldn't have gotten through it without you. The many electricity bills will be paid off soon, I promise! Also, a huge thanks to my brother Harry who has always been a great source of encouragement.

Thanks to all my friends who have been so supportive, especially my pals in my band TV People, both past and present, who have given me such an amazing creative outlet outside of the PhD over the last several years. Lastly, thanks to my dog, Ted, who I think really gets it.

List of Publications, Presentations and Contributions

Publications

1. **Brendan P. Clarke**, Diana E. Morosan, Peter T. Gallagher, Vladimir V. Dorovskyy, Alexander A. Konovalenko, & Eoin P. Carley
"Properties and magnetic origins of solar S-bursts",
Astronomy & Astrophysics, 622, A204 (2019)

2. **Brendan P. Clarke**, Laura A. Hayes, Peter T. Gallagher, Shane A. Maloney, & Eoin P. Carley
"Quasi-periodic Particle Acceleration in a Solar Flare",
The Astrophysical Journal, 910(2), 123 (2021)

3. Thomas Long, Shane A. Maloney, **Brendan P. Clarke**, & Peter T. Gallagher
"X-ray and Radio Diagnostics of Accelerated Electrons Using STIX",
The Astrophysical Journal, in prep

Oral Presentations

1. "Properties and Magnetic Origins of Solar S-bursts",
Irish National Astronomy Meeting, Birr, (2018)

2. "Properties and Magnetic Origins of Solar S-bursts",
Community of European Solar Radio Astronomers (CESRA) Summer School, Royal
Observatory of Belgium, (2018)

3. "Remote Sensing the Coronal Magnetic Field using Solar S-Bursts",
49th Young European Radio Astronomers Conference, Trinity College Dublin, (2019)

4. "Evidence for Time-Dependent Magnetic Reconnection from X-ray and Radio Pulsations",
18th RHESSI Workshop, University of Minneaspolis, (2019)

5. "Multi-Wavelength Observations of Solar Magnetic Phenomena Associated with Particle Acceleration ",
Post Graduate Seminar Series, Trinity College Dublin, (2021)

6. “Quasi-Periodic Particle Acceleration in a Solar Flare”,
   238th AAS Meeting - American Astronomical Society, Online, (2021)

7. “Quasi-Periodic Particle Acceleration in a Solar Flare”,
   20th RHESSI Workshop, Online, (2021)

Software Contributions

1. STIXpy - Analysis Software for The Spectrometer Telescope for Imaging X-rays
   Development of Visualisation Package, (2021)

Contents

List of Figures

List of Tables

1

Introduction

Natural curiosity and wonder has been a prime motivation to study astronomy and astrophysics for our entire history. Simply looking up at the stars on a dark night evokes a primal feeling of mystery. It's significant to acknowledge that only a relatively short period of time has elapsed since we had a very primitive understanding of our place in the Universe. Early scientists in ancient Greece believed that the Earth was the centre of the Universe. It wasn't until 1514 that Copernicus discovered that the Earth was not at the centre, and that in fact the planets revolved around the Sun. Our understanding of the scale of the Universe then began to incrementally expand. In 1610, Galileo found that our solar system is part of a larger galaxy, The Milky Way. Hubble, in 1923, then discovered the existent of other galaxies separate to our own.

The following hundred years would lead to the birth of many now established theories. The fact that the Universe is expanding and is perhaps infinite in size, that there are some two trillion galaxies in the observable Universe, and that the Universe was born out of a big bang $\sim$13.8 billion years ago, to name a few. So much has been discovered in such a short period that we have gone from a paradigm in which our humble solar system was of paramount importance, to one in which it is simply a generic system within a generic galaxy in a vast Universe. These ideas and discoveries are extremely exciting and liberating, yet can also be daunting to fathom. My own personal motivation to study astrophysics, and solar physics in particular, is to understand some of these ideas for myself.

Despite the recent and significant progress in our understanding of cosmology, galax-

ies, stars, exoplanets and other cosmic entities, our own star, the Sun, displays many phenomena we are yet to fully understand. Solar physics plays a key role in astrophysics as the proximity of the Sun enables us to study its features in great detail. As we understand the Sun further, we also develop our understanding of similar stars and can extrapolate this knowledge to understand and inform astrophysics in general. This thesis presents new research and results I conducted on the broad topic of solar magnetic phenomena associated with particle acceleration, as well as a thorough introduction to many relevant topics in solar and plasma physics.

In this introductory chapter, the structure and atmosphere of the Sun and the solar magnetic field, which is the driving force behind the spectacular eruptive solar events we observe, is explored. Details of our understanding of solar flares, plasma physics and magnetohydrodynamics (MHD), magnetic reconnection, and relevant associated phenomenology is then provided in the context of multi-wavelength observations associated with particle acceleration. Using combined observations of low frequency radio emission through to extreme ultra violet emission and X-ray emission reveals new and exciting details of the nature of energy release in solar flares and the relationship between the complex suite of emission mechanisms and resulting radiation we see. Finally, this chapter will conclude with an outline of the proceeding sections of this thesis.

1.1 Stars and The Sun

Stars are luminous objects held together by gravity, composed primarily of hydrogen and helium, that are powered by nuclear fusion. In general terms, we describe stars in terms of their observed or inferred physical properties such as their luminosity, effective temperature, spectral class, and mass. A star's luminosity, L, is the total amount of electromagnetic radiation it emits per unit time. A stars luminosity is related to its effective temperature, T_{eff}, via the following equation

$$L = 4\pi R^2 \sigma T_{eff}^4 \tag{1.1}$$

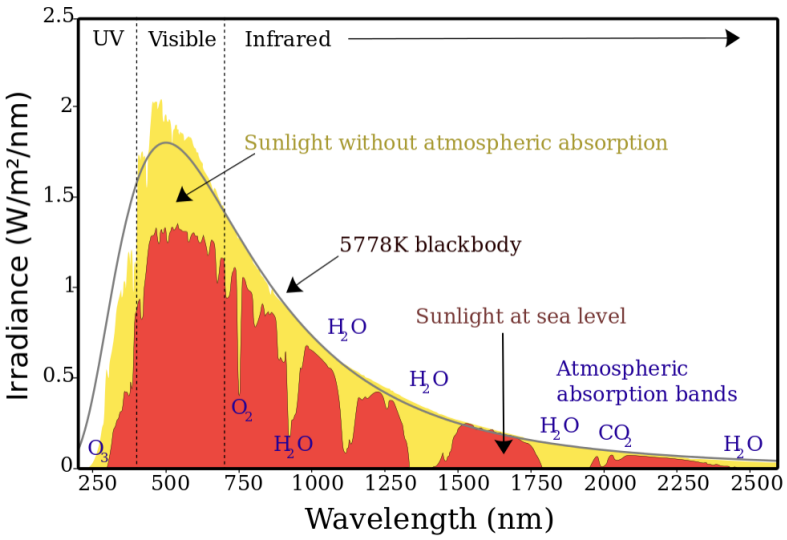

Figure 1.1: The solar radiation spectrum for light at the top of the Earth's atmosphere (yellow region) and at sea level (red region) (Wu et al., 2011). The black curve shows the spectrum of a black body at a temperature of ~ 5778 K. It is clear that a black body is an excellent representation for the solar spectrum. In reality, absorption, scattering, and other effects are at play resulting in differences between the solar spectrum and that of a perfect black body.

where R is the stellar radius and σ is the Stefan-Boltzmann constant. Idealised objects known as black bodies are hypothetical perfect absorbers and radiators of energy. A black body in thermal equilibrium (meaning at a constant temperature) emits black body radiation according to Planck's law. In astronomy, stars are approximated as black bodies in order to estimate their effective temperature via their luminosity. Figure 1.1 shows the spectrum of the Sun and how it closely compares to that of a black body of temperature 5778 K. This approximation provides a powerful tool for measuring the surface temperature of stars. The spectrum of black body radiation is solely dependent upon the temperature of the black body: $j^* = \sigma T^4$. Here, j^* is the total energy radiated per unit surface area. Multiplying this by the surface area of the star gives us the luminosity formula from Equation 1.1.

If we survey many stars and plot their luminosities against their effective temperatures, or equivalently their absolute magnitude versus their spectral type, an important trend is observed that is of great importance to theories of stellar evolution. This graph is known as the Hertzsprung Russell diagram. Figure 1.2 shows this diagram in the

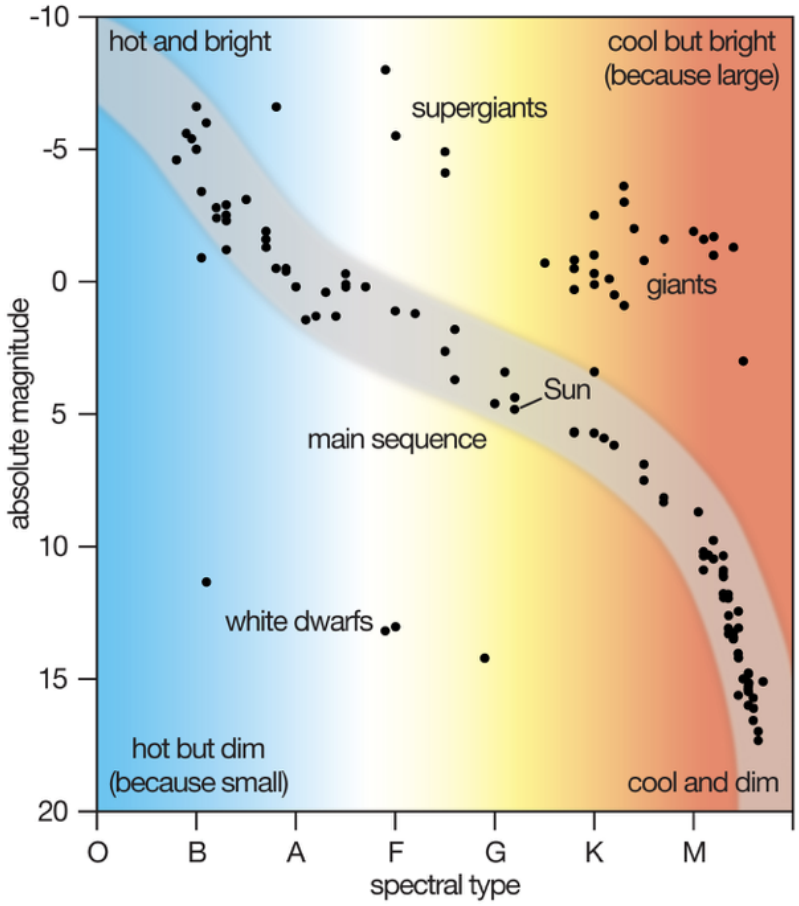

Figure 1.2: Hertzsprung Russell diagram illustrating the relation between the absolute magnitude and spectral type of stars. Taken from Encyclopedia Britannica (https://www.britannica.com/science/Hertzsprung-Russell-diagram).

form of absolute magnitude versus their spectral type. Most stars are located along the grey region, known as the main sequence. The stars in the main sequence are in a stage of their evolution in which they are fusing hydrogen into helium in their cores. Stars spend the majority of their lifetimes on the main sequence region before they evolve. In the case of the Sun, it is currently mid way through its life cycle. Eventually, it will move off the main sequence as it expands and cools to become a red giant, before shrinking in size to become a white dwarf.

The Sun is an average sized star that formed approximately 4.6×10^9 years ago when an accumulation of gas and dust collapsed under the force of gravity. As shown in Figure 1.2, it is located on the main sequence of the Hertzsprung Russell diagram and has spectral type G2 V. It is of course our closest star, whose distance to the Earth is approximately 1.49×10^{11} m (Phillips, 1992). It has a radius of $6.959 \pm 0.007 \times 10^8$ m

and a mass of $1.9889 \pm 0.0003 \times 10^{30}$ kg. The luminosity of the Sun is $3.84 \pm 0.04 \times 10^{26}$ W (Foukal, 2004).

The Sun's source of energy is a consequence of the nuclear fusion of hydrogen at its core, which produces pressure, P, that counterbalances the inward collapsing force of gravity to result in a state of stability known as hyrdostatic equilibrium ($\Delta P = -\rho g$). Here, ρ represents density and g is the acceleration due to gravity. This energy produced at the core eventually manifests in the solar atmosphere where the largest explosions in our solar system, known as solar flares, occur. To understand this process of energy transport, we must first understand the structure of the solar interior and atmosphere in more detail.

1.2 Solar Interior

The radial variation in the temperature and density of the solar interior yield different dominant processes and energy transport mechanisms. The 'standard solar model', or SSM, describes the four regions of the solar interior which comprise of *The Core*, *The Radiative Zone*, *The Tachocline*, and *The Convective Zone*. Figure 1.3 shows profiles of the density and temperature of the core, the radiative zone, and the convective zone as a function of radius (Christensen-Dalsgaard et al., 1996).

1.2.1 The Solar Core

The core of the Sun boasts extremely high temperatures and densities, exceeding even the density of gold by reaching up to 150 $g\ cm^{-3}$ (Basu et al., 2009). It occupies the very central region of the solar interior, up to $\sim 0.25\ R_{\odot}$. These high temperatures, of the order of 10^7 K (Thomas & Weiss, 2004), and densities are sufficient enough to drive the process of nuclear fusion (H $\rightarrow$ He). This is the ultimate source of energy in our solar system.

The extreme conditions in the core provide enough energy for the particles to overcome the Coulomb barrier and undergo a reaction called the proton-proton chain (Davis

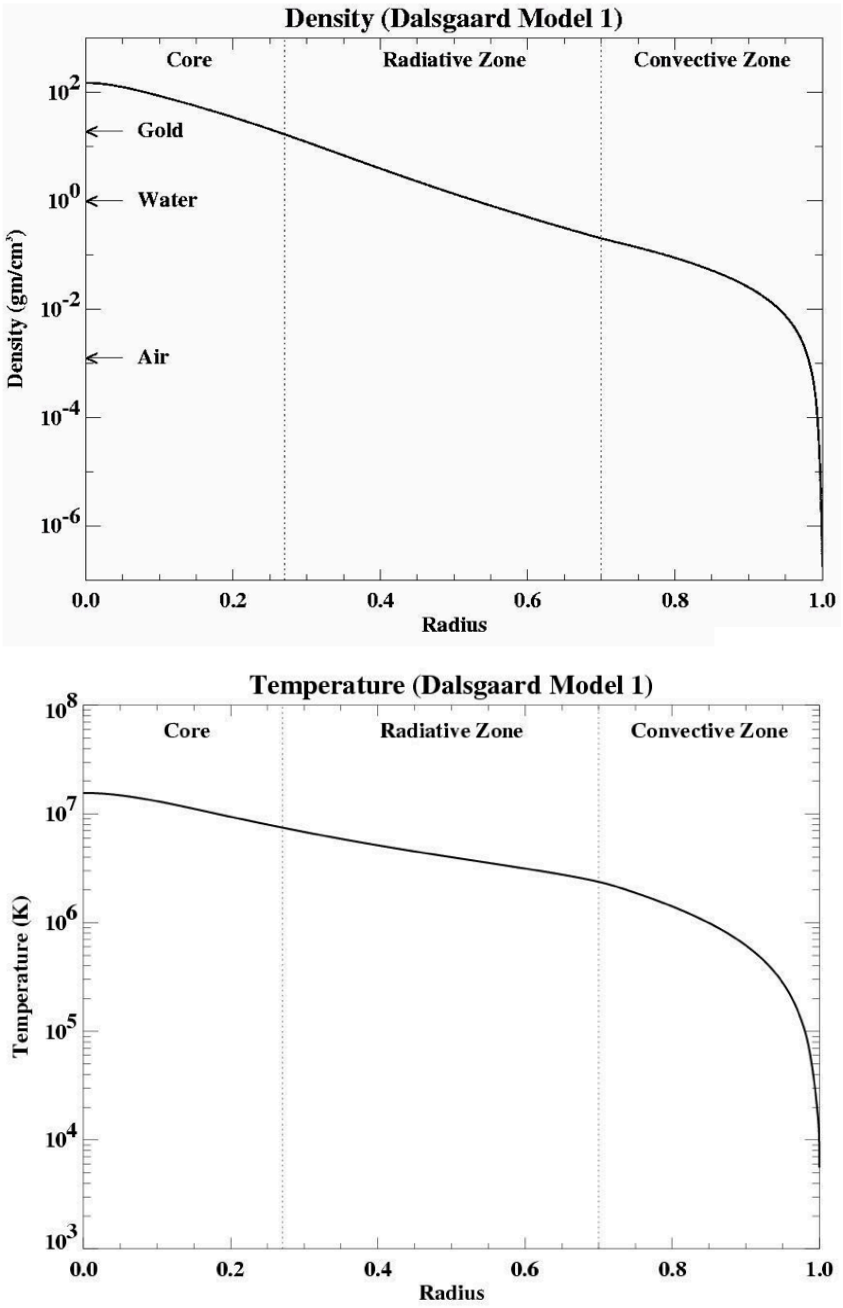

Figure 1.3: Profiles of the density and temperature of the solar interior as a function of radius. One can note the staggeringly high density and temperature of the core, followed by the gradual radial decrease in these properties as we reach the radiative and convective zones closer to the solar surface (Christensen-Dalsgaard et al., 1996).

et al., 1968). Step 1 in this chain involves the fusion of two protons into deuterium, producing a positron, e^+ and an electron neutrino, ν_e.

$$ {}^1_1H + {}^1_1H \rightarrow {}^2_1H + e^+ + \nu_e \tag{1.2}$$

1.44 MeV of energy is then produced in the form of two γ rays when the positron produced in Equation 1.2 annihilates with an electron. In step 2, the newly formed deuterium can then react with a proton resulting in a helium isotope, ${}^{3}_{2}He$.

$$2^{1}_{1}H + {}^{1}_{1}H \rightarrow {}^{3}_{2}He + \gamma \tag{1.3}$$

5.49 MeV of energy is produced during this stage. Step 3 then involves a reaction between two ${}^{3}_{2}He$ to produce a ${}^{4}_{2}He$, meaning that step 1 and step 2 must occur twice before step 3 can take place.

$${}^{3}_{2}He + {}^{3}_{2}He \rightarrow {}^{4}_{2}He + 2^{1}_{1}H \tag{1.4}$$

The entire process can then be summarised as

$$4^{1}_{1}H \rightarrow {}^{4}_{2}He + 2e^{+} + \nu_{e} + 2\gamma. \tag{1.5}$$

The significant outcome of the pp-chain is the liberation of 4.2×10^{12} J of energy in the form of γ-rays that powers the Sun's radiant energy as it travels towards the outer layers of the solar interior.

The discovery that the source of the Sun's energy is most dominantly a consequence of the pp-chain process is attributed to Davis et al. (1968) who carried out the famous neutrino experiments which gave rise to much of our understanding of the nature of the solar core and interior. It was later discovered that in fact $\sim 86\%$ of the fusion reactions occuring in the solar interior are due to the ppI chain (Turck-Chièze & Couvidat, 2011). The temperature profile of the solar interior is shown in Figure 1.3 where we can see the intense temperature of 15.6×10^{6} K that the core reaches due to this fusion process.

The interior zones of the Sun beyond the core are classified by the method through which the majority of energy is transferred. Conduction plays little role in the transfer of energy within the Sun, while convection and radiation are the more dominant processes (Phillips, 1992). Immediately beyond the core, we have the *the radiative*

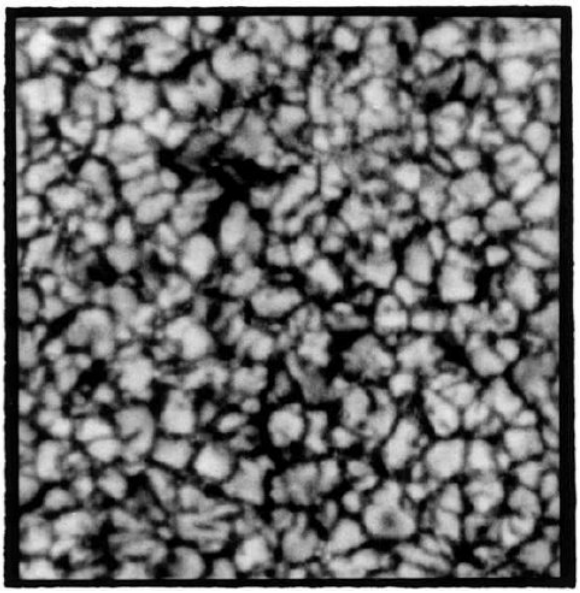

Figure 1.4: Image of the dominant solar surface feature of convection known as granulations, taken from Roudier et al. (1997). The central bright regions show the hot rising plasma while the cooler sinking plasma is visible as the dark intergranular lanes.

zone.

1.2.2 The Radiative Zone & Tachocline

Radiation acts as the dominant energy transport mechanism from 0.25 - 0.7 $R_{\odot}$ (Christensen-Dalsgaard et al., 1996). In this radiative zone, high densities of up to 2×10^4 $g\ cm^{-3}$ cause the photons to scatter off many particles as they diffuse outwards towards the surface in a random walk fashion. Here, the average distance over which such a photon travels before scattering, known as the mean free path, is extremely short with a value of ~ 0.9 cm. As a result, the photons spend 10^5 years on their journey from the radiative zone to the solar surface (Mitalas & Sills, 1992).

A particularly intriguing region of the solar interior is the point of interface between the radiative zone and the convective zone, which is located at $\sim 0.7\ R_{\odot}$. This region, known as the tachocline, is theorised to be the point from which the Sun's dynamo magnetic field generation originates (Thompson et al., 2003). A sudden change in the rotational dynamics of the solar interior, from the solidly rotating radiative zone to the differentially rotating convection zone, is believed to be factor leading to the complexity of the solar magnetic field. Poloidal fields shear in the tachocline and become toroidal

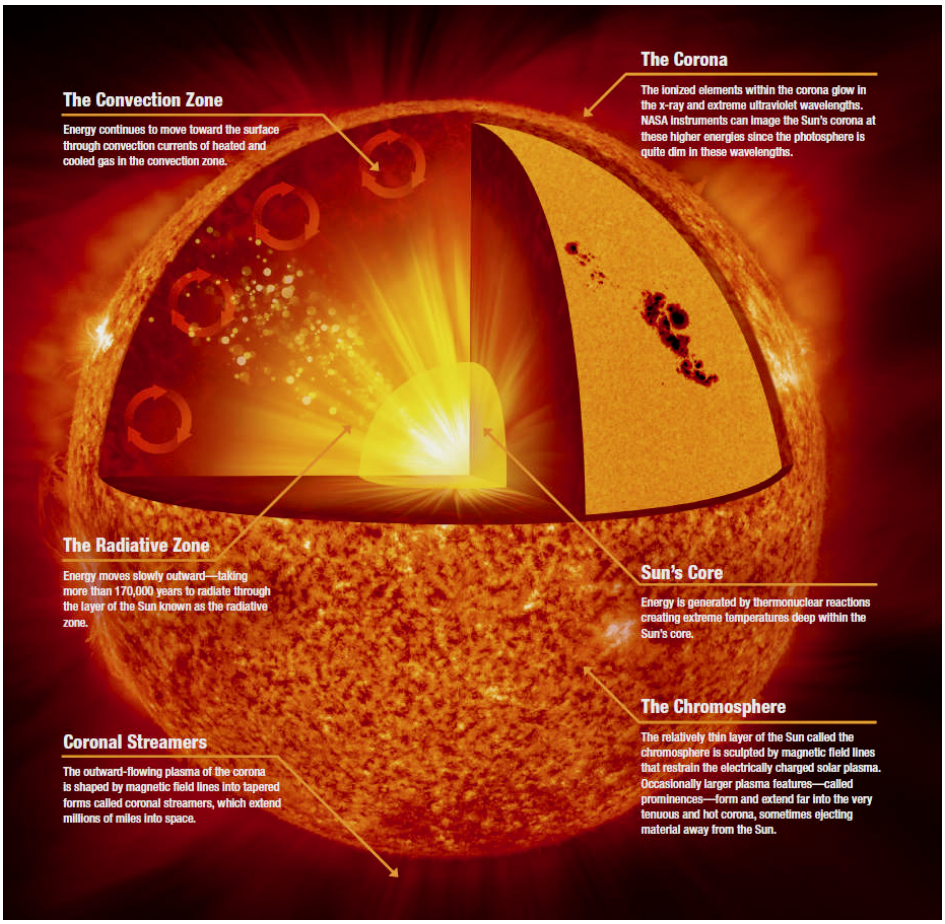

Figure 1.5: Structure of the solar interior and atmosphere (image credit: NASA).

due to this sudden change in rotational dynamics. The interchange between these magnetic states and its relevance to the solar magnetic field is discussed further in Section 1.3.

1.2.3 The Convective Zone

As the distance outward from the core increases and the temperature decreases further, we reach the convective zone. Here, the temperature has fallen to approximately two million degrees kelvin, allowing some heavier nuclei to capture electrons and recombine for longer periods. These optically thick particles obstruct the out-flowing radiation, increasing the opacity of the environment, resulting in the gas becoming more unstable.

The pent up energy then gives rise to a shift in the dominant transfer mechanism of energy from radiation to convection for the outer 28.7 % of the solar interior (Lang, 2001). As the cooler, opaque material at the base of the convective zone heats, it

expands and rises in a convective motion to reach the solar surface in a period of about ten days. It then cools and sinks back down producing the granulations we observe in white light images of the photosphere. The bright centers of the granules are a consequence of the hot up-flowing convective cells of plasma, while the dark edges represent the cooling and descending plasma. Figure 1.4 shows a white light image of this granulation pattern (Roudier et al., 1997).

Much of our knowledge of the properties of the solar interior mentioned above are derived from the study of helioseismology. Helioseismology enables us to probe the solar interior by analysing the effects that sound waves, or acoustic waves, generated within the sun have on our observations of spectral lines in the photosphere. The photosphere and other atmospheric regions of the Sun are discussed in detail in Section 1.4. An image of the structure of the solar interior and atmosphere is displayed in Figure 1.5.

1.3 Solar Magnetic Field

The solar magnetic field is instrumental in controlling the dynamics and topology of all coronal phenomena. As mentioned in Section 1.2.2, It is believed to be generated at the interface between the convective and radiative zones of the solar interior, known as the Tachocline.

Although the details of the origin of the solar magnetic field and its complexity remains an active area of research, it is believed to be generated through a dynamo process. Babcock (1961) provided a general description of this process, which describes the evolution of the solar magnetic field from a simple poloidal dipolar structure to a more complex and partly toroidal configuration over a period of $\sim$11 years (Charbonneau, 2010). The magnetic flux we observe varies by a factor of $\sim$8 over the solar cycle causing a modulation in the Sun's radiation output.

The magnetic cycle of the Sun begins in a simple poloidal configuration aligned to the solar rotation axis. Babcock (1961) describes how the gas pressure dominates the magnetic pressure in the convective zone, resulting in the magnetic field being dragged along with the motion of the plasma. Additionally, at the tachocline we see the onset

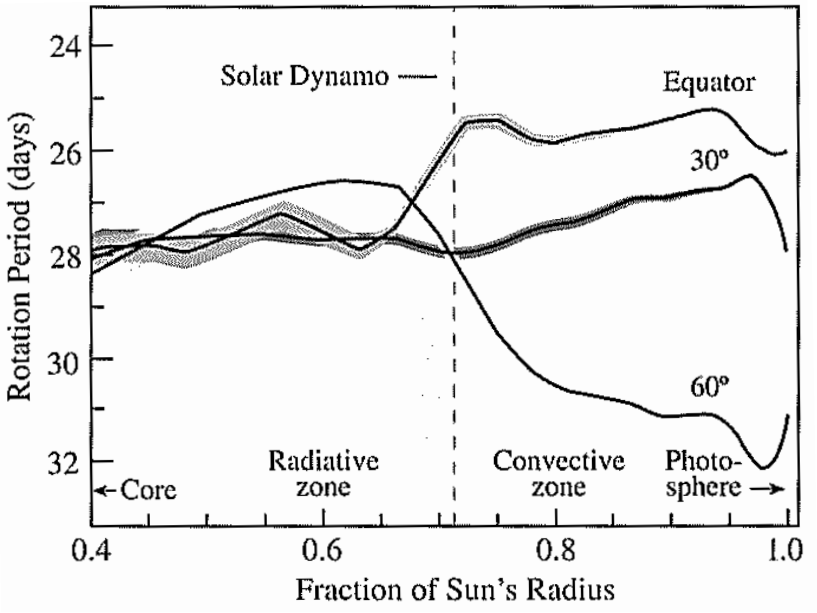

Figure 1.6: The rotation period of the solar interior at latitudes of 0°, 30° and 60° inferred via data obtained by the Michelson Doppler Imager aboard The Solar and Heliospheric Observatory (Lang, 2001).

of differential rotation in the solar interior. Figure 1.6 shows the rotation rate of the solar interior at latitudes of 0°, 30° and 60° inferred via data obtained by the Michelson Doppler Imager aboard The Solar and Heliospheric Observatory (Lang, 2001). Below the tachocline, we see uniform rotation as a function of latitude. Above this zone, we see that higher latitudes rotate slower than those near the equator.

The combined conditions of the magnetic field being *frozen-in* with the motion of the plasma with differential rotation results in the magnetic field slowly deviating from its poloidal state. Shearing motions lead to it becoming wrapped around the solar axis into a toroidal configuration. This is known as the Ω effect.

Figure 1.7a shows a schematic of how the processes mentioned above gives rise to the complexity of the solar magnetic field. The magnetic field winds into twisted structures known as *flux ropes*. As the magnetic field pressure increases, these regions become unstable and rise towards the surface where they manifest observationally in the form of sunspots of opposite polarity. These regions of concentrated flux emergence form magnetically complex structures in the solar atmosphere known as *active regions* which build up large amounts of potential energy. Once established, these active regions can last for many weeks before magnetic interactions result in in catastrophic explosions.

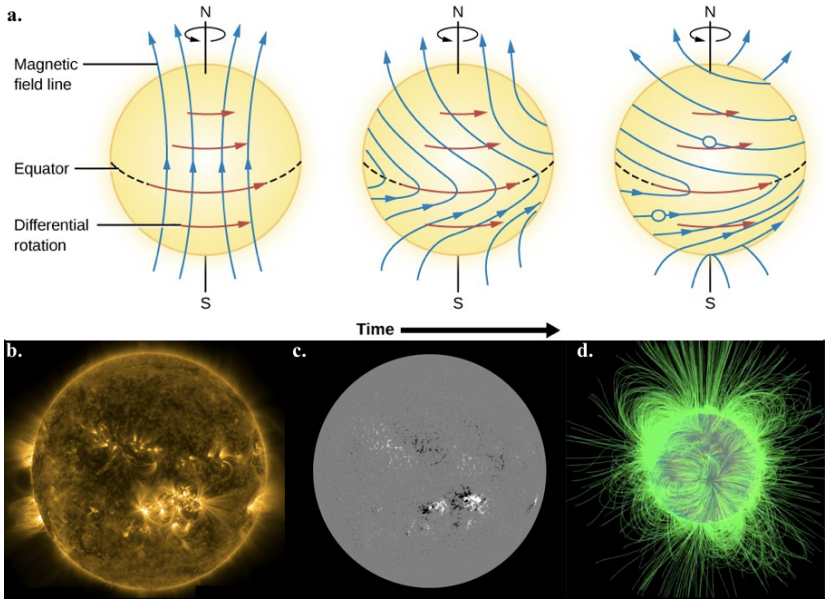

Figure 1.7: (a): The influence of differential rotation and high-β conditions in the convective zone gives rise to the Ω effect. This leads to the formation of concentrated magnetic regions known as active regions. (b): An image of the Sun at extreme ultra violet wavelengths taken by the Atmospheric Imaging Assembly on-board the Solar Dynamics Observatory. Here, we can see a central active region characterised by hot plasma contained within complex coronal loops. (c): The same region as (a) using data from the Helioseismic and Magnetic Imager. This magnetogram conveys the opposite polarities at the footpoints of these loop structures. (d): An example of a potential field source surface extrapolation that uses photospheric magnetic field data to estimate the magnetic field configuration and strength at higher altitudes above the photosphere.

These explosive events we observe in the solar atmosphere, such as flares and coronal mass ejections (CMEs), are the consequence of the release of this large amount of stored magnetic energy.

Coronal loops, which are conduits of heated plasma shaped by the geometry of the twisted flux ropes (Aschwanden, 2005), imaged at extreme ultra violet wavelengths by the Atmospheric Imaging Assembly (AIA) on-board the Solar Dynamics Observatory (SDO) are shown in Figure 1.7b. Figure 1.7c shows a magnetogram of the same region taken by the Helioseismic and Magnetic Imager (HMI) on SDO. The white and black represent the opposite polarities of the magnetic field at the photospheric layer of the Sun's atmosphere, while the absolute pixel value represents the magnetic field strength. It is clear that these loops are rooted in magnetic footpoints of opposite polarity.

Our knowledge of the photospheric magnetic field is mainly based on measurements such as the Zeeman splitting of spectral lines. The strongest fields are observed above

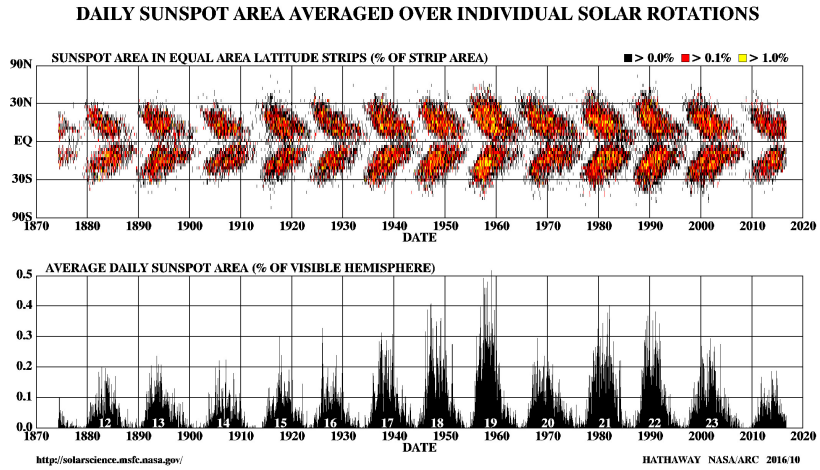

Figure 1.8: Top: The latitude of sunspots as a function of time, The 'butterfly diagram' showing the latitude of sunspots as a function of time during the solar cycle. Bottom: The total area of the sunspots as a percentage of the visible hemisphere of the solar disk. Source: NASA)

sunspots within these active regions where we observe values up to 3000 G (McLean et al., 1978). Above the photosphere, we rely on remote sensing techniques to estimate the strength of the coronal magnetic field (Aschwanden, 2005). Radio and white-Light observations are typically used to do this (Kumari et al., 2017). The coronal magnetic field is typically reconstructed using potential field source surface (PFSS) extrapolations from magnetograms, however, these extrapolations are uncertain due to unknown currents and non-force-free conditions (Schrijver & De Rosa, 2003). A visualisation of such an extrapolation is shown in Figure 1.7d where one can observe both open and closed magnetic field lines; the source regions of the fast and slow solar wind, respectively. Chapter 4 of this thesis presents a new method of remote sensing the coronal magnetic field using short radio bursts known as S-bursts.

At the peak of the magnetic complexity of the 11 year solar cycle, there may be greater than 100 sunspots visible on the solar disk at any time. Figure 1.8 shows the sunspot formation occurring at about 30° latitude at the start of the solar cycle and then migrating towards the equator at the end of the cycle forming the famous butterfly shaped diagram. The bottom panel shows the total area of the sunspots as a percentage of the visible disk.

1.4 The Solar Atmosphere

The Sun is not solid in nature. It is a large mass of incandescent gas and plasma with no solid surface. The density of the material that makes up the Sun simply becomes increasingly tenuous with increasing distance from its centre. In fact, there is extremely diffuse solar material as far out as the Earth and even beyond, to the edge of our solar system. We call the 'surface' of the Sun the photosphere. This is the visible 'sphere of light' we can see in the sky. The photosphere is the first layer of the solar atmosphere and the point at which the Sun has become optically thin to visible radiation, allowing the light to escape and travel into interplanetary space (Lang, 2001). Above the photosphere, the solar atmosphere is further divided into *the chromosphere*, *the transition region*, and *the corona*.

Figure 1.9 displays how the temperature and density of the solar atmosphere varies quite dramatically with distance above the solar surface (Priest, 2014). One can note the extremely rapid and counter-intuitive rise in temperature at the transition region as we reach the Corona. Typically, one would expect temperature to decrease with distance from an energy source. In this case, nuclear fusion is occurring at the solar core and so one would anticipate the outermost region of the solar atmosphere to be cooler than the surface. Understanding the origin and energy source for this temperature change, known as *the coronal heating problem*, remains a contemporary research topic in solar physics and one of the key unsolved elements in our understanding of energy transport in the solar atmosphere. This topic is discussed further in Section 1.4.3.

1.4.1 The Photosphere

The photosphere is the first and most dense layer of the solar atmosphere. Despite its relatively high density, it is in fact so rarefied that we would consider it a vacuum here on Earth, with its pressure being one ten thousandth that of Earth's atmospheric pressure at sea level. The photosphere is extremely thin, with a thickness corresponding to 0.05 % ($\sim$1 Mm) of the Sun's radius.

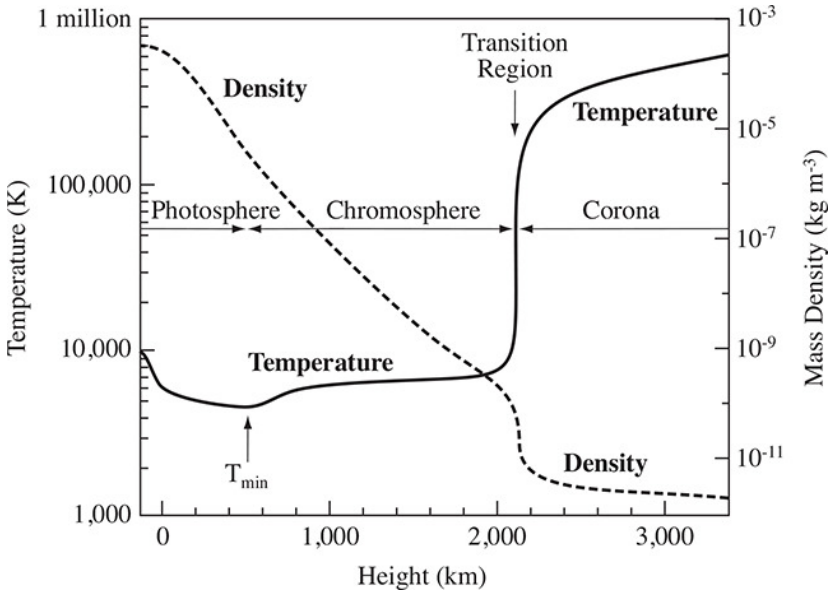

Figure 1.9: Temperature and density profiles of the solar atmosphere as a function of height above the solar surface (Priest, 2014).

The photosphere, or visible solar disk, is often described as the *surface* of the Sun. However, in reality, this is an illusion as the Sun is an entirely gaseous entity. We simply can't see through it as a result of gases present there that have high opacities. Hydrogen atoms are able to form in the photosphere due to the sufficiently cool temperature. However, rare collisions can occur in which hydrogen atoms capture free electrons, forming negatively charged ions. These negative ions absorb the radiation emanating from the solar interior due to their high opacity and re-emit visible light. This contributes to our inability to peer into layers of the Sun deeper than the solar photosphere (Lang, 2001).

The photosphere is the region from which photons can finally escape. Until this point, photons have been continually emitted and absorbed, gradually travelling outwards towards the photosphere over a period of ∼1 million years via a random walk motion with a very short mean free path, as described in Section 1.2.2. The photons are now finally free to propagate out into space to produce the Sun's characteristic solar spectrum. These photons are in thermal equilibrium with the surrounding matter and as a result the solar spectrum approximates a black body at 5778 K (see Figure 1.1). The photons do however encounter hot, tenuous plasma in higher levels of the atmosphere, resulting in the absorption lines that we see in the solar spectrum

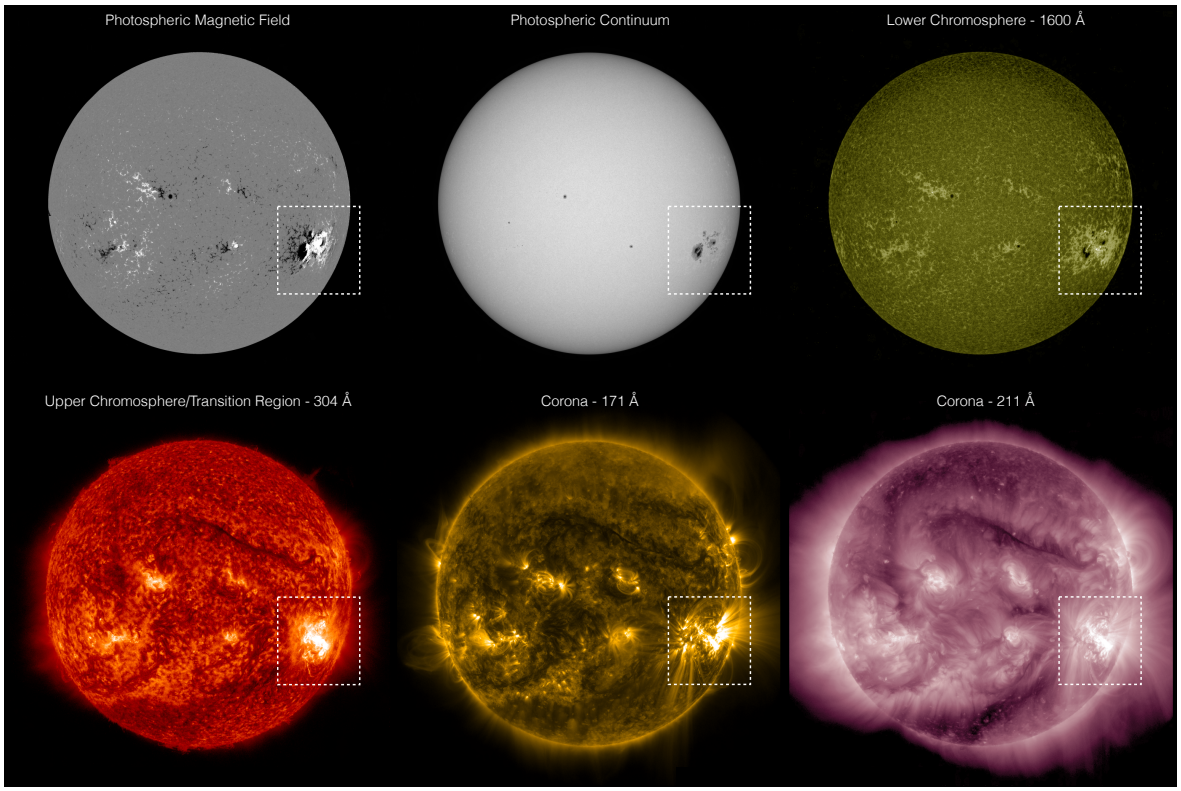

Figure 1.10: Multi-wavelength images taken by the Atmospheric Imaging Assembly (AIA) on board the Solar Dynamics Observatory (SDO). Each image has a different passband of wavelengths which are sensitive to the various layers of solar atmosphere discussed in this section. Shown are a magnetogram of the photospheric magnetic field (top left), the photospheric continuum (top centre), the lower chromosphere (top right), the upper chromosphere and transition region (bottom left), and the corona (bottom centre and bottom right). A box is drawn on each image highlighting a visible active region of concentrated magnetic field and solar activity. Source: Helioviewer.org

(Gary, 2012).

The photosphere reveals the convective nature of the interior layer below through its characteristically granular appearance as described in Section 1.2.3. These granulations have a lifetime of approximately 5 to 10 minutes and are typically about 1000 km in diameter (see Figure 1.4). Larger and deeper convective cells, known as supergranules, are produced by the same mechanism but can have much larger diameters up to ~ 35 Mm.

1.4.1.1 Sunspots

One of the most striking observational features of the photosphere are sunspots. Sunspots are regions of concentrated magnetic flux that appear darker than their surroundings.

Historically, we know from ancient chinese records that sunspots were first observed at least two thousand years ago (Lang, 2001). These would have been examples of rare, large sunspots many times the size of Earth. They appear dark due to their relatively cool temperature of ∼4000 K in comparison to the surrounding black body temperature in the photosphere of ∼5778 K.

Their cooler temperatures are a result of the concentrated magnetic field strength in theses regions, of the order of kilogauss (quiet magnetic regions of the photosphere are permeated by fields of ∼10 gauss), suppressing convection. Regions containing sunspots correspond to magnetic active regions that are associated with solar flares and coronal mass ejections. Studying their complexity and topology is a powerful tool for determining the likelihood of explosive energetic events occurring.

Figure 1.10 shows multi-wavelength images of the solar atmosphere. The top left image shows a magnetogram taken using the Helioseismic and Magnetic Imager (HMI) instrument on SDO. One can note the bipolar nature of the active region shown, in which there clear regions of opposite magnetic polarity aligned from west to east in the highlighted kernel. The top centre panel of Figure 1.10 shows a white-light continuum image of the photosphere where we can see sunspots manifested in the region of concentrated magnetic flux as shown by the aforementioned mangetogram. Figure 1.9 shows that the photosphere decreases in temperature with height until a we reach a temperature minimum before it again begins to rise (Priest, 2014). This marks the beginning of the next layer up of the solar atmosphere, known as the chromosphere.

1.4.2 The Chromosphere

This relatively thin layer of the solar atmosphere, ∼2.5 Mm thick, is named after the greek word *chromos* meaning 'colour' (Lang, 2001). This was due to its historical red appearance when it was first observed during a solar eclipse. It is characterised by its rise in temperature, its dynamic structure, and features such as *filaments*, *spicules*, and *prominences*.

In white light, we are blind to the chromosphere due to the strong emission of

the photosphere in this waveband. However, as the density of the chromosphere is $\sim 10^6$ times less dense than that of the photosphere, we see strong emission lines as the tenuous gas present there is heated and becomes incandescent. Before our ability to tune into specific wavelengths that are sensitive to specific regions of the solar atmosphere, we had to wait for events such as solar eclipses to capture fleeting moments in which the chromosphere or corona would become visible.

The brightest emission line in the chromosphere is hydrogen. Imaging the sun using a Hα passband, which is a red emission line generated by hydrogen atoms at 656.3 nm, reveals the chromosphere and its features. Other emission lines such as CaII H and K are also sensitive to the chromosphere. In EUV, the 1600 $\mathring{A}$ and 304 $\mathring{A}$ channels, reveal features of the lower and upper chromosphere, respectively. Figure 1.10 shows images of the Sun in these EUV passbands.

Filaments and *spicules* are dynamic features of the chromosphere. Filaments are dark arcs of plasma that extend across large portions of the solar disk. They are regions of cooler plasma, trapped in suspension by magnetic fields. However, when observed at the solar limb, they appear bright and are referred to as *prominences*. Spicules are needle shaped jets of plasma, $\sim$2 km in width, that can shoot 10^4 km up into the solar atmosphere at speeds of 100 km s^{-1}. There are $\sim$500,000 spicules visible in the chromosphere at any one moment (Lang, 2001). They are believed to play a role in the heating of the upper regions of the solar atmosphere. Towards the upper edge of the chromosphere, the temperature begins to dramatically rise as we reach a point called the transition region.

1.4.3 The Transition Region

The link between the chromosphere and the corona is known as the transition region. This region is only $\sim$ 100 km thick and yet the density of the solar atmosphere changes over several orders of magnitude and the temperature increases from 2000 k to $\sim$1 Mk (Aschwanden, 2005).

As mentioned in Section 1.4, this is extremely puzzling as it appears to violate the

laws of thermodynamics - heat simply should not flow from cooler regions to hotter regions. The 304 Å passband image in Figure 1.9 shows the chromosphere and transition region. Significant efforts have been made to understand how this heating occurs. It is believed that the source of the coronal heating is related to free magnetic energy generated at the photosphere and deeper regions of the Sun which is then transported and converted to heat (Browning et al., 2008). Identifying in detail the method through which this energy transport occurs remains undiscovered.

1.4.4 The Corona

At ∼2500 km above the photosphere, the outermost layer of the solar atmosphere known as the corona begins. It is extremely tenuous, with maximum electron densities of $\sim 10^{11}\ cm^{-3}$, and hot, with temperatures that can exceed ∼4 Mk in active regions. The corona is very faint in comparison to the photosphere. In the past, before modern instrumentation, eclipses offered the only opportunity for us to observe the patterns of free electrons in the corona, made visible as light scatters off of them as they trace the complex magnetic field lines of the high solar atmosphere.

The pressure produced by a magnetic field, P_m, transverse to its direction is

$$P_m = B^2/2\mu_0 \tag{1.6}$$

where B is the magnetic field strength in tesla and μ_0 is the permeability of free space. The gas pressure exerted by a plasma due to particle motion is

$$P_g = NkT \tag{1.7}$$

where N is the particle number density, k is Boltzmann's constant, and T is the temperature. In the corona, the magnetic pressure exceeds the gas pressure resulting in the emission tracing out the magnetic topology of the environment. In the photosphere, the gas pressure dominates. This results in photospheric motions driving the overlying coronal magnetic field.

The shape of the corona varies dramatically with the solar cycle. For example, during the solar maximum, the complexity of the magnetic is at its peak, meaning there will be more active regions present and hence more visible regions of spectacular coronal loops interspersed around the solar disk. The 171 Å and 211 Å images in Figure 1.9 show the complex magnetic topology, such as the coronal loops, traced out by the EUV emitting electrons.

Observations of images of the corona in the EUV and x-ray regimes reveal systems of both *open* and *closed* magnetic field lines. These features are also shown by models of the coronal magnetic field such as potential free source surface (PFSS) extrapolations (Schrijver & De Rosa, 2003). Magnetic field models, as well electron density models, and their relevance to this thesis are discussed in more detail in Section 1.4.5. Open magnetic field lines are most prominent at the poles, connect the solar atmosphere to interplanetary space, and provide an escape route for accelerated particles. It is believed open field lines give rise to the fast solar wind. Open field regions are associated with *coronal holes* as they are less dense than their surroundings due to the particles constantly escaping. Coronal holes are visible in EUV/x-ray images and appear darker than their surroundings. Active regions contain closed field lines which manifest as bright coronal loops rooted in magnetic footpoints of opposite polarity. The plasma is these regions is confined and hot, appearing bright in EUV/x-ray images. These active regions are the origin of solar flares and coronal mass ejections.

1.4.5 Coronal Magnetic Field & Density Models

The importance of the solar magnetic field cannot be overstated. It is responsible for everything from solar flares, to the effects of space weather seen at Earth (such as auroras), to interplanetary radiation and coronal mass ejections. Despite its position of importance, we still predominantly rely upon models and extrapolations to inform us about the magnetic field above the photosphere.

The Zeeman Effect describes the phenomenon in which spectral lines split into several components in the presence of a magnetic field. In a solar context, such effects

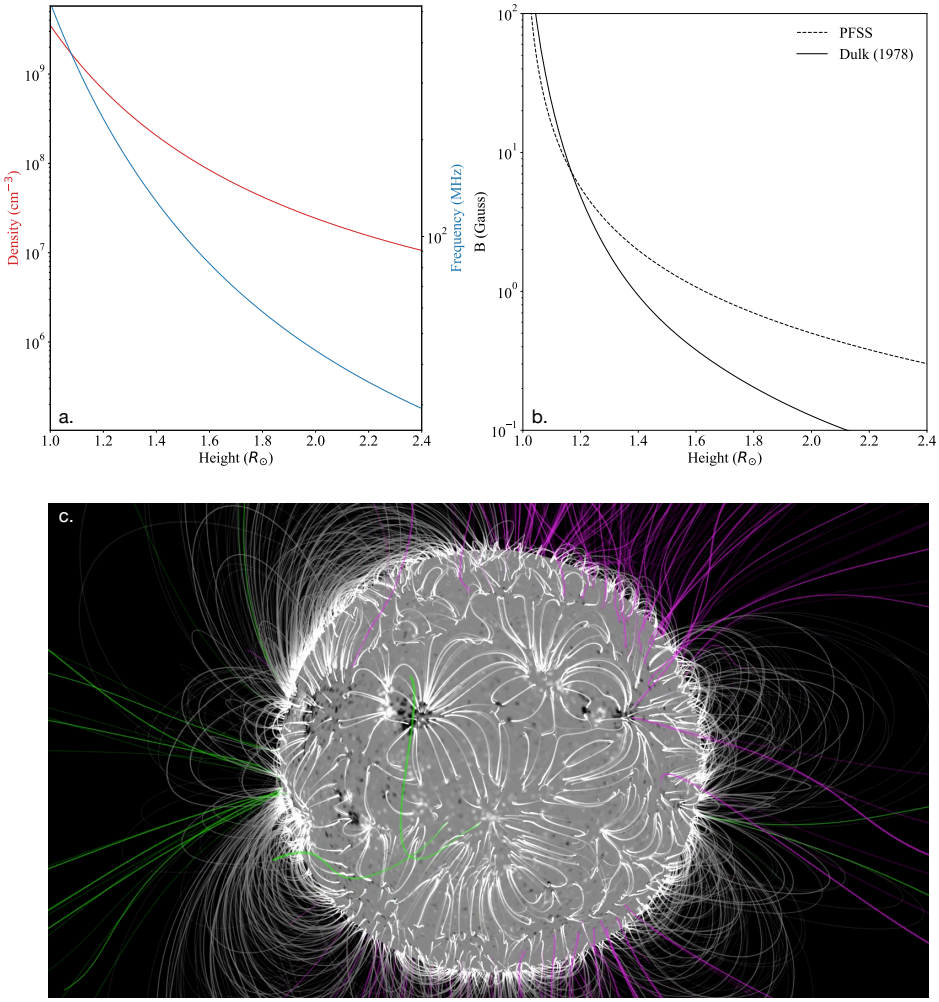

Figure 1.11: (a): Electron density and plasma frequency as a function of height derived from the model of Newkirk Jr. (1961). (a): Magnetic field strength as a function of height derived from the model of McLean et al. (1978) and a PFSS. (c): A PFSS extrapolation which provides an approximation of the coronal magnetic field up to 2.5 $R_\odot$ based on the observed photospheric field.

can be exploited to generate magnetograms of the photosphere which describe the strength and polarity of the magnetic field. An example of such an instrument that uses observations of the photosphere to generate magnetograms is the Helioseismic and Magnetic Imager on-board SDO.

However, to date, scientists must generally turn to models and simulations to obtain information about the topology and strength of magnetic fields higher up in the solar atmosphere. One such example that combines observations with theoretical knowledge is a Potential Field Source Surface, or PFSS, extrapolation. Other techniques for developing models of the coronal magnetic field involve combining extrapolations with

in-situ measurements and radio data such as the McLean et al. (1978) model given by the following

$$B(R) = 0.5\big[R/R_{\odot} - 1\big]^{-1.5}. \tag{1.8}$$

where $B(R)$ is the magnetic field strength for given heights, R, in the solar atmosphere. To date, the solar magnetic field is yet to be fully mapped out. In Chapter 4, we present a new technique of remote sensing the coronal magnetic field using solar radio bursts.

Another key parameter of the solar atmosphere is the electron number density which, like the magnetic field strength, is inversely proportional to height. The plasma frequency, f_p, is related to the electron density, N_e, via:

$$f_p = \frac{\omega_P}{2\pi} = \frac{1}{2\pi}\sqrt{\frac{N_e e^2}{m_e \epsilon_0}} \approx 9000\sqrt{N_e} \tag{1.9}$$

where ω_P is the angular frequency of the plasma radiation, m_e is the electron mass, e is the electron charge, and ϵ_0 is the permittivity of free space. Radiation is emitted at this frequency during the plasma emission process, discussed in Section 2.6.1 of Chapter 2, which plays a key role in solar radio physics. Although many density models have been developed and are often used, actual density measurements of the corona have been made via EUV and white-light observations. Different density models, such as those put forward by Allen (1947) and Newkirk Jr. (1961) are more applicable to certain altitudes or conditions of the solar atmosphere. Panel (a) of Figure 1.11 shows a plot of the Newkirk Jr. (1961) electron density model, as well as it transformed into frequency space via Equation 1.9. Panel (b) shows magnetic field strength as a function of height according to the McLean et al. (1978) magnetic field model and a PFSS model. Panel (b) is a visualisation of a PFSS extrapolation where one can note the open filed lines in green and purple and the closed filed lines in white. These properties of density and magnetic field strength play a key role in the emission mechanisms of solar flares.

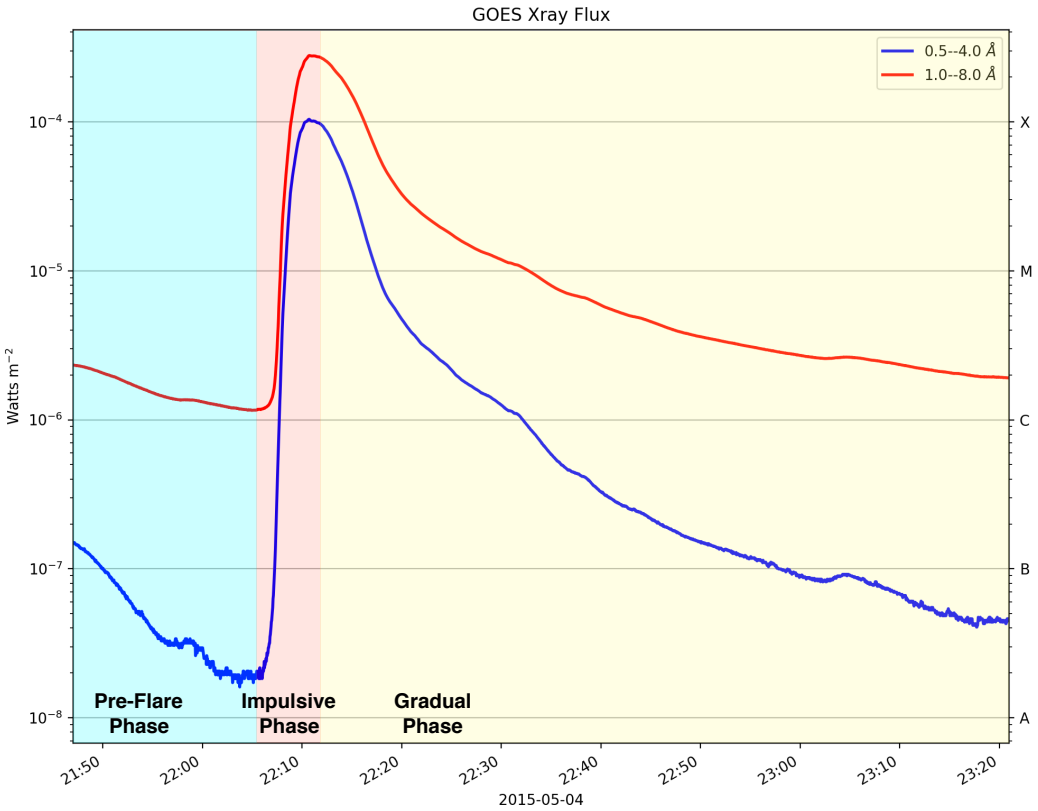

Figure 1.12: X-ray light curves of a X2.7 class solar flare observed by GOES. The 1.0-8.00 Å and 0.5–4.00 Å channels are shown in red and blue, respectively. The phases of the flare and the GOES classification scale are also shown.

1.5 Solar Flares

In this thesis, the role of particle acceleration in flares is explored from a multi-wavelength perspective. Chapter 4 outlines how radio emission, that is a consequence of outwardly propagating electron beams, can enable us to remote sense the coronal magnetic field. Chapter 5 illustrates how particle acceleration can occur intermittently during flares yielding a phenomenon known as quasi-periodic pulsations. Lastly, Chapter 6 explores the relationship between radio and X-ray observations using modern instrumentation. In this section, the fundamentals of solar flares are introduced.

Solar flares are the largest releases of energy in our solar system. They can release up to 6×10^{25} J of energy in just a few minutes (Kopp et al., 2005). To put the enormity of this amount of energy into context, it is equivalent to ∼1,600,000,000,000 atomic bombs exploding at once. When flares occur, massive of amounts of heating

and particle acceleration take place that give rise to a multitude of electromagnetic emission (EM) mechanisms. Disentangling the observed multi-wavelength EM emission from flares is crucial in order for us to understand the processes and mechanisms at play, and gain insight into fundamental plasma physics and the physics of solar flares in general. A particularly spectacular type of solar activity known as coronal mass ejections (CMEs) often, but not always, accompany solar flares. CMEs are enormous releases of plasma and magnetic field that propagate into space with typical speeds of 10^3 kms^{-1} (Yurchyshyn et al., 2005). It was thought in the past that CMEs were a consequence of flares, however, recent studies have contradicted this assumption which has re-opened the discussion of the relationship between the two phenomena.

A process known as magnetic reconnection, discussed in Section 2.4, is theorised to be the method through which energy release occurs in flares (Priest & Forbes, 2002). In short, magnetic reconnection involves the build-up of magnetic energy as the magnetic configuration becomes highly stressed, complex and unstable. The system then relaxes to a lower energy state, releasing energy. This process produces thermal and kinetic energy, heating the surrounding plasma and accelerating particles to non-thermal velocities. Radiation across the electromagnetic spectrum is produced in the process from low frequency radio waves through to γ-rays.

Flares are ranked based on their peak X-ray flux in the 1-8 Å channel observed by the Geostationary Operational Environmental Satellite (GOES) (Bengston & McCuistion, 1996). They can be classified as A, B, C, M, and X, with each listed class having a peak flux ten times greater than the last. Figure 1.12 shows an example of an X2.7 class flare observed by GOES. Also shown on the plot are the three temporal phases of the flare, namely the *pre-flare phase*, *the impulsive phase* and *the decay phase*. Some minor activity can be observed during the pre-flare phase as the active region heats, however, the bulk of the energy release occurs during the impulsive phase. The impulsive phase is characterised by high energy radiation, such as hard x-rays and γ rays, reflected by the highly energetic particles that are accelerated at this point. EUV and optical emission is also generated during this phase as the local plasma is heated

by the accelerated particles. During the gradual phase, most impulsive activity has ceased and the heated plasma begins to cool and relax to a pre-flare state. Conduction and radiation are thought to be the dominant cooling mechanisms (Culhane et al., 1994). This gradual phase can last hours while the impulsive phase occurs over a period of minutes. These phases will be referred to further in the following section which describes the standard flare model.

1.5.1 Standard Flare Model

The standard flare model, sometimes referred to as the CSHKP model, was first put forward by Carmichael (1964), Hirayama (1974), Kopp & Pneuman (1976), and Sturrock (1968). Figure 1.13 shows a cartoon of the standard flare model, which outlines the fundamentals of flaring emission (Kitchin, 2007). The energy release, thought to be due to magnetic reconnection, occurs above the loop-top at a magnetic null point. This energy release accelerates particles to relativistic speeds which leads to various types of thermal and non-thermal electromagnetic emission. Examples of the dominant non-thermal emission mechanisms at play here include plasma emission, gyro-synchrotron emission, and Bremsstrahlung emission (Aschwanden & Benz, 1997). The theoretical details of relevant solar flare emission mechanisms is described in Chapter 2.

In the CSHKP framework, the accelerated particles spiral downwards along newly reconnected closed magnetic field lines towards the chromosphere. These particles can emit gyro-synchrotron emission as they travel. Once they reach the denser chromosphere, which acts as a thick target (Brown, 1971), they undergo coulomb collisions and emit hard X-rays (HXRs), and even γ-rays, via non-thermal Bremsstrahlung. This occurs at the roots of the close magnetic field lines, located at the base of the coronal loops in the chromosphere, known as the *footpoints*. These footpoints are of opposite magnetic polarity. The chromosphere is then heated by these colliding electrons causing the local plasma to expand in a process called *chromospheric evaporation* resulting in thermal emission (Antiochos & Sturrock, 1978). This thermal emission manifests as soft X-rays (SXRs) and EUV emission in the loops of the flare site. This relationship

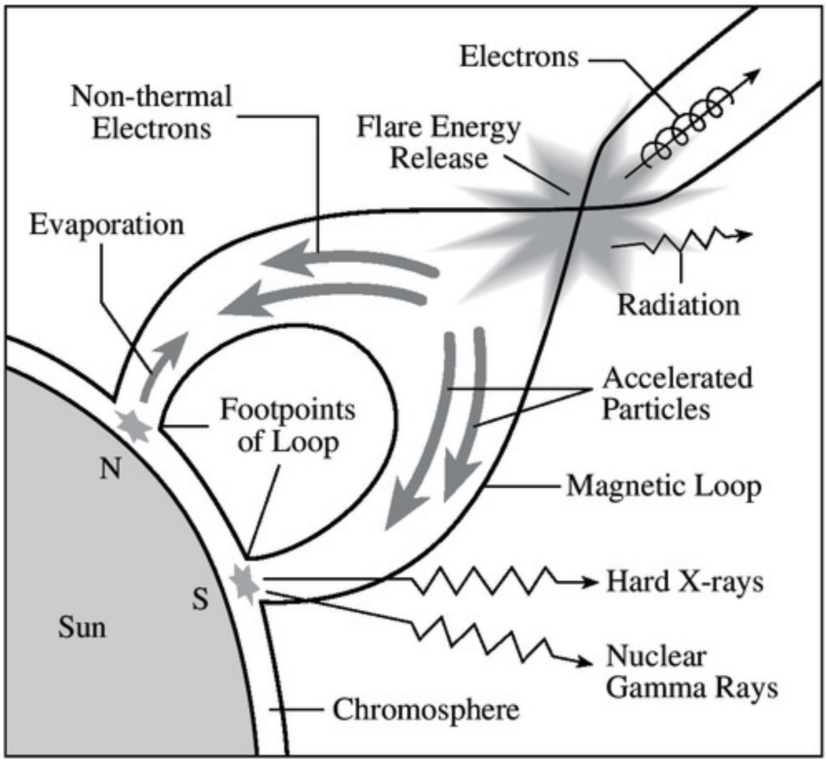

Figure 1.13: Cartoon of the standard flare model. At the energy release site, particles are accelerated towards interplanetary space as well as down towards the solar surface causing thermal and non thermal electromagnetic emission via multiple mechanisms (Kitchin, 2007).

between the HXRs and SXRs is validated by the Neupert effect (Neupert, 1968a). This is the observational phenomenon that the flux of the non-thermal hard X-rays (HXRs) is proportional to the flux of the time derivative of the thermal SXRs.

In addition to the electrons that precipitate downwards towards the chromosphere, some electrons can escape along newly open field lines toward interplanetary space. These beams of escaping electrons can produce solar radio bursts high in the solar atmosphere. The impulsive phase is dominated by the non-thermal hard X-ray emission, radio, and γ-ray emission produced as a result of intense particle acceleration. The more gradual brightening of the SXR and EUV emission occurs in the latter decay phase due to the heating of the surrounding ambient plasma.

Much of the expected morphology of flare sites according to the CSHKP model can be validated by X-ray, EUV, and radio imaging observations. For example, Figure 1.14 shows a 193 Å EUV image from AIA illustrating the thermal emission occurring in the flare loops. Overplotted are X-ray images made using the Reuven Ramaty High Energy

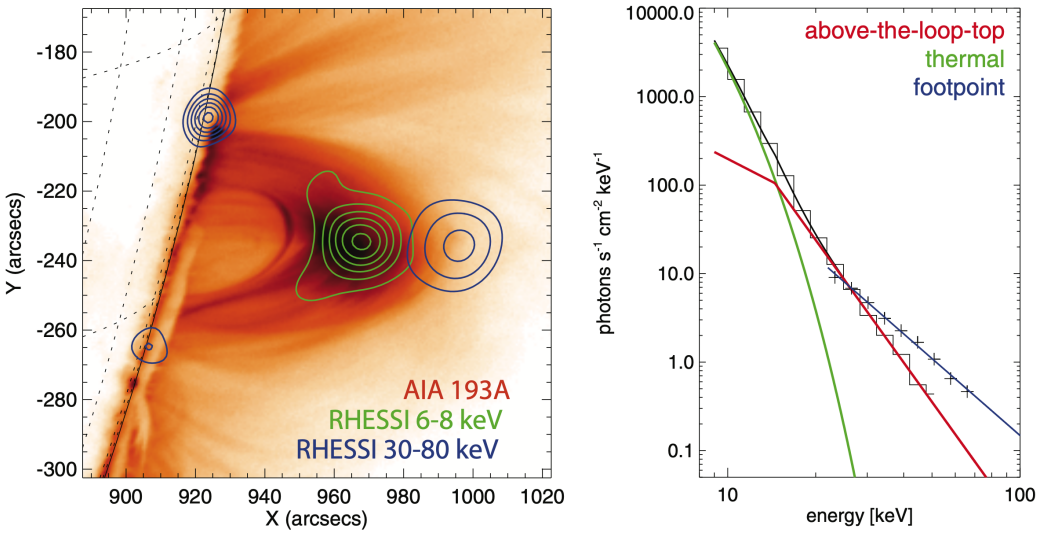

Figure 1.14: Imaging spectroscopy observations of the 2012 July 19 flare taken from Krucker & Battaglia (2014) which provides observational evidence for the standard flare model outlined in this section. Left: An 193 Å EUV image from AIA showing the thermal emission occurring within the flare loops. The blue contours, imaged by RHESSI, show the location of non-thermal (30-80 keV) HXR footpoints as well as a loop-top source. The green contours show the SXR thermal emission (6-8 keV) in the coronal loops. Right: Imaging spectroscopy results of the source showing thermal fits to the data in green and red with the non-thermal fit shown in blue.

Solar Spectroscopic Imager (RHESSI) (Lin et al., 2002). The blue contours show the location of the non-thermal (30-80 keV) HXR footpoints, as well as a loop-top source, while the green contours show the SXR thermal emission (6-8 keV) in the coronal loops. The right side of the figure shows the Imaging spectroscopy results where we see that data fits to a combination of thermal and non-thermal models. In the following section, solar radio emission produced as a result of the accelerated electrons which propagate away from the flare site will be introduced.

1.6 Solar Radio Bursts

An important element of the solar electromagnetic emission we observe is from the radio regime. Radio emission from flares can arise via multiple mechanisms such as gyrosynchrotron emission, Bremsstrahlung, plasma emission, and electron Cyclotron Maser (ECM) Emission. Different mechanisms dominate within specific frequency bands, which in turn dominate at specific heights of the solar atmosphere. Figure 1.15

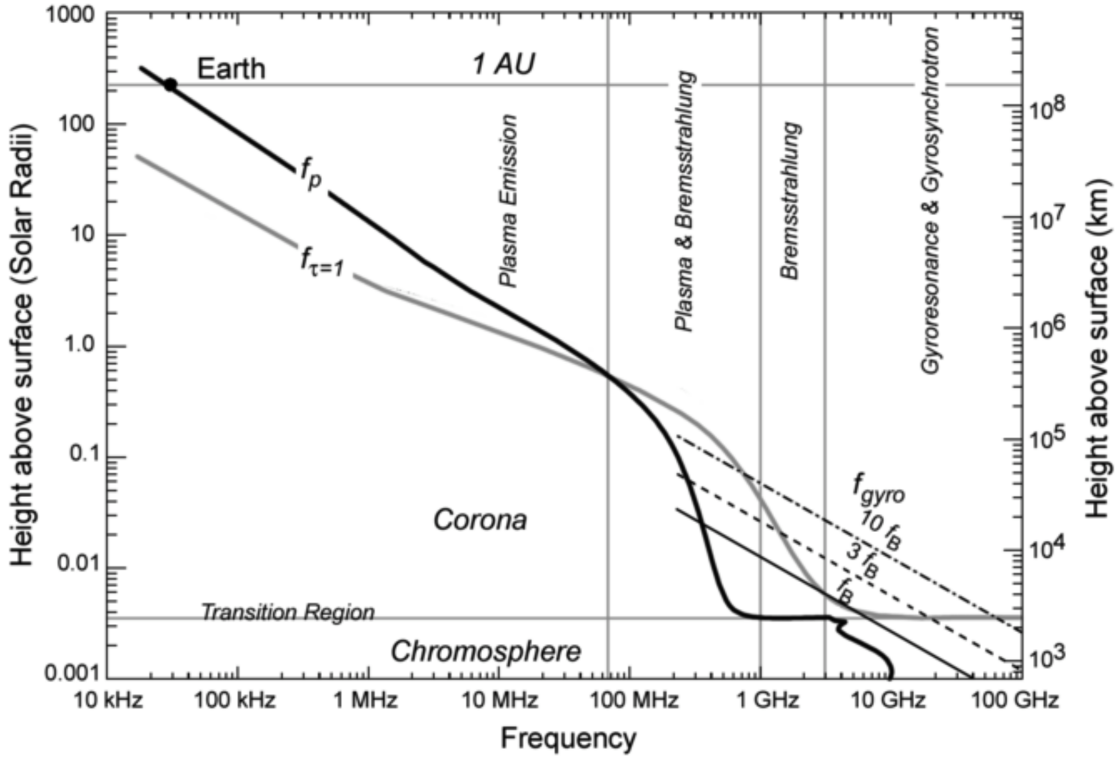

Figure 1.15: The dominant radio emission mechanisms in the solar corona as a function of height for various frequencies (Gary & Hurford, 1989).

shows which mechanisms dominate for various frequency bands as a function of height.

The most pronounced form of radio emission we observe associated with solar flares and CMEs comes in the form of solar radio bursts. Solar radio bursts are classified into five main types (Wild, 1963). Figure 1.16 shows a cartoon of dynamic spectrum containing each of the these in addition to another sub class known as S-bursts. Solar radio bursts are classified by how their frequency changes with time, known as their drift rate (Reid & Ratcliffe, 2014). S-bursts and Type III radio are a focus of the work in this thesis and so are introduced below.

1.7 S-bursts

In addition to the five standard classes of radio bursts (Types I-V), various types of radio bursts have been identified at metre and decametre wavelengths; these include metric spikes (Benz et al., 1996, 1982), drifting spikes (Elgaroy & Sveen, 1979), decametre spikes (Melnik et al., 2014), and supershort radio bursts (Magdalenić et al., 2006).

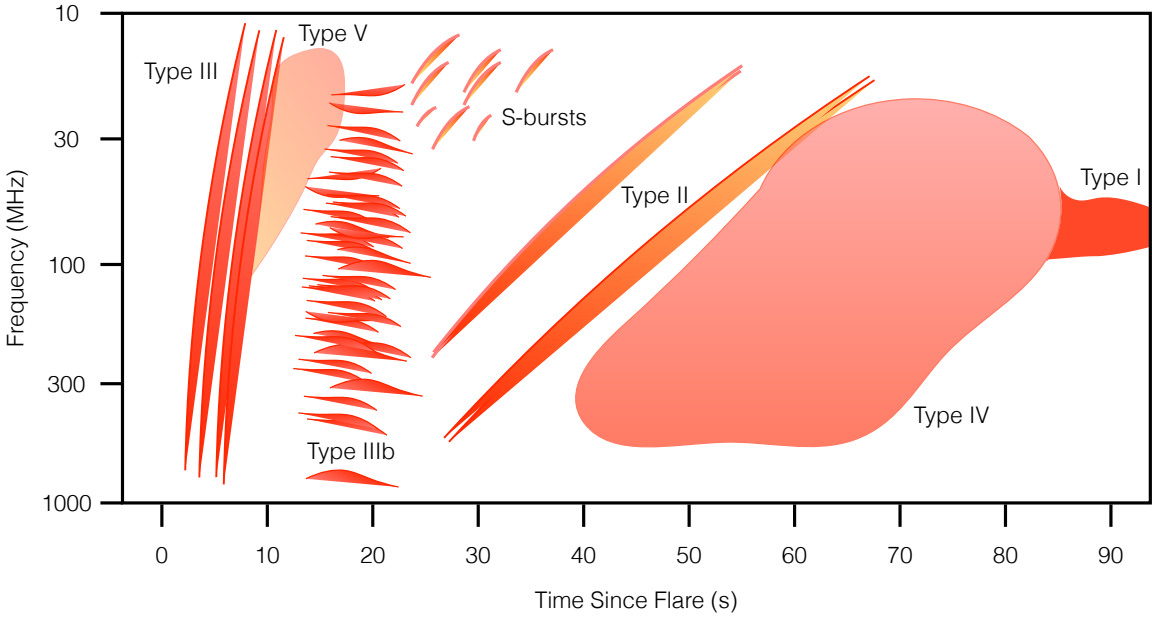

Figure 1.16: Cartoon of a dynamic spectrum showing the five standard classifications of solar radio bursts in addition to solar S-bursts.

These bursts usually have short durations of $\leq$1 s and fine frequency structure, which may suggest that small-scale processes occur in the corona (Morosan et al., 2015). At longer wavelengths ($>$ 3 m), or frequencies $<$ 100 MHz, instrumental limitations have prevented detailed studies of fine structure radio bursts. However, using 32 broad-band dipoles, Ellis (1969) was able to successfully identify a new type of solar radio burst at these frequencies that he called fast drift storm bursts. These intriguing, low frequency bursts were investigated further by McConnell (1982), using the Llanherne Radio Telescope in Australia (4096 dipoles). McConnell renamed these solar S-bursts, owing to their similarity to Jovian S-bursts: the S stands for short or storm.

S-bursts appear as narrow tracks on a dynamic spectrum that usually drift from high to low frequencies, and in rarer cases, from low to high frequencies. Figure 1.17 shows an example of a dynamic spectrum containing S-bursts, type III bursts, and a type IIIb burst. As the data is flux calibrated, colour bars are included that indicate the flux values of the bursts. This data was obtained from the Ukrainian T-shaped Radio telescope, second modification (UTR-2). UTR-2 consists of 2040 array elements in two arms, north-south and east-west, which make up the T-configuration of the instrument. The north-south arm contains 1440 elements spread out over 240 rows

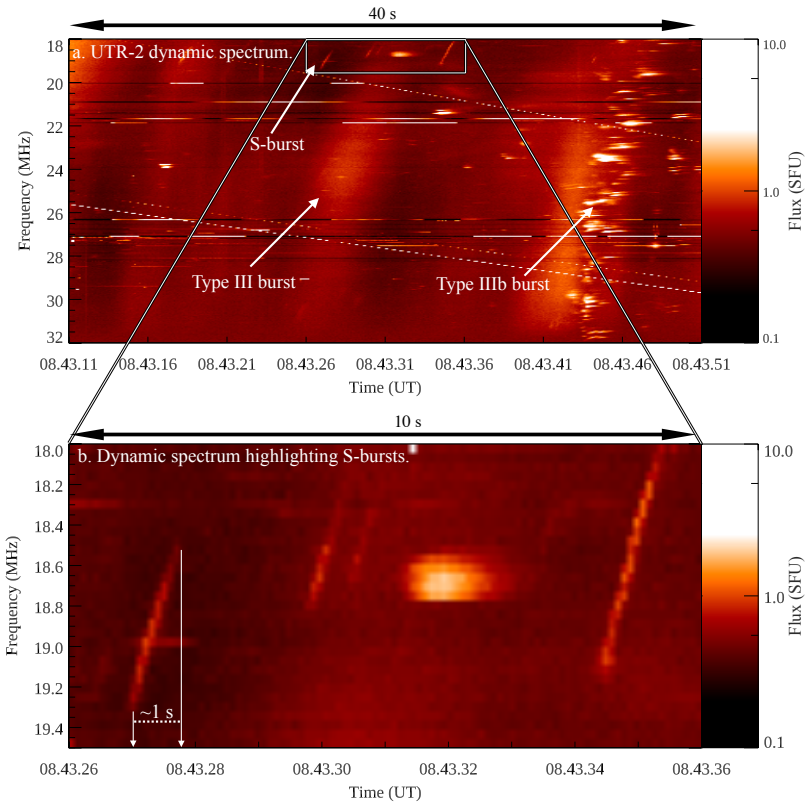

Figure 1.17: Panel (a): Dynamic spectrum obtained from the Ukrainian T-shaped Radio telescope, second modification (UTR-2) on 9 July 2013 containing examples of type III, type IIIb, and S-bursts. Several negatively drifting S-bursts are shown within the highlighted region between the times of 08:43:26 UT and 08:43:36 UT and the frequency range of 18-19.5 MHz. A type III burst is also visible in this time frame. A type IIIb burst is visible between the times of 08.43.41 UT and 08.43.46 UT. Panel (b): The highlighted region is shown in greater detail, indicating the short duration of the bursts (<1 s). Colour bars indicate the flux values of the bursts in solar flux units.

while the east-west arm contains 600 elements spread out over 6 rows. The two arms of the telescope combine to give a total area of $\sim$1.4 $\times 10^5$ m^2. The UTR-2 instrument operates within a frequency range 8-32 MHz with a frequency resolution of 4 kHz. Further information about this instrument is provided in Chapter 3.

S-bursts typically have a duration of $\leq$1 s and have been observed to occur in a frequency range of 10-150 MHz, their number decreasing towards lower frequencies (Dorovskyy et al., 2017; Ellis, 1969; McConnell, 1982; Melnik et al., 2010; Morosan et al., 2015). S-bursts have short instantaneous bandwidths (frequency width at a fixed central time, Δf). Ellis (1969) and McConnell (1982) observed that the instantaneous bandwidths of S-bursts lie in a wide range. McConnell (1982) observed values of 100 kHz at 30 MHz to 500 kHz at 80 MHz. Over a frequency band of 10-30 MHz, Melnik

et al. (2010) found that the instantaneous bandwidth of S-bursts increased linearly with frequency. S-bursts typically have a total bandwidth of approximately 2.5 MHz (McConnell, 1982; Morosan et al., 2015) and in rare cases can reach highs of 10-20 MHz, particularly in the decametre band (Melnik et al., 2010; Morosan et al., 2015). The full width half maximum (FWHM) duration (duration at fixed central frequency) was found to be < 400 ms by Morosan et al. (2015). S-bursts have low intensities, their fluxes rarely exceeding tens of solar flux units (SFU) (1 SFU $\equiv 10^4$ Jy) (Melnik et al., 2010). They usually have negative drift rates that vary from -7 MHzs^{-1} at 75 MHz to -0.6 MHzs^{-1} at 20 MHz (McConnell, 1982; Morosan et al., 2015). S-bursts have been found to have a wide range of circular polarisation degrees from two to eight times that of type III bursts (Morosan et al., 2015). S-bursts are associated with active regions and appear against the background of other types of solar radio activity such as type III and IIIb radio bursts (Melnik et al., 2010). The exact emission mechanism behind the generation of S-bursts remains a topic of debate, however, they are believed to be emitted at the plasma frequency.

As S-bursts are associated with active regions and so active region electron density and magnetic field models were used to estimate source heights and the magnetic fields at those heights for our analysis which is presented in Chapter 4 (McConnell, 1982; Melnik et al., 2010; Morosan et al., 2015). As solar S-bursts occur at low frequencies, their sources are expected to occur at high altitudes in the corona. Additionally, by assuming that S-bursts are produced as a result of the plasma emission mechanism, it is possible to estimate the velocity of the source electrons involved in the process via the frequency drift rate of the bursts. This can be achieved by using Equation 2.48 to find the electron density at the start time and end time of the burst. An electron density model can then be used to convert this information into a set of height versus time values which in turn can be used to infer the velocity of the exciter. McConnell (1982) observed that S-bursts drift at a rate that is approximately three times slower than the drift rate of type III radio bursts. This indicates that their source electron velocities are $\sim$0.1 c, which is approximately one-third of the velocity of typical type III burst

sources (Morosan et al., 2015). Several theories have been proposed to explain how S-bursts are generated that are introduced in Chapter 2. In Chapter 4 the properties of S-bursts are analysed in detail and it is shown how they can be used as new tool for remote sensing the coronal magnetic field.

1.8 Type III Radio Bursts

Type III radio bursts appear as rapidly drifting features on dynamic spectra that have durations of just a few seconds. They are one of the most common forms of solar radio bursts that we observe and are associated with periods of moderate to high solar activity. Although they were first suggested to originate from active regions alone, many observations have also been made without the occurrence of a solar flare (Dulk, 1985). They are associated with the impulsive phase of solar flares during which time high amounts of particle acceleration are taking place. They can occur in isolation or as type III storms, which are cases when many bursts continually occur over several hours. An example of a type III radio burst observed by UTR-2 is shown in Figure 1.17

Their relevance to this thesis is due to the fact that they represent a signature of particle acceleration. As mentioned in Section 1.5.1, during solar flares, accelerated electrons precipitate towards the chromosphere but can also escape along open field lines towards interplanetary space. These escaping electron beams can result in the onset of the plasma emission process (see Section 2.6.1) which gives rise to the generation of type III bursts.

Similarly to S-bursts, it is possible to estimate the velocity of the source electrons via an electron density model due to the fact that they are produced via plasma emission. Using this method, the typical velocity is found to be sub-relativistic with a value of $\sim$0.30 c.

Due to the fact that HXRs in solar flares are produced via the downward propagating electrons colliding with the chromosphere, while type III bursts are associated with the outwardly travelling beams, there is a well established connection between HXRs and type III bursts. This is discussed further in Section 1.10. As type III radio

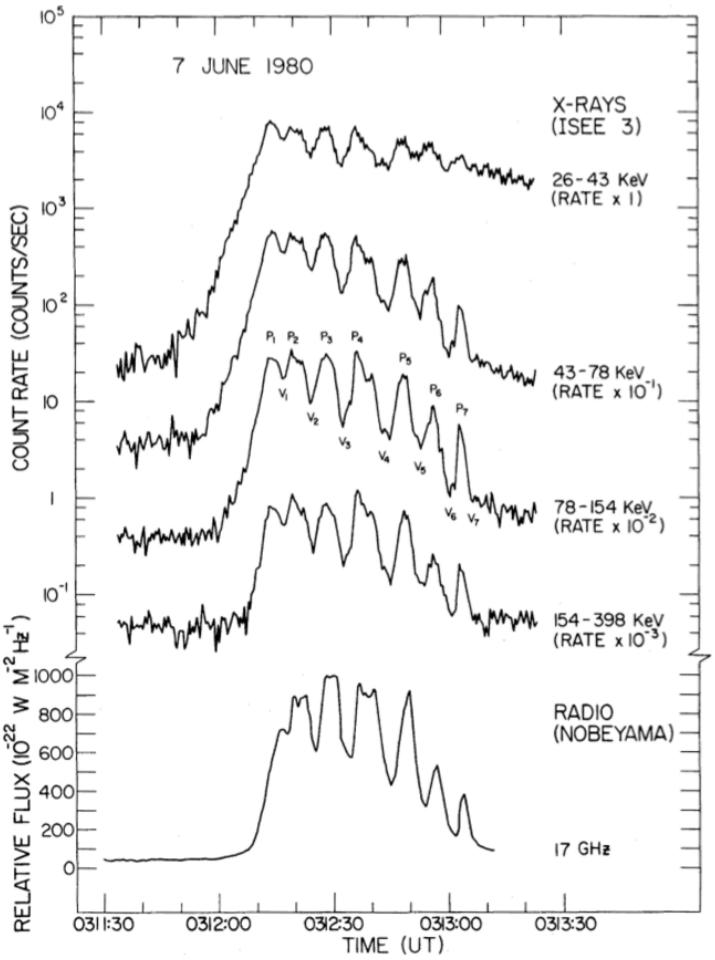

Figure 1.18: Prominent example of QPPs known as the '7 sisters' flare taken from Kane et al. (1983). One can note the seven distinct pulsations separated by a period of ∼8 s.

bursts often occur in groups during solar flares, it is possible that the energy release mechanism driving solar flares occurs in a time dependent fashion that is linked to intermittent particle acceleration. This idea leads on to the next introductory topic relevant to the work in this thesis which describes the phenomenon of quasi-periodic pulsations.

1.9 Quasi Periodic Pulsations in Solar Flares

Quasi-periodic pulsations (QPPs) are an important feature observed in solar and stellar flare emission (Kupriyanova et al., 2020; Nakariakov & Melnikov, 2009; Van Doorsselaere et al., 2016). This puzzling phenomenon lacks a concrete definition, however, they

are typically described by variations in the flux from a flare as a function of time that appear to include periodic components and time-scales that typically range from 1 s up to 1 min, and in extreme cases from $\leq$1 s up to several minutes (Hayes et al., 2019; Karlický et al., 2005; Li et al., 2015; Tan et al., 2010). QPPs are typically observed during the impulsive phase of solar flares, however, in recent years it has become clear that they can persist through to the decay phase, after the impulsive energy release (Dennis et al., 2017; Hayes et al., 2019; Hayes et al., 2016). Figure 1.18 shows a historic example of QPPs in which seven distinct peaks are visible with a period of $\sim$8 s (Kane et al., 1983).

There are several significant reasons highlighting the importance of understanding the nature of QPPs. Given their ubiquity, occurring in $\sim$46 % of X-class flares in the last solar cycle, it is crucial that they are accounted for in any flare model (see Figure 1.19). Additionally, studies have shown that active region properties can be related to the QPP period. Figure 1.20 shows a scatter plot of flare ribbon separation versus QPP period for which there appears to be a significant correlation. This relationship would enable one to remotely infer active region properties based on the period of the QPPs observed. There also appears to be similarity between solar and stellar QPPs as shown in Figure 1.21. This relation would provide a powerful tool for inferring morphological properties of stellar active regions based on QPPs observed in light curves.

QPPs have been reported in a broad range of wavelengths from decametric radio (Carley et al., 2019; Li et al., 2015), through to extreme ultra-violet (EUV) and X-rays, (Dolla et al., 2012; Dominique et al., 2018), and even γ rays (Li et al., 2020; Nakariakov et al., 2009). Statistical studies suggest that QPPs are a common feature, especially in larger flaring events (Hayes et al., 2020b; Inglis et al., 2016; Simões et al., 2015). Within the decimetric waveband, QPPs can manifest as a sequence of type III radio bursts emanating from the corona as a consequence of accelerated beams of electrons escaping along open magnetic field lines away from the flare site (Aschwanden et al., 1994; Kupriyanova et al., 2016; Ning et al., 2005). In contrast, QPPs in the

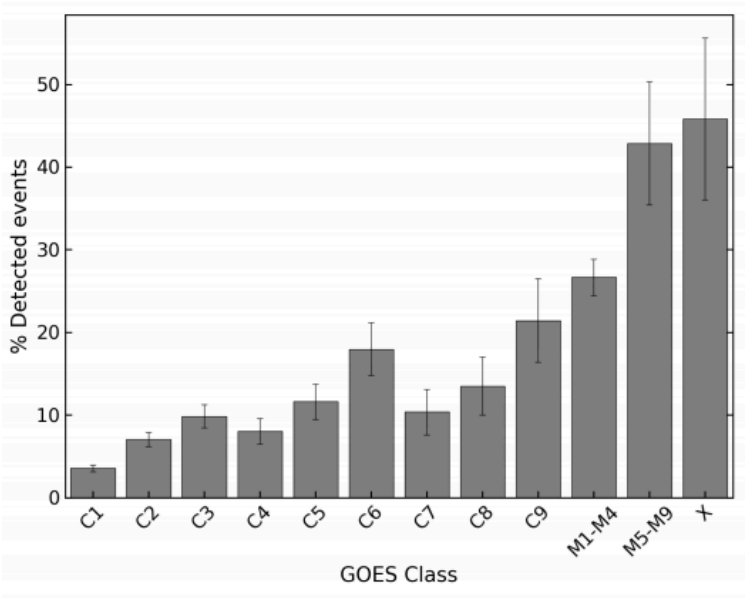

Figure 1.19: Percentage of detected QPP events for different GOES class flares. Taken from Hayes et al. (2020a)

EUV are typically observed to originate from the hot plasma in the coronal loops of a flaring region (Van Doorsselaere et al., 2016). In addition to studies of QPPs analysed within specific spectral domains, some research has been done focusing on events containing QPPs across a wide band of wavelengths. For example, Aschwanden et al. (1993) investigated the timing of HXR pulsations with respect to pulsations seen in radio wavelengths (100-300 MHz) and found evidence for a strong causal connection. Additionally, Tajima et al. (1987) found that current loop coalescence can lead to quasi-periodic amplitude oscillations in the microwave, X-ray, and γ-ray wavebands. More recently, Kumar et al. (2016) presented a multi-wavelength analysis of QPPs found to be occurring in HXR, radio (25–180, 245, 610 MHz), and EUV wavelengths.

Several models have been proposed as explanations for the presence of QPPs in solar and stellar flares (McLaughlin et al., 2018) which are typically categorised as oscillatory or self-oscillatory processes. In the regime of oscillatory processes, QPPs are interpreted as a signature of magnetohydrodynamic (MHD) oscillations inducing periodic motions about an equilibrium in the flaring region. This explanation has been promising for some events, as some observed periodicities of QPPs are in good agreement with that of the timescales of MHD waves in the corona (Nakariakov &

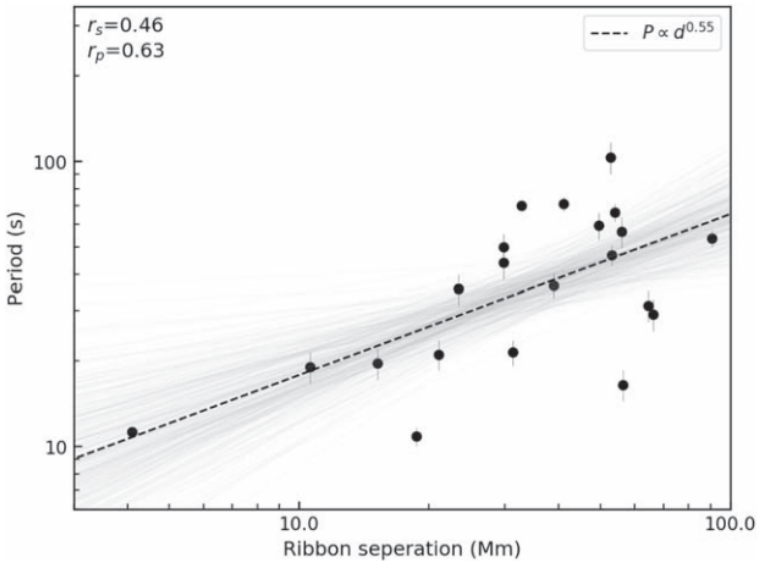

Figure 1.20: Scatter plot of QPP period and ribbon separation taken from Hayes et al. (2020a).

Melnikov, 2009). There is widespread observational evidence for MHD waves existing in the corona and it is possible that kink, toroidal, longitudinal, or sausage modes could cause some of the thermal and non-thermal intensity variations that we observe.

For example, kink mode oscillations have been reported that have an overlapping timescale (∼1.5-10 minutes) with observed QPP periodicities (Anfinogentov et al., 2015). Such waves could periodically modulate emission or influence particle dynamics (Nakariakov & Melnikov, 2009). It is also possible that the presence of these waves could trigger magnetic reconnection resulting in a periodicity related both to the type of wave mode involved and the properties of the coronal loops (Carley et al., 2019; Nakariakov & Zimovets, 2011). In the other category of self-oscillatory processes, QPPs are interpreted as a manifestation of time dependent, intermittent magnetic reconnection. Despite a plethora of studies and observations of QPPs in various contexts, the underlying mechanism for their generation remains a topic of debate. In Chapter 2 the details of these proposed mechanisms is described while in Chapter 5 a detailed study of QPPs and there relation to particle acceleration is presented.

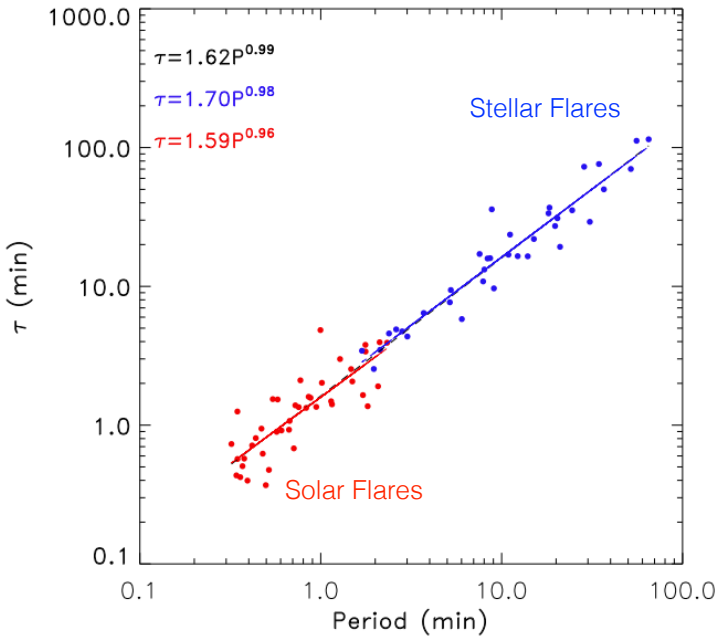

Figure 1.21: Damping time versus QPP period for solar and stellar flares. Taken from Zimovets et al. (2021)

1.10 X-ray and Radio Signatures of Accelerated Electrons

There is a longstanding temporal association between HXRs and various types and radio emission. Peterson & Winckler (1958) carried out some of the first observations for which the temporal profiles of the emission at microwave wavelengths and hard X-rays were seen to be very similar. This similarity indicated that the same population of accelerated electrons during the event were responsible for both types of emission. Due to this temporal similarity, it is believed that the emission at both spectral ranges originates from the same population of accelerated electrons during the event. Figure 1.9 shows an example of such a case. Here, the microwave emission is a consequence of gyrosynchrotron emission. The association is explained by the fact that the accelerated electrons spiral along closed magnetic field lines producing the microwaves before they emit HXRs via bremsstrahlung emission mechanism as the collide with the chromosphere at the flare footpoints. Recently, da Silva & Valio (2021) showed that for such

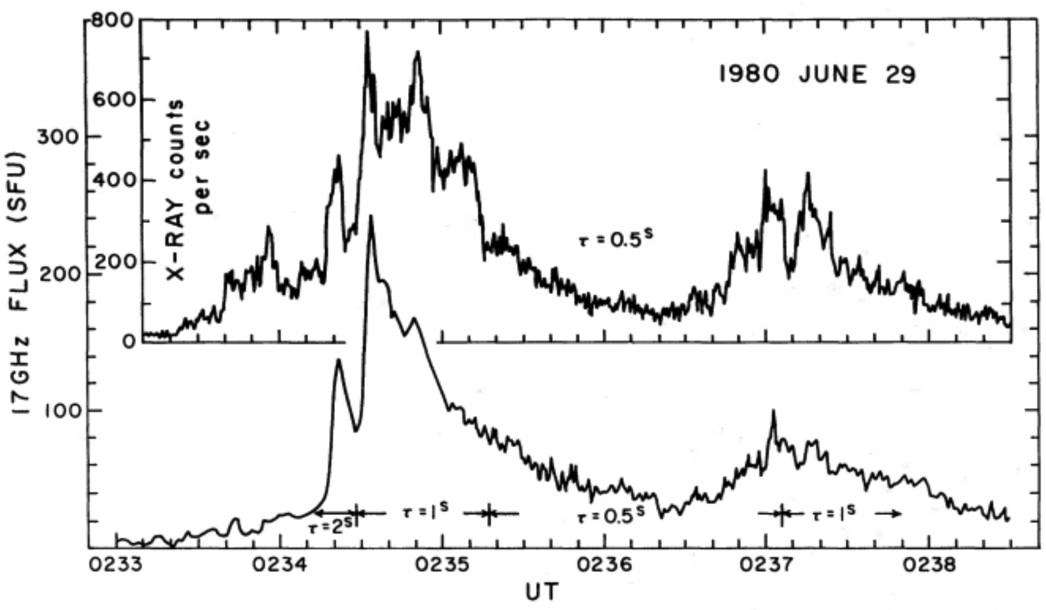

Figure 1.22: X-ray and radio profiles of a flare showing close temporal correlation between the two wavebands (Dulk & Dennis, 1982)

cases, the spectral indices of the radio and x-ray producing electrons match for energies above ∼600 keV.

For low frequency radio emission in the form of type III radio bursts, it is also possible to link the source electrons to those producing the HXRs. However, in this case, there are complications due to the fact that the radio emission is produced high in the corona (or even in interplanetary space) via an emission mechanism that is more complex and dependent upon the local conditions to take place. Reid & Kontar (2018) showed via modelling a relationship between the spectral index of the HXRs with the velocity of the electrons producing the type III radio bursts. This is what one would expect if the populations of electrons were related as it indicates that more energetic electrons produce faster drifting type III radio bursts.

In Chapter 5, we provide observational evidence that links HXR pulsations with a sequence of type III radio bursts while in Chapter 6 we further explore the relationship using modern instrumentation and spectroscopic techniques that build up on the modelling by Reid & Kontar (2018).

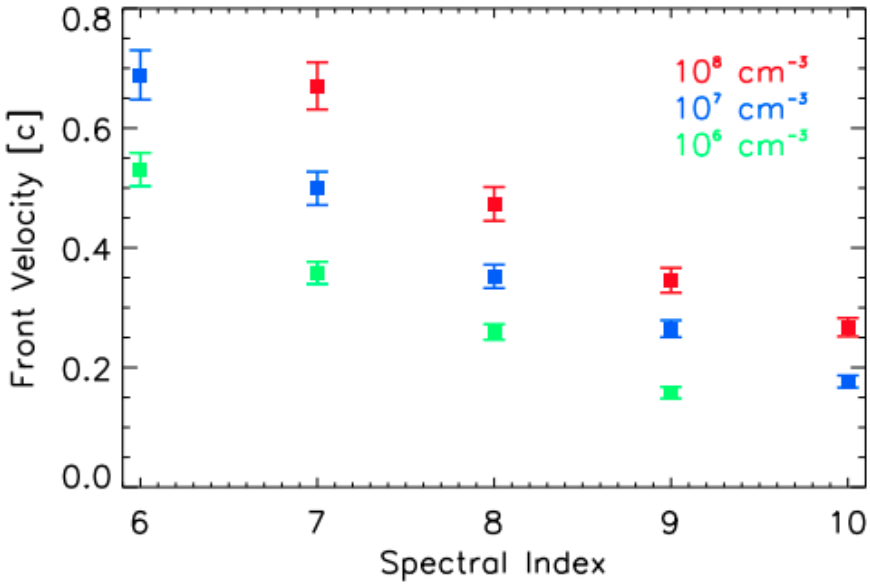

Figure 1.23: Type III radio burst velocity versus HXR spectral index. taken from Reid & Kontar (2018)

1.11 Thesis Outline

The research presented in this thesis attempts to further current understanding of the nature and characteristics of particle acceleration in solar flare emission and provide new techniques for measuring the coronal magnetic field in the corona as well as relating the populations of electrons we see producing radio and x-ray emission.

In Chapter 2, relevant theoretical background for the research is outlined including an overview of solar flare emission mechanisms and currently proposed mechanisms for the generation of QPPs and solar S-bursts. In Chapter 3 the observational instruments used for this work are described.

In Chapter 4 a statistical study of solar S-bursts is conducted and evidence is provided showing that these bursts can act as a tool for remote sensing the coronal magnetic field. In Chapter 5, we present work showing how quasi periodic pulsations in flares can be extremely broad band and attributed to bursty magnetic reconnection that results in intermittent particle acceleration.

In Chapter 6, we build upon this by conducting further work relating x-rays and radio emission to the same population of accelerated electrons using state of the art

instrumentation. Finally, in Chapter 7 we provide a summary and conclusion of the results in this thesis and explore future work.

2

Theory

In this chapter, the theory underpinning the work of this thesis is presented. Given the sun is composed of plasma, its physics are first introduced. Maxwell's equations are then outlined before the framework of magnetohydrodynamics, which describes the dynamics of plasma in a magnetic field, is discussed. The leading theory describing the mechanism through which the magnetic energy of the sun is converted into thermal and kinetic energy, known as magnetic reconnection, is then explored before relating these concepts to particle acceleration and solar flare emission mechanisms. The mechanisms that give rise to the coherent radio emission we observe in the form of solar radio bursts are presented, as well as the theory behind the generation of HXRs at flare sites. The leading theories of QPP and S-burst generation are then provided.

2.1 Plasma Physics

In the 1920's, Irving Langmuir showed that ionised gases can support oscillations that appear 'jelly-like', and described this state of matter as a *plasma*. The electromagnetic force is responsible for holding atoms and molecules together. This force yields the structures we are most familiar with, such as solid matter. These structured systems having binding energies that exceed the local ambient thermal energy. However, if we heat the environment, these structure begin to decompose. If enough thermal energy is introduced into the system, the temperature can approach, and even exceed, the atomic ionisation energies of the matter the system is composed of. Even if a small proportion

of the system becomes ionised, splitting into ions and electrons, the behaviour of the system can become subject to to electric, magnetic, and other forces. Such a system would then exhibit collective behaviour, distinct from a completely neutral gas, this is termed a plasma.

It is believed that perhaps 95% of the baryoninc matter of the Universe is in a plasma state. This illustrates the importance of understanding fundamental plasma physics. Stars, nebulae, and interstellar space are composed of plasma and act as massive remote laboratories for us to observe their behaviour. Hence, it important that some introductory plasma theory relevant to this thesis is introduced. Below, we introduce Maxwell's equations which describe the behaviour of electric and magnetic fields and how they relate to one another. Single particle motion is also introduced.

2.1.1 Maxwell's Equations & Single Particle Motion

Maxwell's equations of electromagnetism are given by the following

$$\nabla \cdot \mathbf{E} = \frac{\rho}{\epsilon_0} \tag{2.1}$$

$$\nabla \cdot \mathbf{B} = 0 \tag{2.2}$$

$$\nabla \times \mathbf{E} = -\frac{\partial \mathbf{B}}{\partial t} \tag{2.3}$$

$$\nabla \times \mathbf{B} = \mu_0 \mathbf{J} + \mu_0 \epsilon_0 \frac{\partial \mathbf{E}}{\partial t} \tag{2.4}$$

where $\mathbf{E}$ is the electric field, ρ is the charge density, ϵ_0 is the permittivity of free space, $\mathbf{B}$ is the magnetic field, μ_0 is the permeability of free space, and $\mathbf{J}$ is the current density. Equation 2.1, known as Gauss' Law, describes that the electric flux out of a closed surface is proportional to the enclosed charge. In other words the divergence of the electric field is proportional to the charge density.

To understand the concept of divergence in a qualitative sense, one can imagine what it describes in terms of fluid flow. Using this analogy, a positive value of the divergence evaluated at some point in the field would indicate that there is a net outward flow of fluid from that point, while if the value were negative it would indicate that there is a net inward flow of fluid at that point. Equation 2.1 simply describes that regions of the field containing a high value of electric charge density yield large values of outwardly/inwardly directed electric flux (depending in the sign of the charge).

Equation 2.2 states that the magnetic field has a divergence equal to zero. This is a consequence of the fact that magnetic monopoles do not exist. As magnetic field lines are continuous between the poles, all closed surfaces have as many field lines going in as coming out, resulting in zero divergence.

Using fluid flow once more as an analogy, the curl at a given point describes how much a fluid tends to rotate around that point. If one imagines dropping a twig into a fluid, if it spun around in a clockwise fashion that region would be said to have a positive curl, while if it spun anticlockwise it would be said to have a negative curl. Equation 2.3 and Equation 2.4 describe how the way the $\mathbf{E}$ or $\mathbf{B}$ fields change with time depends on the curl of the other field. Equation 2.3 is known as Faraday's law while Equation 2.4 is known as Ampère's Law with Maxwell's addition. Faraday's law is stating that a spatially varying electric field always accompanies a time-varying magnetic field. Ampère's law with Maxwell's addition states that a spatially varying magnetic field can be generated by electric current and by time-varying electric fields. These two laws give rise to electromagnetic waves. For non-relativistic speeds, as in the case of the framework of magnetohydrodynamics (see Section 2.2), the displacement current is negligible and so Equation 2.4 reduces to the following.

$$\nabla \times \mathbf{B} = \mu_0 \mathbf{J} \tag{2.5}$$

As plasmas are composed of charged particles, the role of electrical and magnetic forces are clearly important to their behaviour. The force, $\mathbf{F_L}$, experienced by a particle with charge, q, moving through a region containing a magnetic field, $\mathbf{B}$, and an electric

field, $\mathbf{E}$, with a velocity, $\mathbf{v}$, is given by

$$\mathbf{F_L} = q\mathbf{E} + q\mathbf{v} \times \mathbf{B}. \tag{2.6}$$

This force, $\mathbf{F_L}$, is known as the Lorentz force. Using Newton's second law, the rate of change of momentum of a particle with mass, m, is given by

$$m\frac{d\mathbf{v}}{dt} = q\mathbf{E} + q\mathbf{v} \times \mathbf{B} + \mathbf{F_g} \tag{2.7}$$

where $\mathbf{F_g}$ represents non electromagnetic forces such as gravity. Oftentimes these non-electromagnetic forces can be neglected, so for now, we can assume $\mathbf{F_g} = 0$.

In a uniform magnetic field with $\mathbf{E} = 0$, Equation 2.7 becomes

$$m\ddot{\mathbf{v}} = \left(\frac{q\mathbf{B}}{m}\right)\mathbf{v} \tag{2.8}$$

implying that in such cases, a charged particle moves in a circular motion in the left hand sense if $q > 0$ and the right hand sense if $q < 0$. The angular frequency of the particle, Ω_c is given by

$$\Omega_c = \frac{qB}{m} \tag{2.9}$$

which is known as the *cyclotron frequency* or the *gyrofrequency*. The radius of the circle the particle traverses is known as the *Larmor radius* or *Gyroradius* and is determined by the component of the particles velocity that is perpendicular to the magnetic field, $v_\perp$. This quantity is given by the following.

$$\rho_c = \frac{v_\perp}{\Omega_c} = \frac{mv_\perp}{qB} \tag{2.10}$$

If we now introduce an $\mathbf{E}$ field perpendicular to the $\mathbf{B}$ field, the response of a charged particle is quite different. Figure 2.1 shows schematically how an electron and ion would move in such a set-up. The electrical force accelerates the particle for part

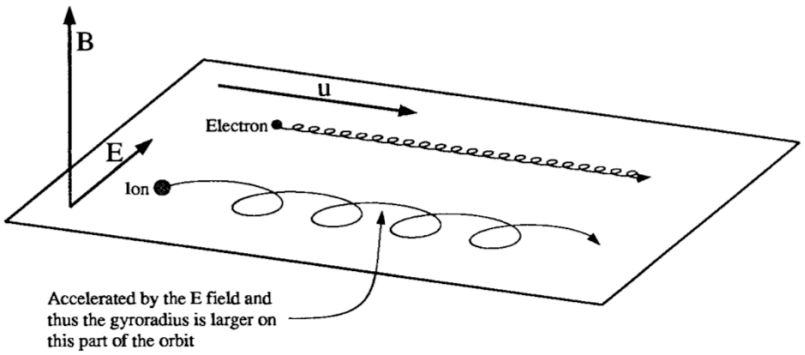

Figure 2.1: Schematic showing E-cross-B drift for ions and electrons in a uniform magnetic field with an electric field present that is perpendicular to the magnetic field. Taken from Kivelson & Russell (1995).

of the orbit and decelerates it for the remainder resulting in the distorted circle shown. The Larmor radius varies with mass and so the heavier ions vary in their trajectory over a longer distance. If we follow the gyrating motion of the particles in this system over many orbits, one can measure the particle drift velocity, $\mathbf{u_E}$, which is given by the equation below.

$$\mathbf{u_E} = \frac{\mathbf{E} \times \mathbf{B}}{B^2} \tag{2.11}$$

This describes that the drift velocity is perpendicular to both the **E** and **B** fields. This phenomenon is known as *E-cross-B drift*. More generally, any force, **F**, that is capable of accelerating charged particles as they gyrate about the **B** field, may result in drifts perpendicular to the field and force. This general expression is given by

$$\mathbf{u_F} = \frac{\mathbf{F} \times \mathbf{B}}{qB^2} \tag{2.12}$$

in which case the drift velocity direction will depend on whether the charge is positive or negative if the force is charge independent. This can give rise to the development of currents, $\mathbf{j}_\perp$, perpendicular to the magnetic field. For example, a gradient in the magnetic field can produce a force that gives rise to drifts resulting in currents across the **B** field. This *gradient drift velocity*, $\mathbf{u_g}$, is given by

$$\mathbf{u_g} = \frac{1}{2} m v_\perp^2 \tag{2.13}$$

An interesting feature of the motion of particles in collisionless plasmas is that their magnetic moment, μ, is conserved. This quantity is known as the first adiabatic invariant and is given below.

$$\mu = \frac{\frac{1}{2}mv_{\perp}^2}{B} \tag{2.14}$$

Given that this quantity must remain constant, it is necessary that acceleration must occur if a particle is traversing a non-uniform field. As a result, it can be shown that a particle travelling from a region of high magnetic field to a region of low magnetic field can undergo a processes known as *magnetic mirroring* and become trapped between two *mirror points*. However, under certain conditions, the particle may escape the magnetic mirror via the *loss cone* depending on the pitch angle of the particle.

2.2 Magnetohydrodynamics

The framework known as Magnetohydrodynamics (MHD), mentioned above, describes the collective large scale, slow dynamics of plasma in a magnetic field. In MHD, the plasma is considered an electrically conducting fluid and is governed by the equations of fluid dynamics coupled with Maxwell's equations. The full set of MHD equations connects a number of important plasma properties including the plasma mass density, ρ, the plasma velocity, $\mathbf{v}$, the gas or kinetic pressure, P, and the magnetic field, $\mathbf{B}$. MHD makes a number of assumptions which restricts its applications to situations in which

- The characteristic time >> the mean free path time and ion gyroperiod.
- The characteristic scale >> the mean free path scale and ion gyroradius.
- The plasma velocities are non-relativisitic.

These circumstances are applicable to the conditions of the solar atmosphere and hence it is relevant to introduce the equations of MHD here. Firstly, the ideal MHD equations are presented which neglect dissipative processes (finite viscosity, electrical resistivity and thermal conductivity) with the the magnetic field subject to Equation 2.2.

The first equation describes that matter is neither created or destroyed and is known as the equation of *mass continuity*. It is given by

$$\frac{\partial \rho}{\partial t} + \nabla \cdot (\rho \mathbf{v}) = 0 \tag{2.15}$$

and simply states that the rate of change of plasma density in a region is controlled by the fluid flow into or out of that region. Secondly we have the Euler equation which describes the motion of an element of the fluid given below.

$$\rho \frac{d\mathbf{v}}{dt} = -\nabla P - \frac{1}{\mu_0}\mathbf{B} \times (\nabla \times \mathbf{B}) \tag{2.16}$$

Next, there is the *energy equation* which for the simple adiabatic case is given by

$$\frac{d}{dt}\left(\frac{P}{\rho^\gamma}\right) = 0 \tag{2.17}$$

where γ (ratio of specific heats) is usually taken as 5/3. One can determine the plasma temperature via the density and thermodynamic pressure, P, via the state equation which for a pure hydrogen plasma is

$$P = 2\frac{k_B}{m_p}\rho T \tag{2.18}$$

where k_B is Boltzmann's constant and m_p is the proton mass. To reach the next equation of ideal MHD one can first consider Ohm's law

$$\mathbf{j} = \sigma \mathbf{E}' \tag{2.19}$$

where σ is the electrical conductivity and $\mathbf{E}'$ is the electric field felt by an element of the plasma in its rest frame. Applying the Lorentz transformation, $\mathbf{E}'$ can be written as the following.

$$\mathbf{E}' = \mathbf{E} + \mathbf{v} \times \mathbf{B} \tag{2.20}$$

Subbing Equation 2.20 into Equation 2.19 we get

$$\frac{1}{\sigma}\mathbf{j} = \mathbf{E} + \mathbf{v} \times \mathbf{B} \tag{2.21}$$

which simplifies to

$$\mathbf{E} = -\mathbf{v} \times \mathbf{B} \tag{2.22}$$

for the ideal case of perfect conductivity when $\sigma \to \infty$. Taking the curl of both sides and using our knowledge of the curl of the electric field from Maxwell's equations (Equation 2.3) and simplifying to exclude the electric field we reach the *induction equation*, shown below.

$$\frac{\partial B}{\partial t} = \nabla \times (\mathbf{v} \times \mathbf{B}) \tag{2.23}$$

The phenomenon of the magnetic dynamo is described by the induction equation. Equation 2.15, Equation 2.16, Equation 2.17, and Equation 2.23 form the ideal MHD equations.

The static equilibrium conditions for MHD are that $\mathbf{v} = 0$ and $\partial/\partial t = 0$. Under these conditions, Equation 2.16 becomes

$$-\nabla P - \frac{1}{\mu_0}\mathbf{B} \times (\nabla \times \mathbf{B}) = 0 \tag{2.24}$$

which when simplified and supplemented with the condition that $\nabla \cdot \mathbf{B} = 0$ yields the following expression.

$$-\nabla \left(P + \frac{B^2}{2\mu_0} \right) + \frac{1}{\mu_0}(\mathbf{B} \cdot \nabla)\mathbf{B} = 0 \tag{2.25}$$

The first term, $P + B^2/2\mu_0$, accounts for the total pressure. P is the gas, or thermodynamic pressure, while $B^2/2\mu_0$ is the magnetic pressure. The second term is the magnetic tension which is a force that acts to restore a curved magnetic field line to a straight line. The ratio of the gas pressure and the magnetic pressure is known as the

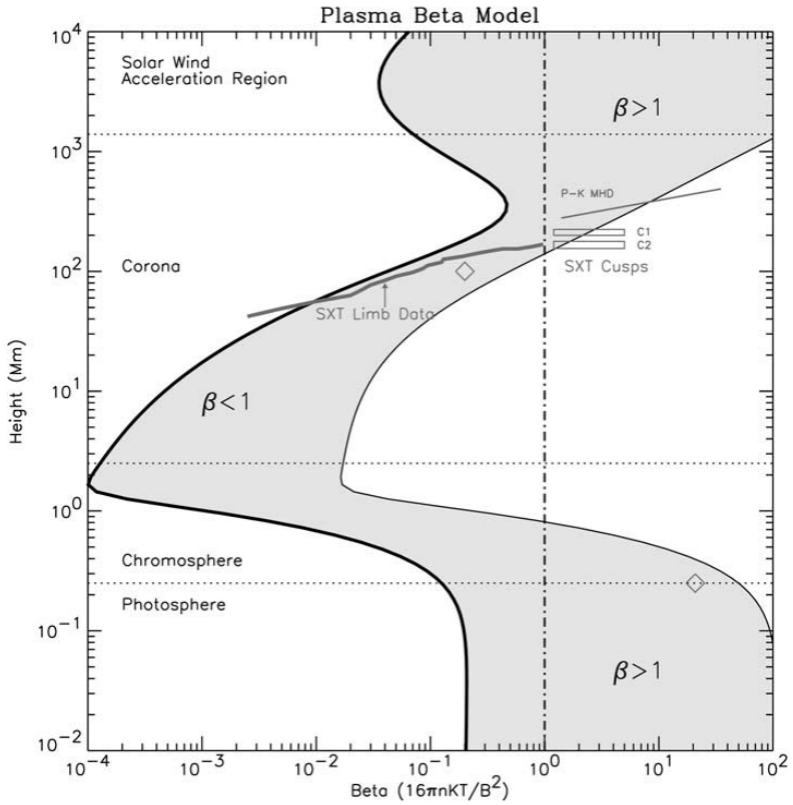

Figure 2.2: Plasma β model of the solar atmosphere. Shown in the shaded region are plasma β values as a function of height for open and closed field lines originating between a sunspot of 2500 G and a plage region of 150 G. Taken from Gary (2001).

plasma-β parameter.

$$\beta = \frac{P}{B^2/2\mu_0} \tag{2.26}$$

For values of $\beta << 1$ the magnetic pressure dominates and the gas follows the magnetic field lines in the plasma while for $\beta >> 1$ the gas pressure dominates freezing the magnetic filed lines into the plasma motion. As referenced in the Introduction of this thesis, high β values are located at the solar photosphere and below while the corona exhibits low β values. Figure 2.2 shows a model of how the plasma β parameter can vary as a function of height in the solar atmosphere illustrating at which altitudes the gas or magnetic pressure dominates.

If dissipative effects, such as magnetic diffusivity, are accounted for, the aforementioned set of ideal MHD equations become the following non-ideal set.

$$\rho\frac{\partial \mathbf{v}}{\partial t} + \rho(\mathbf{v}\cdot\nabla)\mathbf{v} = -\nabla P - \frac{1}{\mu}B\times\nabla\times\mathbf{B} + \mathcal{F} \tag{2.27}$$

$$\frac{\partial \mathbf{B}}{\partial t} = \nabla \times (\mathbf{v} \times \mathbf{B}) + \eta \nabla^2 \mathbf{B} \tag{2.28}$$

$$\frac{\partial \rho}{\partial t} + \nabla \cdot (\rho \mathbf{v}) = 0 \tag{2.29}$$

$$\frac{\rho^\gamma}{\gamma - 1} \frac{d}{dt} \left(\frac{P}{\rho^\gamma} \right) = -\mathcal{L} \tag{2.30}$$

$$\nabla \cdot \mathbf{B} = 0 \tag{2.31}$$

Here, η represents magnetic diffusivity, $\mathcal{F}$ represents an external force acting on a unit of volume of the plasma such as gravity, and $\mathcal{L}$ is the energy loss/gain function. A highly important diffusive process thought to be the source of energy release in solar flares is known as *magnetic reconnection*, which will discussed in Section 2.4.

2.3 MHD Waves

Plasmas can support a variety of different types of waves. Evidence for the presence of MHD waves in the solar corona is supported by numerous observations. Analysing the properties of these waves enables us to probe plasma properties. One example is the usual sound wave that would be encountered in hydrodynamics. Others, known as magnetosonic waves, are essentially hybrids of sound waves and the Alvèn waves. Alvèn waves are transverse waves that arise exclusively from the magnetic field and for which the restoring force is magnetic tension.

MHD waves are driven by various restoring forces that occur when the plasma is perturbed. The process of deriving the equations of MHD waves involves introducing small perturbations, in properties such as the plasma pressure, density and magnetic field, and then subbing these into the MHD equations. The equations are linearised and solved in order to obtain dispersion relationships. The dispersion relations inform us about the relationship between the wave's wavelength and its velocity. The classic

example of dispersion is of white light passing through a prism. In this case, the light splits and its velocity changes depending on the wavelength. Sound waves are non dispersive, meaning that their velocity is remains constant no matter the wavelength. MHD waves can play a role in triggering magnetic reconnection in active regions or modulating electromagnetic emission in flares which is discussed in Section 2.8.

The dispersion relations for Alvèn waves and magnetoacoustic waves are given by the next two equations, respectively.

$$\omega^2 - v_A^2 k_z^2 = 0 \tag{2.32}$$

and

$$\omega^4 - k^2(c_S^2 + v_A^2)\omega^2 + k_z^2 k^2 c_S^2 v_A^2 = 0 \tag{2.33}$$

Here, $\mathbf{k} = (k_x, k_y, k_z)$ is the wavenumber and ω is the angular frequency. Two characteristic wave speeds of MHD are introduced in these dispersion relations. Firstly, there is the sound speed $c_S = \sqrt{\gamma p_0/\rho_0}$ where γ is the ratio of specific heats, ρ_0 is the background density and P_0 is the background pressure. Secondly, there is the Alvèn speed $v_A = B_0/\sqrt{\mu_0\rho_0}$ where B_0 is the background magnetic field. Equation 2.33 has two solutions which give rise to the *fast* and *slow* magnetoacoustic waves.

2.4 Magnetic Reconnection

The main driving force of all solar activity is thought to be a consequence of the energy release mechanism known as magnetic reconnection. The energy release process in flares is likely due to this process as discussed in Section 1.5.1. Magnetic reconnection liberates the stored magnetic energy that builds up in the solar atmosphere by relaxing from a more complex topological magnetic configuration to a simpler, lower energy state. Coronal mass ejections, jets and other dynamic solar phenomena are also believed to be caused due to this mechanism. In Chapter 5, I present work that provides observational evidence and analysis that shows that magnetic reconnection can occur

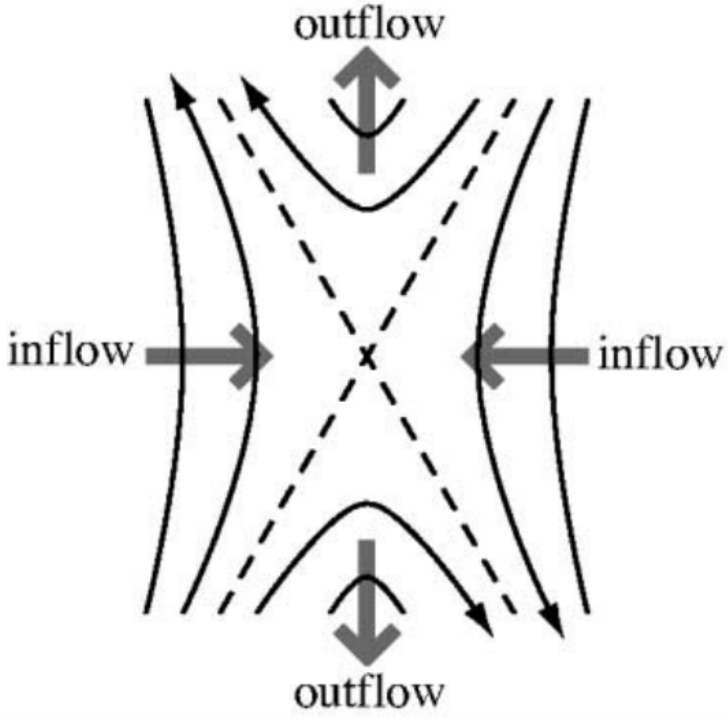

Figure 2.3: Idealised two-dimensional magnetic reconnection taken from Brown et al. (2002). Shown are two in-flowing magnetic field lines of opposite polarity. These reconnect and are convected away in the outflow regions.

in a quasi-periodic fashion leading to time-dependent, or bursty, energy release and particle acceleration in flares. Many models of reconnection have been proposed and this area of research remains active. Here, a short introduction to the phenomenon is provided.

Figure 2.3 shows an idealised 2D magnetic reconnection model where two in-flowing magnetic field lines of opposite polarity reconnect and are convected away in the outflow regions (Brown et al., 2002). The dashed lines are separatrices distinguishing the four topologically distinct regions. A layer of current density is centered at the *X-point*. The central area where the field lines of opposite polarity interact is known as the *diffusion region*. Modifying the induction equation (Equation 2.28) for the scenario in which diffusion dominates over advection we have

$$\frac{\partial \mathbf{B}}{\partial t} = \eta \nabla^2 \mathbf{B} \tag{2.34}$$

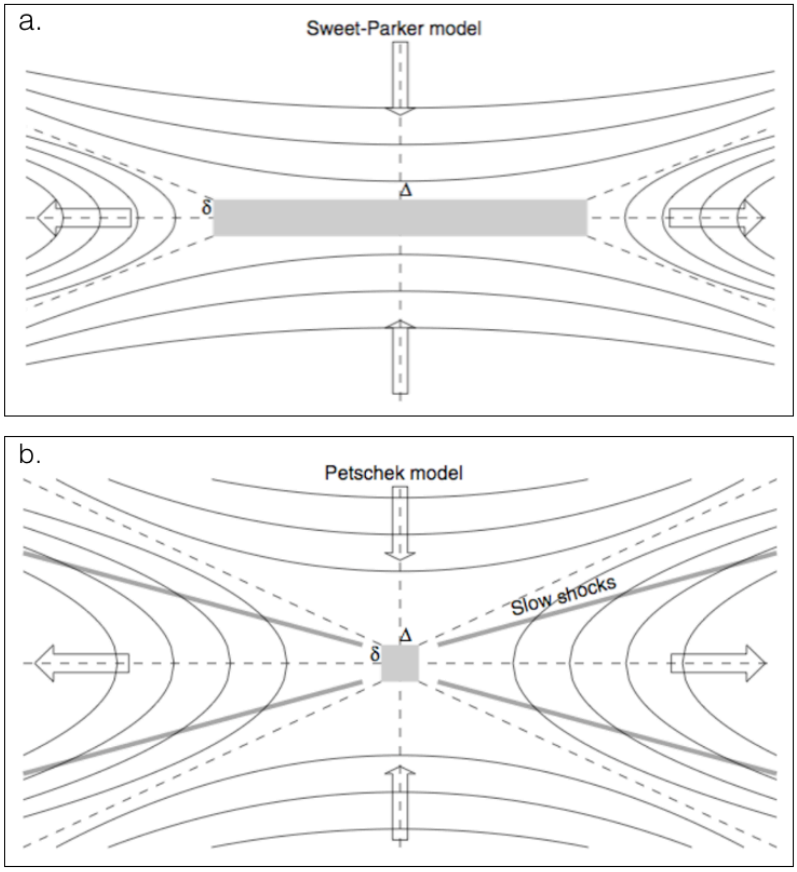

Figure 2.4: (a): Diagram of the Sweet-Parker model of magnetic reconnection. In this model, a long thin diffusion region is employed ($\Delta >> \delta$). (b): The Petschek model for which the diffusion region is smaller ($\Delta \approx \delta$). The Petschek also accounts for slow mode shocks in the dissipation of energy. Adapted from Aschwanden (2004).

which can then, when combined with some approximations, provide an estimate for the timescale of the magnetic diffusion process, τ_D. This is given by

$$\tau_D \approx \frac{L^2}{\eta} \tag{2.35}$$

where L is the length scale over which there are variations in the magnetic field. Energetic solar events like flares and CMEs involve impulsive energy release that occurs over periods of minutes. Therefore, as $\tau \propto L^2$, the length-scale over which reconnection occurs must be short implying small regions of high magnetic diffusivity.

The Sweet-Parker model (Parker, 1963; Sweet, 1958) was the first proposed MHD mechanism through which magnetic reconnection could occur. This model provided a framework to calculate important parameters of magnetic reconnection such as the

reconnection rate. This describes the rate at which magnetic flux is converted into thermal and kinetic energy. The top panel of Figure 2.4 shows a diagram of the Sweet-Parker model. This model assumes the diffusion region is much longer than it is wide ($\Delta >> \delta$). The continuity equation then gives rise to the following relationship

$$\rho_{in} v_{in} \Delta = \rho_{out} v_{out} \delta \tag{2.36}$$

where ρ_{in} and v_{in} are the inflow density and inflow velocity. ρ_{out} and v_{out} are the outflow density and outflow velocity. This relation then leads to the predicted reconnection rate, M, implied by the Sweet-Parker model given by

$$M = \frac{v_{in}}{v_{out}} = \frac{1}{R_m} \tag{2.37}$$

where R_m is the magnetic Reynolds number (or Lundquist number when using the Alfvèn speed). This parameter encapsulates the relative imporatance of the magnetic advection and diffusion terms in the induction equation (Equation 2.28). If we input a typical value of R_m that one would expect in the solar corona ($10^8 - 10^{12}$) into Equation 2.37, it outputs a timescale $10^8 - 10^9$ years. This is clearly far longer than the time-scale of solar eruptions which occur occur over a period of minutes or less. The Sweet Parker is hence too slow to account for the reconnection rates we expect from solar observations.

This Petschek model was then developed in an attempt to yield shorter reconnection rates comparable to observations. The bottom panel of Figure 2.4 shows a diagram of the Petschek model. The diffusion region in this case is much smaller ($\Delta \approx \delta$) and slow mode shocks are accounted for in the dissipation of energy. The compact diffusion region in this model resulted in a new expression for the reconnection rate given by

$$M \approx \frac{\pi}{8 \ln(R_m)} \tag{2.38}$$

which yields reconnection time-scales of ~ 70 s using typical values of R_m for coronal

conditions. This is comparable to the times-scale of flares and other solar eruptive events.

Certain geometries of the diffusion region, such as cases when it gets particularly long, can give rise instabilities leading to a regime of impulsive *bursty reconnection*. In solar flares, observations of intermittent pulses of hard X-rays as well as radio signatures of intermittent particle acceleration, provide evidence for such a regime (Infeld, 2001). Some specific models of bursty reconnection are outlined in Section 2.8. Chapter 5 presents a case study for which strong evidence that this type of bursty reconnection is occurring which manifests in broad band electromagnetic quasi periodic pulsations (QPPs). The electromagnetic emission from each waveband in this study emanates in multiple spatial regions associated with the flare site, such as the chromospheric footpoints (HXRs), the flare loops (SXRs and EUV), and interplanetary space (low frequency radio emission). Linking these pulses of different radiation to the same energy release mechanism and position, as well as the same population of accelerated particles is a major theme of Chapter 5.

2.5 Particle Acceleration

The previous section outlines how magnetic reconnection provides a mechanisms through which stored magnetic energy can be released, resulting in the acceleration of particles to non-thermal energies. It also produces thermal energy which heats the surrounding plasma. In the context of solar flares, there are a number of particle acceleration mechanisms at play once magnetic reconnection occurs. An example of such a mechanism is electric field acceleration.

The application of strong electric fields ($\mathbf{F} = q\mathbf{E}$) is the simplest way in which particles can be accelerated. When this acceleration occurs as a result of magnetic reconnection, the injected non-thermal particles can cause instabilities in the plasma. HXRs can be then be produced via Bremsstrahlung as the particles collide with the denser chromosphere, while Type III radio bursts and S-bursts can be produced as they escape at sub-relativistic speeds towards interplanetary space along open magnetic field

lines. Analysing the properties and origin of these radio bursts form a key component of the work presented in Chapters 4, 5, and 6.

The aforementioned electric fields arise due to reconnection occurring in the *current sheet*. A current sheet is a term used for the plane located between the magnetic field lines of opposite polarity in a reconnection scenario (see central region of Figure 2.4a). The plasma and magnetic field that flows into the diffusion region is accelerated outwards in the outflow region by an induced electric field (Zharkova & Gordovskyy, 2004). Rearranging Equation 2.21, this electric field can be written as the following.

$$\mathbf{E} = \frac{\mathbf{J}}{\sigma} - \mathbf{v} \times \mathbf{B} \tag{2.39}$$

Applying Ampère's law then yields

$$\mathbf{E} = \eta \nabla \times \mathbf{B} - \mathbf{v} \times \mathbf{B} \tag{2.40}$$

where the first term dominates in the diffusion region and the second term ($\mathbf{v} \times \mathbf{B}$) dominates outside the reconnecting current sheet. This is due to the electric field remaining constant in both regions. Acceleration occurring simply due to the Lorentz force ($\mathbf{v} \times \mathbf{B}$ term) can result in particles obtaining energies of $\sim$100 keV (Litvinenko, 1996). Coherent radio emission can then manifest in the form of solar radio bursts as a result of this particle acceleration. Plasma emission is thought to be the way in which Type III bursts are generated from these accelerated particles (primarily electrons). S-bursts are also thought to generated via a form of plasma emission.

2.6 Solar Flare Emission Mechanisms

In this section, the main solar flare emission mechanisms associated with particle acceleration resulting in the generation of solar radio bursts and HXRs will be discussed. Firstly, the coherent radio emission mechanism known as plasma emission is outlined. Another coherent radio emission mechanism, known as electron cyclotron maser (ECM)

emission is also briefly touched upon in Section 2.7 in discussing proposed S-bursts emission mechanisms. Secondly, the collisional thick target model which describes how HXRs arise in the standard flare model is discussed. The reader is referred to the many reviews available for more information on the additional incoherent mechanisms (Bastian et al., 1998; Nindos, 2020).

2.6.1 Plasma Emission

Ginzburg & Zhelesniakov (1958) first proposed the plasma emission mechanism as an explanation for how low frequency radio bursts are generated. The electrons within a plasma can convert their energy into Langmuir waves or electron cyclotron waves. Langmuir waves rapid oscillations of the electron density in the plasma. These waves can interact with one another or be scattered off of ion-sound waves. These processes can produce radio emission at the local plasma frequency, f_p, or its harmonics. A flowchart of the general process, beginning with the accelerated electron beam, is provided in Figure 2.5 (Melrose, 1991).

As mentioned in Section 2.4, particle acceleration may occur as a result of magnetic reconnection. This can accelerate accelerate beams of electrons along magnetic field lines both towards the solar surface and out towards interplanetary space. In a collisionless plasma, the injected energetic electron beam induces an instability in the particle distribution function. This is known as a *bump-on-tail* instability. The result of this instability is that the previously Maxwellian electron velocity distribution gains a *bump* at higher velocities as shown in Figure 2.6 (Melrose et al., 2021).

Once this instability is established, the free energy can be removed via the generation of Langmuir waves. The rate of growth of these plasma oscillations is proportional to the slope of the bump-on-tail. The Langmuir waves grow, interact with other waves in the environment, and eventually remove the positive slope of the instability. The coalescence of the various waves produced in this scenario can result in the generation of electromagnetic radiation.

In describing the coalescence of certain waves, Langmuir waves will be labelled

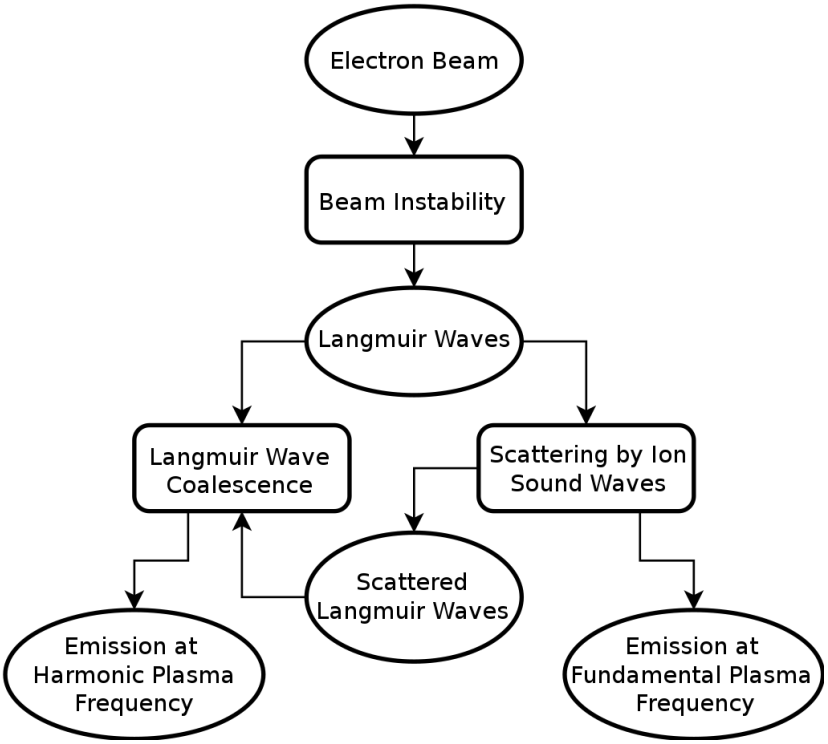

Figure 2.5: Flowchart showing the stages of plasma emission. The process begins with the acceleration of an electron beam that eventually yields the generation of fundamental or harmonic transverse waves. Adapted from Melrose (1991).

L, ion sound waves will be labelled S, and transverse electromagnetic waves will be labelled T. Scattered waves will be labelled with a dash, such as L' for a scattered Langmuir wave. The process which leads to the generation of electromagnetic waves at the fundamental plasma frequency is given by

$$L + S \rightarrow T \tag{2.41}$$

while the second harmonic can be generated via the following.

$$L + L' \rightarrow T \tag{2.42}$$

Scattered Langmuir waves arise from interactions such as $L + S' \rightarrow L'$. Three wave interactions can also occur resulting in emission at the third harmonic, however, this is rare.

The dispersion relations for Langmuir waves ω_L, ion sound waves ω_S, and transverse

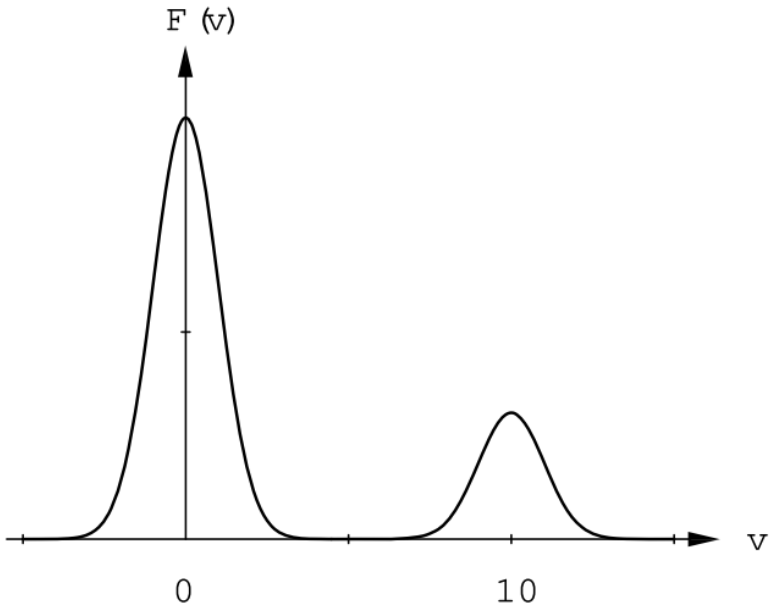

Figure 2.6: Velocity distribution showing a bump-on-tail instability at high velocities due to the injection of accelerated electrons. Taken from Melrose et al. (2021)

waves ω_T, are given by the following equations, respectively.

$$\omega_L^2 = \omega_p^2 + \frac{3}{2}k^2 v_{th}^2 \tag{2.43}$$

$$\omega_S^2 = k v_S \tag{2.44}$$

$$\omega_T^2 = \omega_p^2 + k^2 c^2 \tag{2.45}$$

In order for the processes described by Equation 2.41 and Equation 2.42 to occur, the frequencies and wave numbers of the involved waves need to combine appropriately. For example, for fundamental plasma emission $\omega_L + \omega_S$ must equal ωT. Given that Langmuir waves are plasma oscillations that have frequencies of ω_p and $\omega_p \approx \omega_L \approx \omega_T$ for fundamental plasma emission, it is necessary that the ion sound waves are very low frequency relative to the Langmuir waves. Such considerations of the coalescence of certain waves are explored in Chapter 4 when investigating the feasibility of models proposed for the generation of solar S-bursts.

2.6.1.1 The Plasma Frequency

To derive the plasma frequency, consider a plasma containing an equal number of positive and negative charges. Displacing a group of electrons by a distance δx results in the onset of an electric field, E, due to the charge separation. The displaced electrons would then accelerate towards their initial positions. However, they would overshoot their equilibrium positions setting up an oscillation. Using Newton's second law we have

$$m_e \frac{d^2 \Delta x}{dt^2} = eE \tag{2.46}$$

where e is the electron charge, m_e is the electron mass, and E is the electric field induced by the displaced electrons. This situation is similar to that of a parallel plate capacitor where the electric field between the two plates is given by $E = \sigma/\epsilon_0$. Here σ is the electron charge density and ϵ_0 is the permittivity of free space. The charge density in this scenario is simply given by $\sigma = -ne\Delta x$. Equation 2.46 can therefore be written as

$$m_e \frac{d^2 \Delta x}{dt^2} = eE = -\left(\frac{ne^2}{m_e \epsilon_0}\right) \Delta x = -\omega_p^2 x \tag{2.47}$$

where ω_p is the plasma frequency. The plasma oscillates at this frequency in order to try and maintain charge neutrality. By substituting in the known physical constants, the expression can be written as

$$f_p = \frac{\omega_p}{2\pi} \approx 8980\sqrt{n_e} \tag{2.48}$$

where f_p is in units of Hz and n_e is the electron density in units of cm^{-3}. It is clear that the plasma frequency is solely dependant on the local electron density. The electron density in the corona decreases as a function of height. However, the electron density is lower over coronal holes (Gallagher et al., 1999) and higher above active regions (Fludra et al., 1999). Therefore, with the aid of an appropriate electron density model, the height of a radio source produced via plasma emission can be estimated.

For example, if a type III radio burst is observed with frequency f_i at a time t_i,

Equation 2.48 can be used to transform from $(f_i, t_i) \rightarrow (n_i, t_i)$. An electron density model, such as the model put forward by Newkirk Jr. (1961) (see Figure 1.11), can then be used to transform from $(f_i, t_i) \rightarrow (r_i, t_i)$ where r is the distance from sun center to the source of the radio emission. The radial velocity of the source electrons producing a radio burst via plasma emission can therefore also be estimated by the *drift rate*, df/dt, of the burst. S-bursts and type III radio bursts typically have negative drift rates indicating that their source electrons are propagating away from the solar surface towards interplanetary space, from regions of high density to regions of low density. However, reverse drift bursts are also observed in rare cases.

2.6.2 X-ray Regime - Collisional Thick Target Model

Bremsstrahlung emission is an incoherent type of free-free emission that occurs when charged particles are accelerated due to a deflection imposed by another charged particle. In fact, the German word 'bremsstrahlung' translates to 'breaking radiation' which is evidently an appropriate name. When charged particles are directly approaching one another, an electron or ion can deviate significantly from its path or even reverse its direction. This typically produces radiation in the X-ray portion of the electromagnetic spectrum as a consequence (Gary, 2012). The HXRs we observe during flares are a consequence of electrons accelerating downwards along the coronal loops where they collide with the dense chromosphere at the footpoints (as shown in Figure 1.13). In the case of radio emission, it is the more gentle deviations that electrons experience from interactions with more distant ions that produce the radiation.

The Collisional Thick Target Model (Brown, 1971) describes how the HXR emission rate spectrum, $I(\epsilon_x)$, relates to the distribution of injected electrons $f_0(\epsilon_0)$. $I(\epsilon_x)$ has units of: photons cm^{-3} s^{-1} keV^{-1}. The bremsstrahlung cross-section, $\sigma(\epsilon,\epsilon_x)$, is a measure of the probability that an electron with energy ϵ will interact with a positively charged particle, resulting in the emission of a photon with energy ϵ_x. The HXR

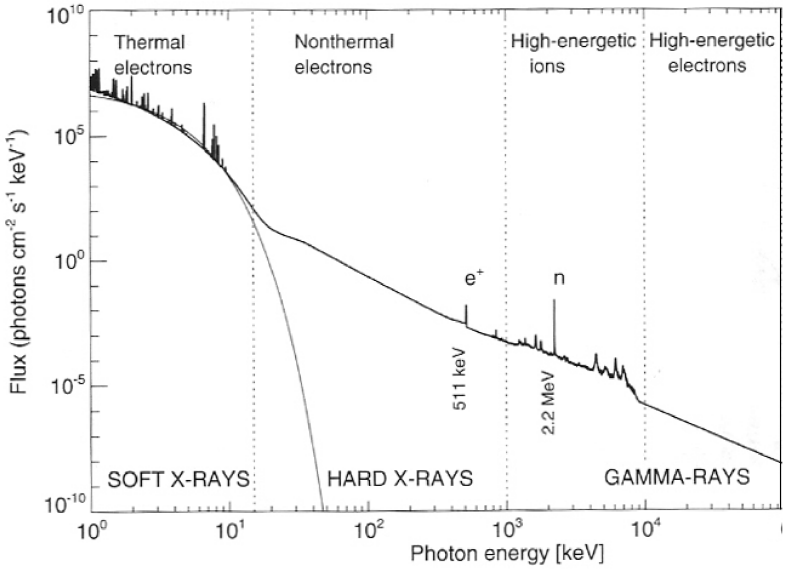

Figure 2.7: Typical solar flare spectrum at X-ray energies showing the power law form for the non-thermal regime. Taken form Aschwanden (2005).

emission rate spectrum observed at a distance r is given by

$$I(\epsilon_x) = \frac{1}{4\pi r^2} \int_{\epsilon_x}^{\infty} f_0(\epsilon_0) \left(\int_{t(\epsilon=\epsilon_0)}^{t(\epsilon=\epsilon_x)} \sigma(\epsilon, \epsilon_x) v(\epsilon) n(\epsilon) dt \right) d\epsilon_0 \tag{2.49}$$

where $v(\epsilon)$ is the electron velocity and $n(\epsilon)$ is the electron density. ϵ_0 is the electron energy at the time of injection. The integral within the parentheses accounts for the total number of electrons that emit a photon with an energy ϵx as they brake.

Modern instrumentation enables us to observe the HXR emission rate spectrum. However, it is desirable to use these observations in combination with models, such as the collisional thick target model discussed here, to extract the electron distribution function. Once the electron distribution function is known, it is possible to analyse and extract physical properties. For example, if the electron energies responsible for producing the HRXs are known, it is possible to compare them to the energy of the electrons responsible for producing type III radio bursts and determine if they are related populations of electrons. This idea is explored in Chapter 6.

The Brown (1971) model makes a number of assumptions in order to solve Equation 2.49 and determine the injected electron spectrum $f_0(\epsilon_0)$. These assumptions include that the energy losses of the electrons are due solely to collisions and that the

photon spectrum has a power law form with spectral index, γ. Figure 2.7 shows a plot from Aschwanden (2005) illustrating how non-thermal x-rays are typically observed to have this power law shape. Brown (1971) derived a solution for the electron injection spectrum given by the following.

$$f_0(\epsilon_0) = 2.56 \times 10^{33} \gamma^2 (\gamma - 1)^3 B\left(\gamma - \frac{1}{2}, \frac{3}{2}\right) \frac{I_1}{\epsilon_1^2} \left(\frac{\epsilon}{\epsilon_1}\right)^{-(\gamma+1)} \tag{2.50}$$

where I_1 is the reference photon flux at energy ϵ_1 and $B(a, b)$ is the Beta function given by

$$B(a, b) = \int_0^1 x^{a-1}(1 - x)^{b-1} dx \tag{2.51}$$

The proposed theories of S-burst and QPP emission mechanisms and now provided before concluding this chapter.

2.7 Proposed S-burst Emission Mechanisms

Melrose (1982) argued that S-bursts are a variation of what are known as drift pairs. Drift pairs appear on a dynamic spectrum as two narrow parallel traces that have approximately the same frequency, but are separated in time by 1-2 s. Drift pairs are observed in cases in which two rays are reflected from a duct wall. This theory suggests that under certain conditions, when only a single ray is produced, we observe an S-burst at Earth. This theory has largely been dismissed because of the work of Melnik et al. (2010) and others that pointed out that drift pairs have considerably longer durations than S-bursts and no functional dependence of frequency on drift rate.

Another model, put forward by Zaitsev & Zlotnik (1986), suggests that plasma waves near the upper hybrid resonance frequency are excited owing to electrons moving in a slightly anisotropic plasma within a quasihomogeneous magnetic field that have velocities of 10 to 20 times the thermal velocity of the local electrons. These plasma waves are then scattered by thermal ions to produce electromagnetic radiation at the local plasma frequency, f_p. The negative drift rate in this model is attributed to group

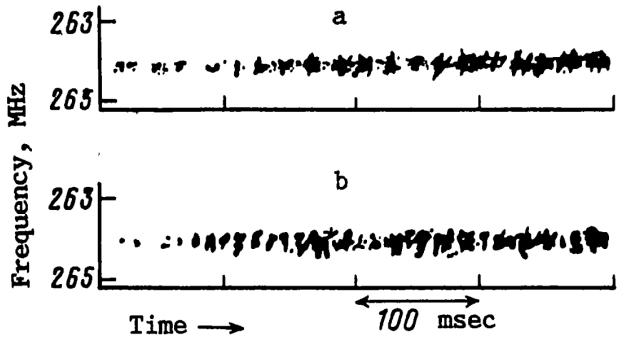

Figure 2.8: Sketch of bursts modelled by Zaitsev & Zlotnik (1986)

delay as the waves propagate outward from their point of origin. Figure 2.8 shows a sketch of the S-bursts modelled by Zaitsev & Zlotnik (1986) Melnik et al. (2010) argued that this model produces coronal inhomogeneity sizes and magnetic fields that are too large at heights corresponding to the local plasma frequency. Additionally, it implies a flatter drift rate dependence on frequency than follows from observations.

More recently, Melnik et al. (2010) proposed a new mechanism of S-burst generation involving beams of particles (electrons or protons) in resonance with right-hand (RH) circularly polarised waves. This takes place against a background of Langmuir turbulence. The RH waves interact with the Langmuir waves to produce radio emission close to the local plasma frequency. This model attempts to account for all of the properties of S-bursts that the group observed, especially the following: 1) S-bursts are always observed against the background of other radio activity such as type III and IIIb bursts. 2) S-burst sources move at velocities that are 5-9 times the thermal velocity of the local electrons. 3) The instantaneous bandwidth of the S-bursts increases linearly with frequency.

Using LOFAR, Morosan et al. (2015) observed that S-bursts may be associated with trans-equatorial loops that stretch to heights of $\sim$1.8 $R_{\odot}$. At such heights, it was noted that plasma emission is the most likely emission mechanism. However, it was observed that some of the properties of S-bursts, such as their relatively slow drift rates compared to type III bursts, narrow bandwidths, and short durations are indicative of electron cyclotron maser emission. The acronym MASER stands for Microwave

Amplification by Stimulated Emission of Radiation. The class of MASER relevant here can produce solar radio bursts at the gyrofrequency, as well as its lower harmonics McLean et al. (1978). This mechanism, known as Electron Cyclotron Maser (ECM) emission, requires the following conditions to occur.

- A population inversion in the local electron distribution.
- The gyrofrequency, ω_e, must be greater than the local plasma frequency, ω_p .

For the second condition to occur to occur the following must be true:

$$\Omega_e = \frac{eB}{m_e} > \omega_p = 2\pi f_p \tag{2.52}$$

where B is the magnetic field at the source height of the bursts. Therefore a relatively strong magnetic field or low electron density is required for ECM emission to occur. The magnetic field strength is given by

$$B = \frac{m_e \Omega_e}{e} \tag{2.53}$$

while the electron density is given by the expression below.

$$n_e = \frac{\omega_p^2 m_e \epsilon_0}{e^2} \tag{2.54}$$

Morosan et al. (2016) found that this condition is only satisfied at heights of $< 1.07\ R_\odot$ and frequencies > 500 MHz, indicating that ECM is not responsible for the generation of S-bursts. In Chapter 4 of this thesis, the spectral characteristics of solar S-bursts are investigated and used to analyse the feasibility of the Zaitsev & Zlotnik (1986) and Melnik et al. (2010) models outlined above. Evidence is then presented that suggests that one can use S-bursts to remote sense the coronal magnetic field at various altitudes. It has also been suggested that the presence of quasi periodic pulsations (QPPs) in solar flare emission may allow us to measure the coronal magnetic field. Proposed theories of how QPPs are generated are introduced below.

2.8 Quasi-Periodic Pulsation Mechanisms

In Section 1.9 of Chapter 1, it was discussed that the models put forward to explain the presence of QPPs in solar and stellar flares are categorised as oscillatory or self-oscillatory processes. The oscillatory mechanisms explain that QPPs are due to MHD oscillations inducing periodic motions in the flaring region which modulates the electromagnetic emission. This explanation has been promising for some events, as some observed periodicities of QPPs are in good agreement with that of the timescales of MHD waves in the corona (Nakariakov & Melnikov, 2009).

There is widespread observational evidence for MHD waves existing in the corona and it is possible that kink, toroidal, longitudinal, or sausage modes could cause some of the thermal and non-thermal intensity variations that we observe. For example, kink mode oscillations have been reported that have an overlapping timescale ($\sim$1.5-10 minutes) with observed QPP periodicities (Anfinogentov et al., 2015). Such waves could periodically modulate emission or influence particle dynamics (Nakariakov & Melnikov, 2009). It is also possible that the presence of these waves could trigger magnetic reconnection resulting in a periodicity related both to the type of wave mode involved and the properties of the coronal loops (Carley et al., 2019; Nakariakov & Zimovets, 2011). Figure 2.9 shows a sketch from Nakariakov & Melnikov (2009) illustrating this. QPPs are interpreted as a manifestation of time dependent, intermittent magnetic reconnection in the self-oscillatory regime. Specific mechanisms theorised to produce intermittently accelerated electron beams resulting in QPPs that are relevant to this thesis include plasmoid magnetic island reconnection and oscillatory reconnection (reconnection reversal). For example, Kliem et al. (2000) demonstrated in a 2D numerical model of a long current sheet that the formation of plasmoids and their coalescence could result in quasi-periodic particle acceleration, which they used to explain the presence of decimetric radio bursts with periods of 0.5-10s. In a more recent study, Guidoni et al. (2016) built upon the work of Drake et al. (2006) to show that the generation, contraction, and interaction of magnetic islands in a multi-layered current sheet

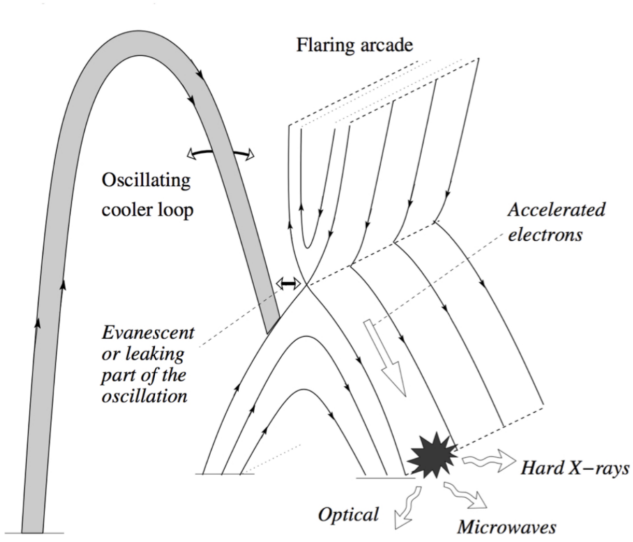

Figure 2.9: Schematic taken from Nakariakov & Melnikov (2009) showing an external loop hosting a periodic wave that is triggering reconnection in the flare site resulting in QPPs.

can efficiently accelerate charged particles. It was demonstrated that this mechanism should occur in a manner that is sporadic and intermittent, and hence would result in pulsating flare emission. The period in this case would be related to the rate of island formation and their interaction with the flaring arcade.

In addition to plasmoid-dominated reconnection models, numerical simulations have demonstrated that the reconnection process itself can be oscillatory. In this scenario of oscillatory reconnection, competition between the thermal-pressure gradients and the Lorentz force provide a restoring force as each aspect overshoots the other in search for equilibrium (e.g. McLaughlin et al., 2009; Murray et al., 2009). Simulations have shown that this mechanism can produce oscillatory reconnection which results in intermittent particle acceleration in a self-consistent manner resulting in decaying QPPs with periodicities of ∼105–212.5 s (McLaughlin et al., 2012). This work has also been extended to a 3D null-point, and it has been shown that reconnection can naturally proceed in a time-dependent oscillatory behaviour (Thurgood et al., 2017). The challenge in identifying an underlying mechanism responsible for generating QPPs is that they are linked to many aspects of flaring emission, and encompass electromagnetic emission that originates from the very base HXR footpoints of a flare up to altitudes of several

solar radii in the corona. Chapter 5 presents new evidence that bursty reconnection can produce QPPs that manifest across the electromagnetic from low frequency radio emission through to HXRs.

3

Instrumentation

A multitude of ground and space based observatories continually monitor the sun. Various instruments make observations within specific wavebands. Combining simultaneously observed datasets from these different instruments provides the multi-wavelength information required in order to investigate the topics presented in this thesis. For example, the discussed themes of QPPs in solar flares and the observational signatures of accelerated electrons required the use of X-ray, extreme-ultraviolet (EUV) and radio instrumentation. Observations from large ground-based radio telescopes known as The Low Frequency Array (LOFAR) and the Ukrainian T-shaped Radio Telescope (UTR-2) were used for the work contained in Chapter 4. The focus of this work was to investigate specific low frequency radio bursts, known as S-bursts. Data from the Irish LOFAR station, I-LOFAR, was also used in Chapter 6. The X-ray and γ-ray telescopes used in the work of Chapters 5 and 6 include the Ramaty High Energy Solar Spectroscopic Imager (RHESSI), the FERMI Gamma Ray Burst (GBM) monitor, the Geostationary Operational Environmental Satellite (GOES), and The Spectrometer/Telescope for Imaging X-rays (STIX). Data from The Atmospheric Imaging Assembly (AIA) onboard The Solar Dynamics Observatory (SDO) was used to analyse QPPs in the EUV regime while data from WIND/WAVES was used for radio analysis. In this Chapter, a brief overview of these instruments is outlined.

3.1 The Ramaty High Energy Solar Spectroscopic Imager (RHESSI)

The Ramaty High Energy Solar Spectroscopic Imager (RHESSI) was launched in 2002 as part of the NASA Small Explorer program with the primary objective of investigating the physics of particle acceleration and explosive energy release in solar flares (Lin et al., 2002). RHESSI observes X-rays and γ-rays in the the energy range of 3 keV to 17 MeV, providing data spanning both the thermal and non-thermal regimes solar flare emission. The imaging capabilities of RHESSI allow for the study of the positions and geometries of non-thermal sources, such as HXR footpoints, and thermal sources, such as SXR coronal loops, in flares. It has a maximum spatial resolution of 2.25 arcsec and spectral resolution of 1 keV at 3 keV, and up to 5 keV at 5 MeV.

RHESSI was decommissioned on the 16th August 2018 due to faults and degradation of its detectors and on-board receiver. Despite this, a wealth of historical data continues to be analysed further showcasing its utility to aid our understanding of processes such as reconnection, particle acceleration and energy transport. In Chapter 6 time-series data from RHESSI is used to investigate QPPs. In addition, RHESSI is used to indirectly image the HXR sources from which the QPPs originate in this work. Below, the mechanism through which RHESSI produces images is outlined. Figure 3.1 shows a schematic of the RHESSI instrument.

3.1.1 Imaging

Directly imaging X-ray sources using focusing optics is challenging as the high energy photons can scatter or penetrate the reflective surfaces or mirrors. Despite this challenge, innovative missions such as the *FOXI* solar sounding rocket campaigns have made strides towards incorporating new technologies enabling the use of space based direct imaging techniques for X-rays (Glesener et al., 2016). RHESSI utilises indirect Fourier imaging techniques in order to creates X-ray images (Hurford et al., 2002). To

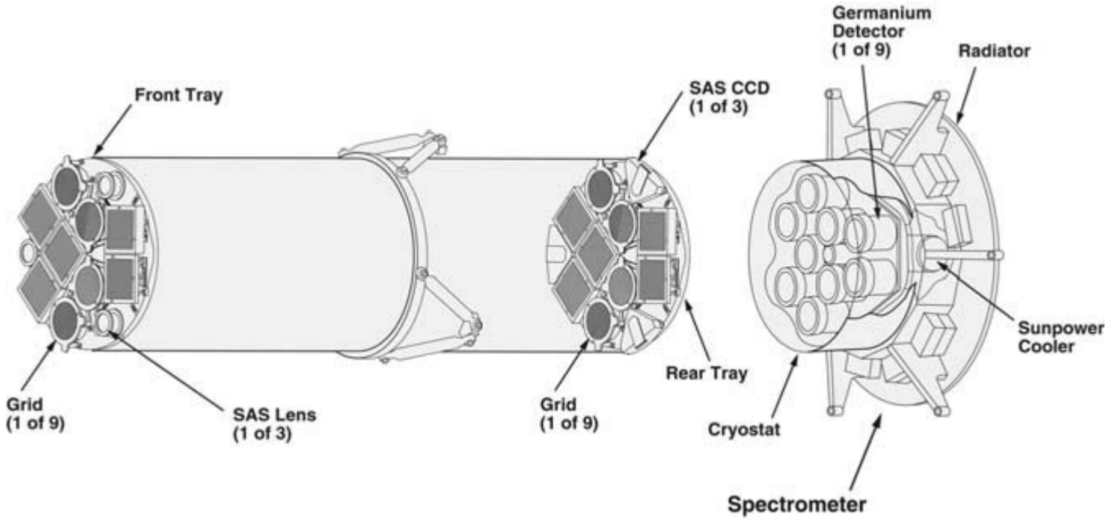

Figure 3.1: Schematic of RHESSIs imaging instrument. Taken from Hurford et al. (2002).

do this, RHESSI measures counts of X-ray photons using nine cooled germanium detectors. The detectors are each located behind a a pair X-ray opaque grids as illustrated by the schematic shown in Figure 3.2.

The grid pairs are labelled 1 through 9 with logarithmically increasing spacing between the slats. The spacing between the slats for each set of grids results in different image resolutions of 2.26, 3.92, 6.78, 11.8, 20.4, 35.5, 61.1, 105.8, and 183.2 arcseconds. RHESSI rotates around its axis every 4 s as its pointing at the Sun. This causes the incident photons to be preriodically blocked resulting in a modulation of the detected signal. The pattern of this modulation encodes spatial information, which when combined with knowledge of the grid geometries and and the spacecraft spin period, allows for the reconstruction of images. This modulation pattern is shown in Figure 3.3 where the variation in amplitude, phase, and frequency can be observed for off-axis sources of various geometries.

By stacking the modulated signal in bins per fraction of the spacecraft rotation, X-ray visibilities are generated that consist of two-dimensional Fourier components of the X-ray source given by

$$V(u,v;\epsilon) = \int_x \int_y I(x,y;\epsilon) e^{2\pi i(ux+vy)} dxdy \tag{3.1}$$

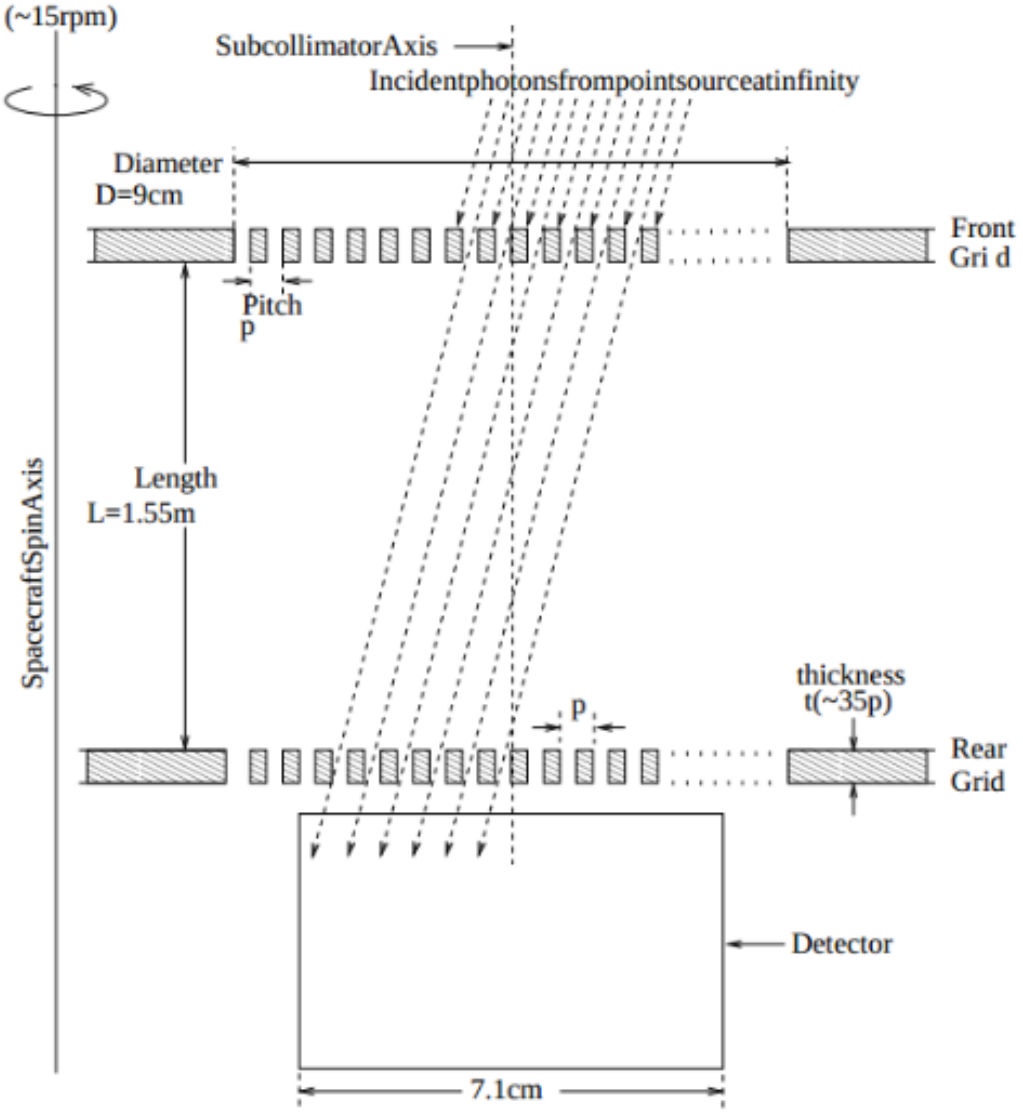

Figure 3.2: Schematic of RHESSIs imaging apparatus. Incoming X-rays first encounter both sets of grids. The amount of photons which reach the detector, having not been blocked by the opaque slats, is related to their angle of incidence. Due to the rotation of the spacecraft every 4 seconds, this gives rise to a modulation of the detected signal which encodes the spatial information on the incident X–rays (Hurford et al., 2002).

where (u, v) are the coordinates in Fourier space which depend on the grid pitch and current angle of the grid slats. Taking the inverse Fourier transform of this equation results in an image, I, in real space for a given energy ϵ. This type of image reconstruction has historically been used in radio astronomy but is also applicable in the X-ray regime.

Using a combination of detectors for selected time intervals and energy ranges allows for the optimisation and tailoring of these image reconstructions. Several algorithms

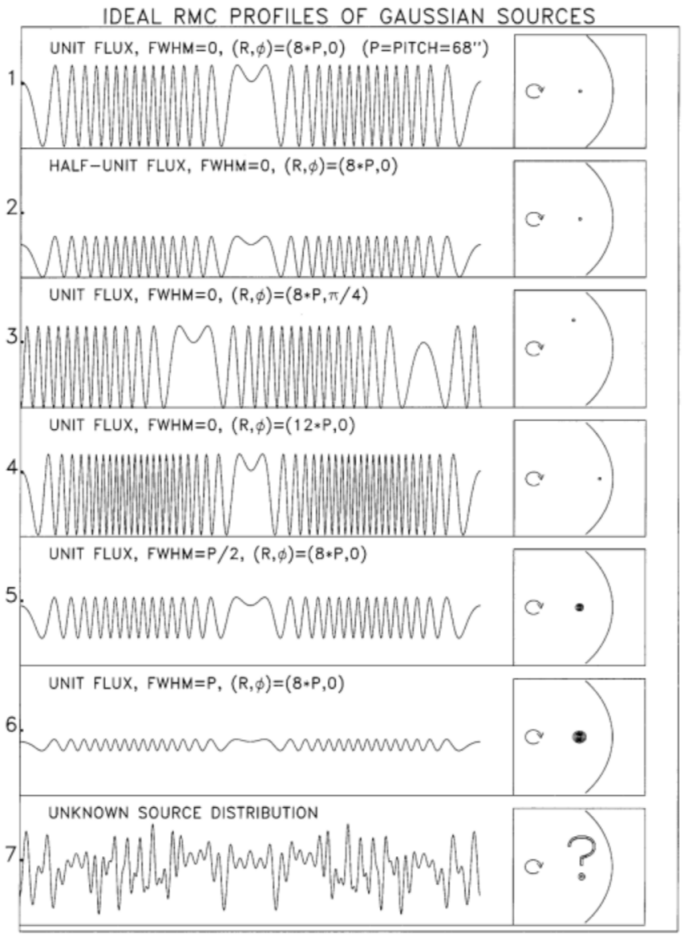

Figure 3.3: RHESSI modulation profiles for various source configurations (Hurford et al., 2002).

are typically employed to produce from measured RHESSI visibilities. The method described above in which the inverse Fourier transform of Equation 3.1 is taken is the simplest approach. This technique is known as *back projection*. This method, although efficient, does not produce images of the highest quality.

More sophisticated algorithms such as CLEAN can be used to improve the image quality. CLEAN is the most commonly employed algorithm to remove sidelobes from a 'dirty map'. It works by locating the pixel containing the peak flux of the map. A fraction of that flux value, usually 10%, is then taken in order to produce a point source of flux. The point source is then convolved with a Gaussian and placed onto a new a new *CLEANed* map. This process is iterated a set number of times, or until the peak flux in the image is negative. The resulting CLEANed map is made up of the positions and amplitudes of the CLEAN components. Another standard algorithm

commonly, known as *Pixon*, takes into account the spatial scale required by the data at each point in the image. This method is employed in Chapter 5 to produce images of X-ray sources associated with QPPs. PIXON is thought to provide the most accurate image photometry of the standard alogirhtm, although it is slower to run than CLEAN (Hurford et al., 2002).

3.1.2 RHESSI Spectroscopy

The RHESSI spectrometer consists of 9 Germanium detectors. An incident X-ray or γ-ray photon produces an electron-hole pair upon reaching the dectectors. This gives rise to a small current that is registered as a time-tagged count. The observed count spectrum (C) relates to the incident photon spectrum (I) via

$$C = B + DRM + I \tag{3.2}$$

here B is the background count rate, and DRM is the detector response matrix. Instrumental noise and non-solar emissions are contributors to the background count rate. The detector response matrix accounts for effects such as Compton scattering, radiation damage to the detectors and, noise in the electronics. Once these effects are accounted for, the RHESSI count spectra (C) can be used for time-series analysis in different energy bands as well as spectroscopy using Objective Spectral Executive (OSPEX) (Schwartz et al., 2002). As RHESSI is in a low Earth orbit, it experiences regular night-time intervals. During these times data are not available. For a period of the flare analysed in Chapter 5, this occurred, restricting our capabilities to carry out imaging analysis for the entire event.

3.2 The Spectrometer Telescope for Imaging X-rays (STIX)

Solar Orbiter is a Sun-observing satellite that was launched on 10 February 2020. The Spectrometer Telescope for Imaging X-rays (STIX), one of ten instruments on-board Solar Orbiter, is a hard X-ray imaging spectrometer. Similarly to RHESSI, STIX observes the hottest flare plasma, providing data on the location and energy content of accelerated non-thermal electrons. Due to the decommissioning of RHESSI, STIX now plays a key role in maintaining our ability to investigate high-energy release processes in solar flares. STIX has 32 Cadmium Telluride (CdTe) X-ray detectors capable of observing energy ranges in the 4 to 150 keV range at 1 keV resolution (Krucker et al., 2020). It employs indirect Fourier imaging techniques related to the method through which RHESSI generates images, as outlined in Section 3.1.1. STIX has a time resolution of 0.1-1 s and its finest angular resolution is 7 arcsec.

The hardware of STIX consists of three main sub-systems. These include:

- A pair of X-ray transparent entrance windows that are independently mounted in the heat shield of Solar Orbiter.
- An imager with two widely separated grids.
- A detector module mounted behind the imager containing electronics (DEM module), the cadmium telluride (CdTe) detectors, and a movable X-ray attenuator.

Figure 3.4 shows a schematic (top) and photograph (bottom) of these systems (Krucker et al., 2020).

The windows are key to the instruments thermal control system which act to limit incident optical and infra red flux. They also serve to preferentially absorb excessive amounts of low energy X-rays to prevent effects such as pulse pile-up. As mentioned, STIX uses Fourier-transform based imaging. One benefit of this technique is that it allows for limited-telemetry systems. The X-ray opaque grids are separated by

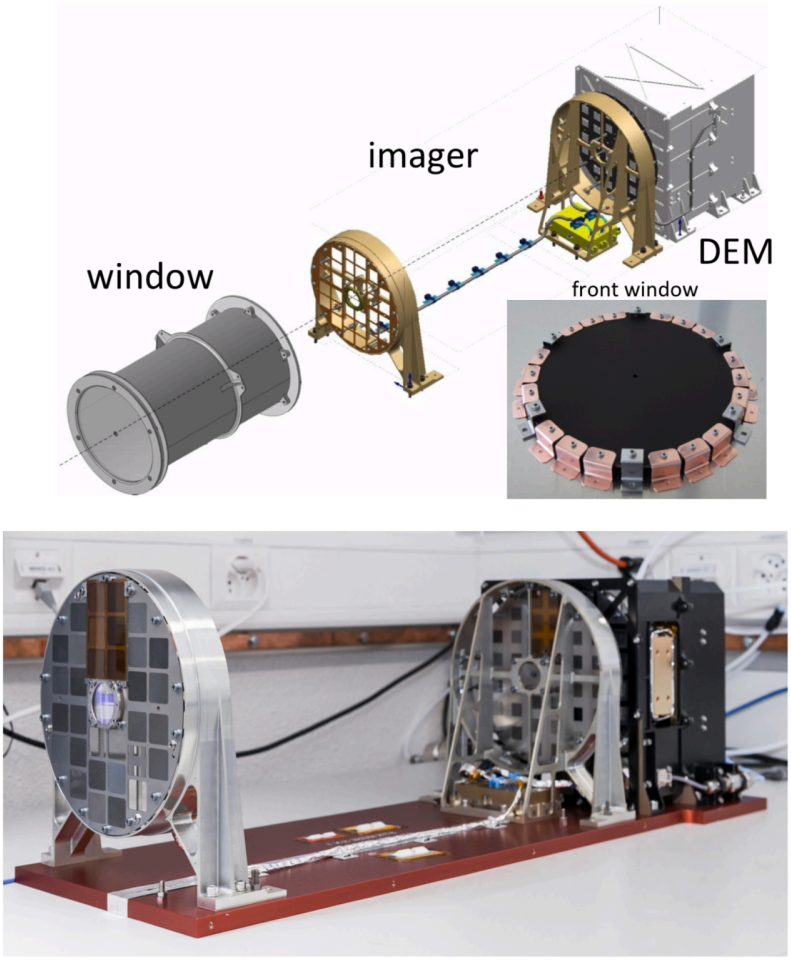

Figure 3.4: Schematic and photographic views of the STIX instrument (Krucker et al., 2020).

55cm and are divided into 32 subareas, each with corresponding detectors behind the rear set of grids. The front and rear grids have slits that differ slightly in pitch and orientation. As X-rays are transmitted to the detectors, this results in a large-scale Moire pattern, for which the amplitude and phase is sensitive to the angular distribution of the incident X-ray flux. Similarly to the RHESSI imaging concept, this type of system measures a set of visibilities that can be processed using algorithms to generate images. STIX registers counts by detecting photons via the Cadmium Telluride semiconductor detectors.

In Chapter 6, STIX time-series data of various energies is used in conjunction with data from various instruments to analyse X-ray and radio diagnostics of accelerated electrons. Additionally, analysis and visualisation software that was developed for

STIXpy, a python based package for STIX data analysis, is presented. The capability of STIX to produce high cadence X-ray images will form part of my future work, as outlined in Chapter 7. Further details of the STIX instruments, its capabilities and imaging concept can be found at Krucker et al. (2020).

3.3 FERMI Gamma Ray Burst (GBM) monitor

The Fermi Gamma-Ray Burst Monitor (GBM) is an instrument on board the Fermi Gamma-Ray Space Telescope (Meegan et al., 2009). This instrument observes the entire sky over an energy range of 8 keV to 40 MeV, with the goal of investigating gamma-ray bursts. FERMI GBM unitises two sets of detectors that are sensitive to different energy bands. 12 thallium-activated sodium iodide scintillation detectors are capable of measuring 8 keV to 1 MeV photons, while two bismuth germanate detectors are sensitive to energies of 150 keV to 40 MeV.

Despite solar observations not being the intentional use for FERMI GBM, it provides quality, complimentary data that overlaps with the RHESSI and STIX energy ranges. The time cadence if the instrument is 1 s in normal mode but it can achieve a time resolution of up to 0.28 s in burst mode. In the QPP investigation presented in Chapter 5, light-curves observed by FERMI GBM are used to study the oscillatory X-ray signals missed by RHESSI, which was in spacecraft night. The high time cadence of FERMI GBM makes it ideal for lightcurve investigations which can be combined with the imaging capabilities of both RHESSI and STIX.

3.4 Geostationary Operational Environmental Satellite (GOES)

The Geostationary Operational Environmental Satellites (GOES) are operated by the United States' National Oceanic and Atmospheric Administration (NOAA). Initially, GOES-1 was launched in 1975. The latest satellite, GOES-17, was launched on 1

March 2018 and declared operational in February 2019. GOES has two X-ray Sensors (XRS) that are particularly useful for solar physics applications. These sensors provide capability for spatially integrated solar X-ray flux measurements in two channels: 0.5-4.0 Å and 1.0-8.0 Å. The current GOES XRS system has a 1 s cadence. The peak flux of 1.0-8.0 Å GOES/XRS channel is used to classify the magnitude and duration of solar flares.

Dual ion chamber detectors with beryllium windows are used by the XRS. Chamber A, filled with xenon gas, is used to measure the 0.5-4 Å X-rays and has a window thickness of 20mm. Chamber B is used to measure the 1-8 Å X-rays. This contains Argon and has a 2mm thick window. In each case, the raw detections are currents induced in the chambers due to interacting incident photons. As well as providing high time cadence SXR data from flares, the derivative of GOES/XRS data can supply information about the non-thermal, higher energy X-rays via the Neupert effect (Neupert, 1968a). This effect is exploited in Chapters 6 and 7 while investigating non-thermal X-ray pulsations and their association with type III radio bursts.

3.5 The Solar Dynamics Observatory (SDO)

The Solar Dynamics Observatory (SDO) is NASA–designed satellite mission. It was launched on 11 February 2010 with the science goal of studying small scale structure in the solar atmosphere with high time and spatial resolution capabilities. The mission also aims to further our understanding of the Sun–Earth connection (Pesnell et al., 2012). Three instruments are operate on board SDO which are named the *Atmospheric Imaging Assembly* (Lemen et al., 2012a), the *Helioseismic and Magnetic Imager* (Scherrer et al., 2012), and the *Extreme Ultraviolet Variability Experiment* (Woods et al., 2015). Data from the Atmospheric Imaging Assembly (AIA) was used in this thesis to identify QPPs in the EUV regime, and to locate the region from the flare site from which the QPPs originated.

3.5.1 Atmospheric Imaging Assembly (AIA)

Analysing EUV images of the solar atmosphere provides insight into energy release, energy transport, and the magnetic configurations of active regions. AIA provides full-disk images of the solar atmosphere in EUV pass-bands including 94, 131, 171, 193, 211, 304, 335, 1600, 1700 and 4500 Å. The coronal plasma being imaged at EUV wavelengths is frozen-in to the magnetic field. The plasma therefore traces out the magnetic field lines, revealing the complex loop structures as shown in Figure 1.10. The high time and and spatial resolution of AIA, 0.6" and 12 s respectively, make it an ideal instrument for studying short timescale phenomena associated with energy release and heating. The imaging apparatus of AIA is made up of four 20 cm Cassegrain telescopes, each with different filters made of Zirconium, appropriate for imaging the aforementioned passbands. Each telescope records images onto a 4096×4096 CCD. The different passbands AIA observes detect specific emission lines that probe specific temperatures. Therefore, the different channels of AIA provide a tool for observing different layers of the solar atmosphere. Table 3.1 summarises the details of the AIA channels, showing the wavelengths, the primary source of emission, the targeted region of the solar atmosphere, and the peak characteristic temperature. Figure 3.5 shows the temperature response function of the 6 coronal channels of AIA. One can note the

Channel	Primary Ions	Region of Atmosphere	log T (K)
4500 Å	continuum	photosphere	3.7
1700 Å	continuum	temperature minimum, photosphere	3.7
304 Å	He II	chromosphere, transition region	4.7
1600 Å	CIV+ cont	transition region, upper photosphere	5.0
171 Å	Fe IX	quiet corona, upper transition region	5.8
193 Å	Fe XII, XXIV	corona and hot flare plasma	6.2, 7.3
211 Å	Fe XIV	active–region corona	6.3
335 Å	Fe XVI	active–region corona	6.4
94 Å	Fe XVIII	flaring corona	6.8
131 Å	Fe VIII, XXI	transition region, flaring corona	5.6, 7.0

Table 3.1: AIA channel details taken from Lemen et al. (2012a). Shown are the wavelengths of each channel, the primary source of emission, the targeted region of the solar atmosphere, and the peak characteristic temperature.

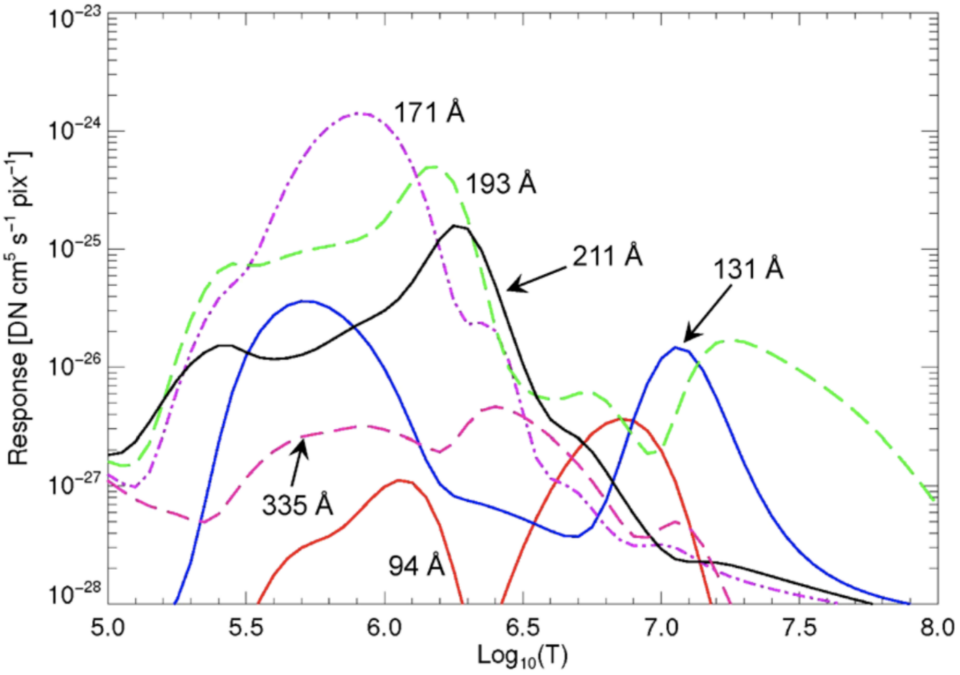

Figure 3.5: AIA temperature response functions for the coronal channels (Lemen et al., 2012a).

double peaks for some channels and the large variance in the width of the temperature response between some channels. QPPs investigated in this thesis were detected using the 171 Å and 1600 Å passbands, as outlined in Chapter 5.

3.6 Ukrainian T-shaped Radio Telescope (UTR-2)

The Ukrainian T-shaped Radio telescope, second modification (UTR-2) is one of the world's largest radio telescopes at decameter wavelengths. It was completed in 1972 and is operated by the Institute of Radio Astronomy of the Ukrainian Academy of Sciences. The telescope consists of 2040 dipole elements. Each of the dipoles is aligned along the east-west axis. The individual elements are broadband cage dipoles that are 8 m long and 1.8 m in diameter. The dipoles are in the form of two cylinders. They are composed of galvanized steel wire and are mounted 3.5 m above the ground.

The elements are arranged in two arms, forming a T-shape. The larger north–south arm consists of 1440 elements and the east–west arm consists of 600 elements. The dipoles are spaced 7.5 and 9 m in the north–south and east–west directions, respectively.

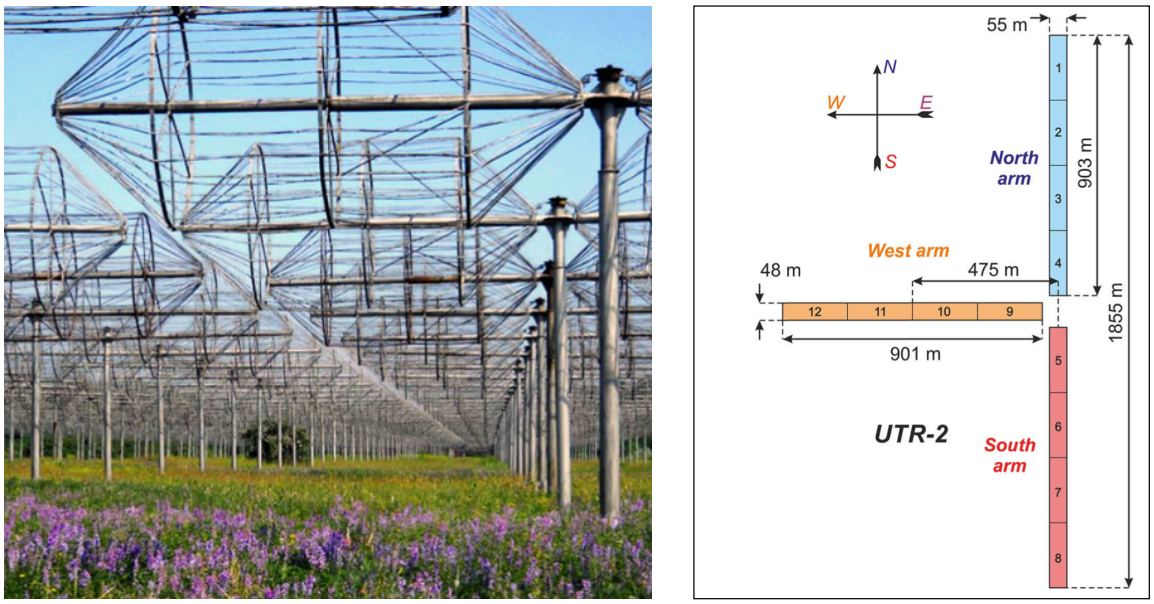

Figure 3.6: Photograph (left) and geometrical configuration (right) of UTR-2. Taken from Konovalenko et al. (2016).

This configuration amounts to a large effective area of $\sim 1.4 \times 10^5\ m^2$. UTR-2 observes frequencies of ∼8-32 MHz and has a sensitivity of ∼10 mJy. This frequency range is lower than that of LOFAR providing coverage for lower energies. Analysing dynamic spectra obtained by UTR-2 is a primary focus of Chapter 4 in which combined spectral observations of S-bursts using LOFAR and UTR-2 are presented and interpreted.

UTR-2 has a frequency resolution of 4 kHz. This interferometer has a potential time resolution of 0.5 ms, however, for the UTR-2 observations included in this thesis, the integration time was set to 100 ms. The telescope is a part of the URAN (Ukrainian Radio Interferometer of NASU) network, which includes four smaller low-frequency telescopes. Although UTR-2 has imaging capabilities, for the observations used in this thesis, only spectral information was available. The left side of Figure 3.6 shows a photograph of the elements that make up UTR-2 while the right side shows a schematic of the geometrical configuration of the telescope (Konovalenko et al., 2016).

3.7 The LOw Frequency ARay (LOFAR)

The LOw Frequency ARray (LOFAR) is a large radio telescope network that was constructed by the Netherlands Institute for Radio Astronomy (ASTRON) in 2012. It

Figure 3.7: LOFAR Superterp and core stations. The LOFAR core is located in Exloo, Netherlands. Taken from Haarlem et al. (2013).

has polarisation and multi-beaming capabilities, as well as excellent sensitivity due to its large number of antennas. At the time of the observations presented in Chapter 4 (July 2013), the network consisted of ∼7000 antennas. Today, the network has grown and contains ∼20,000 antennas. The low band antennas (LBAs) of LOFAR operate at frequencies of 10-90 MHz, while its high band antennas (HBAs) operate at 110-250 MHz (Haarlem et al., 2013). These antennas are distributed over 24 core stations and 14 remote stations in the Netherlands, and 14 international stations across Europe.

The 24 LOFAR core stations were used for the observations presented in this Chapter 4. One of the beam formed modes of LOFAR in the LBA frequency range was used to produce high time (∼10 ms) and frequency (12.5 kHz) resolution dynamic spectra in order to study the spectral characteristics of the S-bursts detected on 9 July 2013 (Haarlem et al., 2013; Stappers et al., 2011). Figure 3.7 shows the LOFAR Superterp and core stations where the LBAs and HBAs can be distinguished (Haarlem et al., 2013).

The LBAs are dipoles consisting of two copper wires. The wires are configured in

an inverted V-shape, with angle of 90 degrees, allowing for polarisation measurements. The dipole arms are 1.38 m in length. This results in a resonance frequency of 58 MHz. The wires connect to a low noise amplifier on a moulded top which is propped up on a pipe 1.7 m high. Steel concrete reinforcement rods on the ground act as a reflector of radio waves. Two coaxial cables output each polarisation of the LBAs and supply power to the low noise amplifier. The HBAs have a different design to the LBAs. 16 antenna elements in a 4x4 pattern make up one HBAs. Each cluster contains a built-in amplifier, an analog beam former, and are covered by protective foil. The antennas are hidden beneath this protective covering, appearing as black tiles as shown Figure 3.7. LOFAR can produce images via interferometric imaging mode and beam-formed imaging. LOFAR imaging did not form part of the work contained in this thesis. High resolution dynamic spectra from the Irish station, I-LOFAR, is used in Chapter 6 in combination with X-ray observations from STIX.

3.8 WIND/WAVES

The WIND satellite is a NASA science spacecraft that was launched on 1 November 1994 (Bougeret et al., 2008). The aim of the mission is to investigate radio waves and plasma occurring in the solar wind and the Earth's magnetosphere. WIND consists of 8 instruments. one of which is the Radio and Plasma Wave Investigation known as WAVES. The detectors of WIND/WAVES are three orthogonal electric field dipole antennas. WIND/WAVES has a total of five receivers. In this thesis, radio receiver band 1 (RAD1) and radio receiver band 2 (RAD2) are used to investigate low frequency radio bursts. RAD1 has a frequency band of 20–1040 kHz, while RAD2 has a frequency band of 1.075–13.825 MHz. The data from WIND/WAVES used in Chapter 6 had a time cadence of 16.188 s and each radio receiver was split into 256 frequency bands.

4

Properties and Magnetic Origins of Solar S-bursts

As introduced in Section 1.7, S-bursts are short duration, low frequency bursts that appear as narrow tracks on a dynamic spectrum. Here, observations from the Ukrainian T-shaped Radio telescope, (UTR-2), and the LOw Frequency ARray (LOFAR) are reported which give us new insight into their nature. On 9 July 2013, 203 S-bursts were observed with UTR-2 and over 3000 S bursts were observed with LOFAR (Morosan et al., 2015). The UTR-2 observations were made by the National Academy of Sciences of Ukraine. Their solar team processed the data and provided us with the spectra. The LOFAR observations were provided by Dr Diana Morosan who previously published the data in a separate study (Morosan et al., 2015). We then collected and analysed the S-burst data from the provided dynamic spectra. The observations were made between 05:34 and 14.30 UT. During this time, there was solar activity in the form of three C-class flares. Using UTR-2, 100 Type III and IIIb radio bursts were also observed during this period in order to compare their fluxes with that of the accompanying S-bursts. For each of the 203 events observed with UTR-2, the following properties of the bursts were recorded: start time, end time, duration, flux, start frequency, end frequency, bandwidth, drift rate, FWHM duration, and instantaneous bandwidth, as outlined in Figure 4.1. Figure 4.1a shows how the start frequency, end frequency, bandwidth, start time, end time, duration, and drift rate were recorded for a typical, negatively drifting burst.

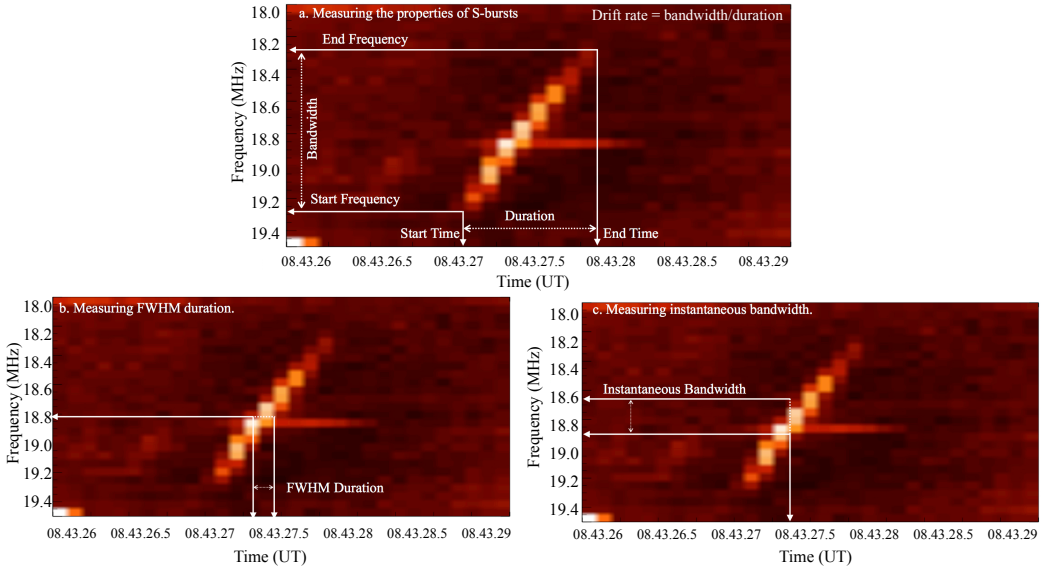

Figure 4.1: Dynamic spectrum containing a typical, negatively drifting S-burst. Also shown is the method through which the various measured properties were recorded. Panel (a) shows the start/end time, start/end frequency, duration, bandwidth, and drift rate of the burst. Panel (b) shows the bursts FWHM duration. Panel (c) shows the bandwidth at a fixed central time (instantaneous bandwidth), sometimes referred to as the frequency width of the burst. The apparent stair-like structure of the S-burst in this dynamic spectrum is an integration time effect and not an actual property of the burst.

Assuming the bursts are produced via plasma emission, the total bandwidth provides information about how far through the solar atmosphere the source travelled while it was emitting. Figure 4.1b shows how the FWHM durations, which is duration at a fixed central frequency, of the bursts were recorded while Figure 4.1c shows how the instantaneous bandwidths, which is bandwidth at a fixed central time, Δf, were recorded. The instantaneous bandwidth provides information about the size of the source producing the emission, again assuming plasma emission (Kontar et al., 2017). The UTR-2 data were fully calibrated enabling flux measurements. The lighter colours indicate higher flux values as shown in the colour table in Figure 1.17. The low frequency band observations (∼18-31 MHz) made with UTR-2 were compared against the higher and broader frequency band observations (∼20-80 MHz) made with LOFAR (Morosan et al., 2015). The same properties that were measured with UTR-2 were measured with LOFAR. However, no flux measurements were conducted using LOFAR as the data were not flux calibrated. These measured properties were then analysed and compared against the assumptions made within the Melnik et al. (2010)

and Zaitsev & Zlotnik (1986) models.

Assuming S-bursts are emitted at frequencies close to the local plasma frequency, it is possible to estimate their source heights. Using the active region coronal electron density models of Newkirk Jr. (1961), Newkirk Jr. (1967), Baumbach-Allen (Aschwanden, 2005), and Zucca et al. (2014), the observed S-bursts (frequencies of ∼18-80 MHz) are expected to have source heights of ∼1.3-2 $R_{\odot}$. The active region magnetic field model of McLean et al. (1978) and a potential field source surface (PFSS) model, which provides an approximation of the coronal magnetic field up to 2.5 $R_{\odot}$ based on the observed photospheric field (Schrijver & De Rosa, 2003), can then be used to estimate the strength of the coronal magnetic field at these heights. In this analysis, we calculate the strength of the coronal magnetic field that the model of Melnik et al. (2010) predicts for each burst. We then estimate the source height for each burst and compare the strength of the magnetic field at each height, according to the active region magnetic field model of McLean et al. (1978) and the PFSS model, with what the Melnik et al. (2010) model implies according to our data.

4.1 Results

4.1.1 S-burst properties

All of the radio bursts for which data was collected in this work were identified manually by visually inspecting dynamic spectra. A point and click method was then employed to measure the spectral properties of the bursts. Due to the wide range of intensity profiles, variation in spectral shapes, radio frequency interference and other factors within the data, it was not possible to create an effective algorithm to automate this process. However, machine learning techniques are currently under development within the solar physics community to solve this problem with the aim of reducing any errors that may be introduced by the conventional manual identification/point and click method presented here. The LOFAR data points were also identified manually (Morosan et al., 2015). The method through which the measured spectral properties

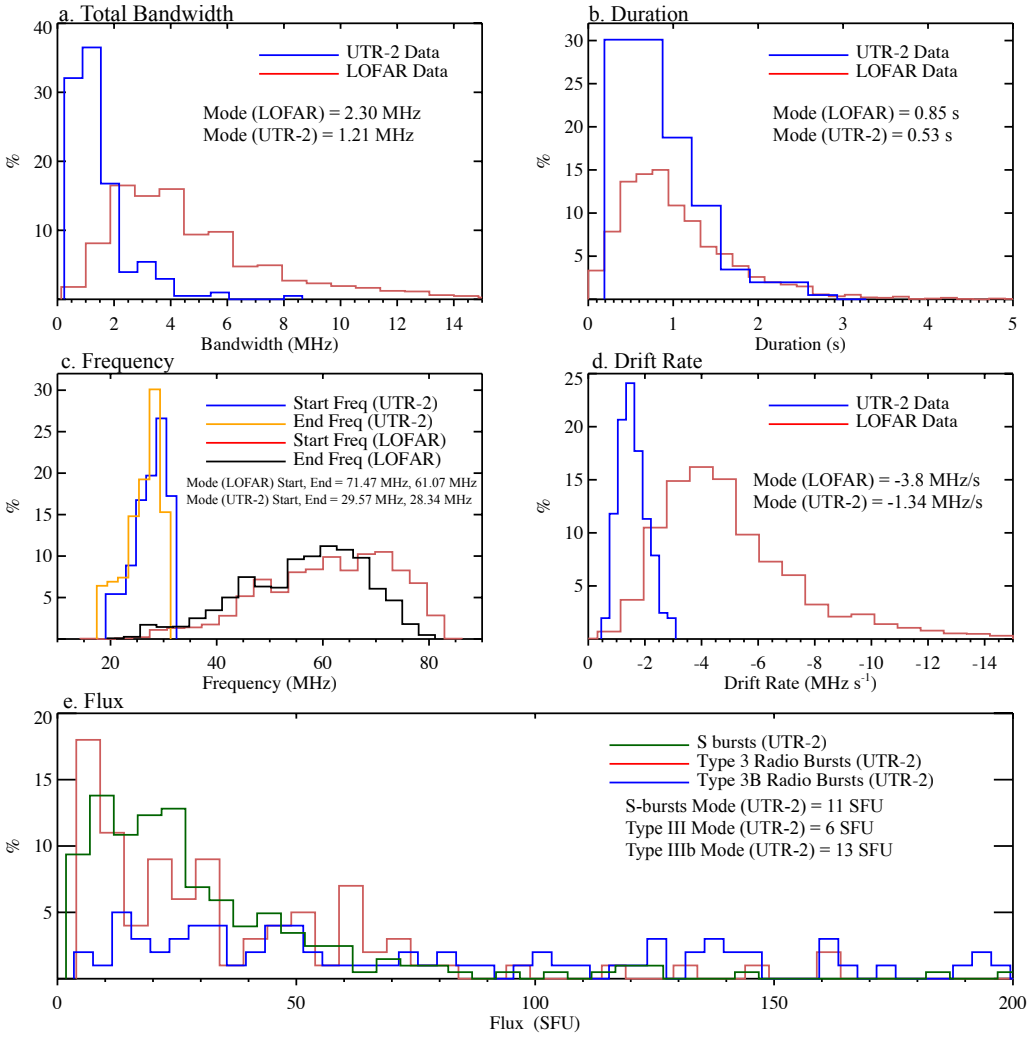

Figure 4.2: S-burst property distributions from UTR-2 and LOFAR (Morosan et al., 2015). Panel (a) shows bandwidth; panel (b): duration; panel (c): start and end frequencies; panel (d): drift rate; panel (e): flux (only contains UTR-2 data; also includes data recorded for Type III and Type IIIb bursts). The mode values are given for each case.

of the bursts was recorded is shown in Figure 4.1. In Figure 4.2, the distributions of bandwidths, durations, start frequencies, end frequencies, and drift rates from both UTR-2 and LOFAR are shown. The flux distributions of S-bursts, Type III bursts, and Type IIIb bursts obtained from UTR-2 are also shown.

The S-bursts had an average total frequency bandwidth of 1.21 ± 0.32 MHz and 2.30 ± 0.43 MHz using the UTR-2 and LOFAR data, respectively. These results indicate that higher frequency S-bursts generally give rise to higher total bandwidths. This tells us that S-bursts sources with higher energies emit and travel over longer distances. Few bursts were observed to have total bandwidths greater than 10 MHz. After discard-

ing unreliable data as a consequence of time resolution limitations, the instantaneous bandwidths of the S-bursts were found to range from 0.14-2.04 MHz. These results generally agree with the previous studies of McConnell (1982), Melnik et al. (2010), and Morosan et al. (2015). The mode duration was found to be 0.53 ± 0.34 s and 0.85 ± 0.09 using the UTR-2 and LOFAR data, respectively. As shown in Figure 4.2b, these distributions agree well within error despite the different frequency bands that UTR-2 and LOFAR can observe. This indicates that the duration of S-bursts is independent of the frequency of S-bursts. These values agree well with previous reports from McConnell (1982), Melnik et al. (2010), and Morosan et al. (2015), most of whom observed S-bursts to have short durations of < 1 s. The FWHM durations of the S-bursts were found to range from 0.1-0.6 s using the UTR-2 data and 0.02-0.4 s using the LOFAR data. These values also agree well. The integration time of our UTR-2 data (100 ms) most likely prevented detection of the lower values that were detected by LOFAR. The observed S-bursts had frequencies that ranged from 18.7-31.4 MHz (UTR-2) and 20.61-80.94 MHz (LOFAR). Figure 4.2c shows the distributions of start and end frequencies for each burst. The majority of S-bursts from both data sets had greater start frequencies than end frequencies illustrating how S-bursts generally start at higher frequencies and drift towards lower frequencies as they evolve. This tells us that S-burst sources generally travel from higher density regions lower in the solar atmosphere towards regions of lower density higher up.

S-burst fluxes are shown in Figure 4.2e in which they are compared to Type III and Type IIIb fluxes. Based on Figure 4.2e, Type III bursts and S-bursts have similar flux distributions with S-bursts generally having higher fluxes. The distribution of flux values for Type IIIb radio bursts is far broader than the other two types and there are many more examples of bursts with flux values > 100 SFU. For these particular observations, the majority of Type IIIb radio bursts have greater flux values than S-bursts or Type III bursts. More generally, Type III bursts can reach highs of 10^6 SFU, Type IIIb bursts are limited to thousands of SFU, and S bursts are rarely greater than 100 SFU (Melnik et al., 2010).

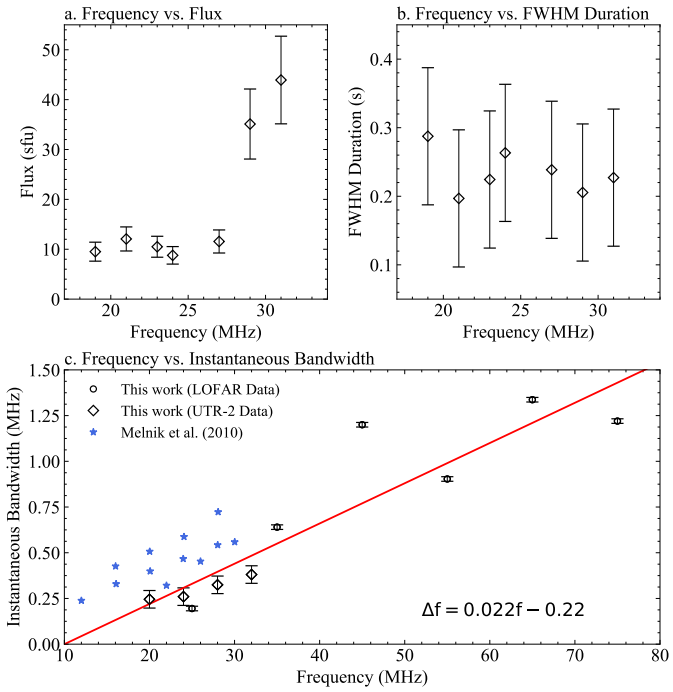

Figure 4.3: Plots of frequency vs. flux and frequency vs. FWHM duration are shown in panels (a) and (b), respectively. No clear dependence was observed. In panel(c), a plot of frequency vs. instantaneous bandwidth is shown. Overplotted are the results of Melnik et al. (2010). We observe a linear dependence between frequency and instantaneous bandwidth, confirming the same result observed by Melnik et al. (2010) over a broader frequency band.

Scatter plots of frequency versus flux and frequency versus FWHM duration are shown in Figure 4.3a and Figure 4.3b, respectively. Figure 4.3c shows a plot of frequency versus instantaneous bandwidth. The included parameters were measured separately in several sub-bands. The sub-bands used in panels a and b were 18-20 MHz, 20-22 MHz, 22-24 MHz, 24-26 MHz, 26-28 MHz, 28-30 MHz and 30-32 MHz. In Figure 4.3c, the sub-bands used for the UTR-2 data are 18-22 MHz, 22-26 MHz, 26-30 MHz, and 30-34 MHz. For the LOFAR data, wider bands of 10-20 MHz, 20-30 MHz, 30-40 MHz, 40-50 MHz, 50-60 MHz, 60-70 MHz, and 70-80 MHz are used. The obtained values were linked to the central frequency of the corresponding sub-band. Overplotted in Figure 4.3c are the results of Melnik et al. (2010). No clear dependence is observed between frequency and flux or frequency and FWHM duration. Using the UTR-2 and LOFAR data collected on 9 July 2013, we observe a linear dependence between frequency and instantaneous bandwidth. The line of best fit is shown in red, which was found to have a slope of 0.022 and an intercept of -0.22 indicating a relation of the

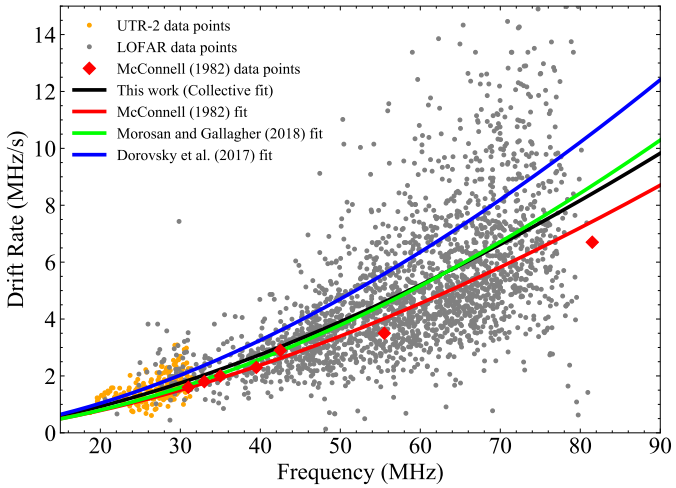

Figure 4.4: Dependence of drift rate on frequency fitted according to power laws using coefficients a and b. The fits derived from the observations of Morosan & Gallagher (2018), Dorovskyy et al. (2017), and McConnell (1982) are plotted in green, blue, and red, respectively. The black fit takes into account the orange (UTR-2 data), grey (LOFAR data from Morosan & Gallagher (2018)), and red (data from McConnell (1982)) points to provide, for the first time, a collective analysis of this dependence using multiple instruments.

form

$$\Delta f = 0.022 f - 0.22. \tag{4.1}$$

The physical interpretation of this is that the larger source sizes tend to have large central frequencies. For this analysis, it was again ensured that because of time resolution limitations unreliable data were not included. This analysis confirms the same result observed by Melnik et al. (2010) over a broader frequency band using multiple instruments.

4.1.2 Drift rate

An important property of radio bursts is how their frequency changes with time, known as their drift rate, df/dt. The relation between the drift rate and frequency of a radio burst can reveal information about the emission mechanism responsible for that burst. For example, if the bursts are generated at the local plasma frequency, we can estimate the velocities of the associated electron beams via this relation. The majority of S-bursts in this study had negative drift rates. However, there were some rare

cases of positively drifting S-bursts, which agrees with previous authors (Melnik et al., 2010; Morosan et al., 2015). A plot of average frequency versus drift rate is shown in Figure 4.4. The dependence between drift rate and frequency may be represented by the following power law:

$$\frac{df}{dt} = -af^b, \tag{4.2}$$

where a and b are fitting parameters. The values of a and b derived from collective data obtained from UTR-2, LOFAR, and the Llanherne Radio Telescope (red points on plot) are given in Table 4.1 providing a new analysis of this dependence from a multi-instrumental perspective. This was done by fitting a power law function to the collected data using a non-linear least squares method. The values found from our collected UTR-2 data and those found in the previous works of McConnell (1982), Dorovskyy et al. (2017), and Morosan & Gallagher (2018) are also given. The values of a and b in Table 1 all agree well, which is reflected by the similarity of the fits shown in Figure 4.4. The slight discrepancy between the fits could be accounted for because of the different frequency ranges in which each set of observations were taken and because the measurements were taken on different dates. The date of the observations can have influence as the drift rate depends on the plasma properties, which may naturally vary from day to day. The distribution of drift rates for each S-burst is given in Figure 4.2d, where it is shown that the majority of the bursts drift at a rate of -1.34 ± 0.15 MHz s^{-1} and -3.80 ± 0.41 MHz s^{-1} using the UTR-2 and LOFAR data, respectively. This difference is to be expected due to the different frequency ranges of LOFAR and UTR-2.

Table 4.1: Comparison of power law fit parameters.

Author(s)	a	b
McConnell (1982)	0.0065 ± 0.0006	1.60 ± 0.06
Dorovskyy et al. (2017)	0.0074	1.65
Morosan & Gallagher (2018)	0.0049	1.7
This Work (collective data)	0.0084 ± 0.006	1.57 ± 0.17

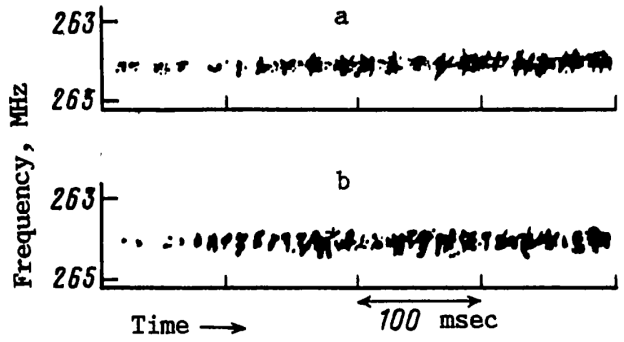

Figure 4.5: Sketch of bursts modelled by Zaitsev & Zlotnik (1986)

4.2 Discussion

The two models that we focus on in this discussion are the plasma emission models put forward by Melnik et al. (2010) and Zaitsev & Zlotnik (1986). Each of these models assumes that the instantaneous bandwidth of S-bursts linearly increases with frequency. Melnik et al. (2010) showed this dependence over a narrow frequency band (10-30 MHz). Using UTR-2 and LOFAR data, our results can confirm this relation over a wide frequency band for the first time.

The plasma emission model of Zaitsev & Zlotnik (1986) proposes that electron beams, with velocities that are ten to twenty times the thermal velocity of the local electrons, move through a slightly anisotropic plasma within a quasihomogeneous magnetic field. These beams excite plasma waves which are then scattered by thermal ions to produce electromagnetic radiation at the local plasma frequency, f_p. As outlined in the introduction, Melnik et al. (2010) pointed out that the model of Zaitsev & Zlotnik (1986) produces incorrect coronal inhomogeneity sizes and magnetic field strengths at heights corresponding to the local plasma frequency and a flatter drift rate dependence on frequency than follows from observations. Additionally, we note that the bursts modelled by Zaitsev & Zlotnik (1986) represent very narrow-band bursts (< 1 MHz) that have central frequencies of $\sim$254 MHz (as shown in Figure 4.5) and total bandwidths that are approximately equal to their instantaneous bandwidths. The model assumes a static source that attributes the frequency drift rate to the electromagnetic

wave group delay. However, the S-bursts presented in this work display long lasting saber-shaped features which may extend in frequency by up to 12 MHz (Melnik et al., 2010). Additionally, their total bandwidths are much greater than their instantaneous bandwidths, indicating a dynamic source. Therefore, the model of Zaitsev & Zlotnik (1986) is unable to account for the characteristics of S-bursts that are commonly observed at decametre wavelengths. It is possible that the bursts modelled by Zaitsev & Zlotnik (1986) belong to a separate class of radio bursts that are produced by a different mechanism to the S-bursts we observe. Our observations of the spectral properties of S-bursts provide support for the core assumptions contained within the model of Melnik et al. (2010). For example, the long-lasting sabre shaped structure of S-bursts and their appearance against the background of other types of radio activity were consistent throughout the data. A linear relation between frequency and instantaneous bandwidth was also found. Additionally, evidence was observed that S-bursts are produced by moving particles, as opposed to the stationary sources proposed by Zaitsev & Zlotnik (1986).

The model of Melnik et al. (2010) suggests that S-burst sources are beams of electrons or protons which move at velocities that are five to nine times the thermal velocity of the local electrons. They propose that the merging of the RH waves with Langmuir waves gives rise to electromagnetic waves. Provided there is a sufficiently large angle between the k-vectors of these waves, the resulting emission has a frequency equal to the upper hybrid resonance frequency, ω_{UH}, plus half the electron cyclotron frequency, $\Omega_e/2$. Given that the background Langmuir turbulence may have a wide angular spectrum, it is possible to find the range of angles between the Langmuir wave and RH wave k-vectors. The dispersion relation for right hand circularly polarised waves in a two fluid plasma (consisting of electrons and protons) and is shown below.

$$\frac{k_{RH}^2 c^2}{\omega_{RH}^2} = 1 - \frac{\omega_p^2}{(\omega_{RH} + \omega_{Ci})(\omega_{RH} - \omega_{Ce})} \tag{4.3}$$

By approximating the ion cyclotron frequency to be small, we can write the above

equation as

$$\frac{k_{RH}^2 c^2}{\omega_{RH}^2} = 1 - \frac{\omega_p^2}{(\omega_{RH})(\omega_{RH} - \omega_{Ce})} \tag{4.4}$$

This can further be reduced using the approximations that $\omega_{Be} << \omega_p$ and $\omega_{RH} \leq \omega_{Be}$. This allows us to neglect the first term on the right hand side of the equation. Solving for ω_{RH} then yields the following.

$$\omega_{RH} = \omega_{Be} \frac{k_{RH}^2 c^2}{k_{RH}^2 c^2 + \omega_p^2} \tag{4.5}$$

Melnik et al. (2010) explain that the interaction between the Langmuir waves and the RH waves can generate electromagnetic waves with a frequency equal to the upper hybrid resonance frequency, ω_{UH}, plus half the electron cyclotron frequency, $\Omega_e/2$. In terms of the k vectors of the involved waves, we can write this interaction in the following manner.

$$k_{RH} + k_L = k_{UH} + k_{Ce}/2 = k_{EM} \tag{4.6}$$

The magnitude of $k_L = \omega_p / v_{beam}$ is larger (by a factor of about ten in this case) than the corresponding magnitude of the wavenumber of an electromagnetic wave at ω_p, which is given by $k_{EM} = \omega_p / c$. However, when Langmuir and RH waves merge, their wave numbers are added as vectors, i.e. taking into account the angle between these two vectors. Consequently, they show that

$$\frac{\Delta f}{f} = \frac{\Omega_e^2}{2\omega_p^2} \sin^2 \theta, \tag{4.7}$$

where f is the frequency and Δf is the instantaneous bandwidth of the bursts. The value θ is the angle width of the Langmuir waves spectrum. This is a measure of the isotropy of the Langmuir waves involved in the interaction that produces the electromagnetic radiation. Rearranging Equation 4.7 in terms of the magnetic field, B, at the source height of the bursts we get the following expression:

$$B = \frac{\sqrt{8}\pi m_e}{e} f \sqrt{\frac{\Delta f}{f}} \frac{1}{sin\theta}. \tag{4.8}$$

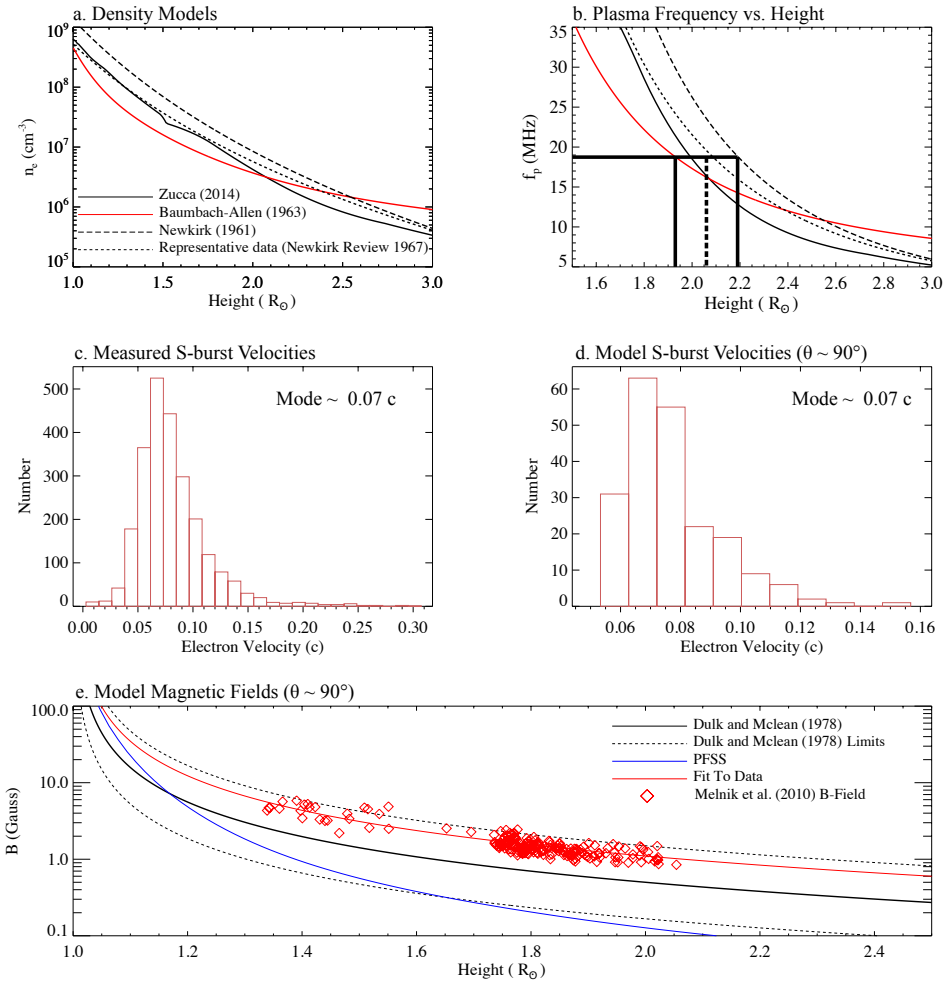

Figure 4.6: Panel (a): Electron density vs. heliocentric height for the active region electron density models of Zucca et al. (2014), Baumbach-Allen (Aschwanden, 2005), Newkirk Jr. (1961), and Newkirk Jr. (1967). Panel (b): The plasma frequency vs. heliocentric height for each density model. An example of how we estimated the source height of an S-burst with a frequency of ∼19 MHz is shown. Panel (c): Distribution of measured source electron velocities. Panel (d): Source electron velocity distribution according to the model of Melnik et al. (2010) when using a value of $\theta = 90°$. Panel (e): The magnetic field strengths predicted by Melnik et al. (2010) at each of the source height estimates according to our data. In this case, a value of $\theta = 90°$ is used to allow for a source velocity of 0.07 c as implied by our observations.

Melnik et al. (2010) also derived a source velocity from the dispersion equation for RH waves propagating through the solar atmosphere, which is given below as

$$v_s = \frac{\Omega_e}{2\omega_p} c. \tag{4.9}$$

This equation can be written as

$$v_s = \frac{eB}{m_e}\frac{1}{4\pi f}c. \tag{4.10}$$

Given that the model assumes emission close to the plasma frequency, we can estimate the source heights for each burst. To do this, the active region coronal electron density models of Zucca et al. (2014), Baumbach-Allen (Aschwanden, 2005), Newkirk Jr. (1961), and Newkirk Jr. (1967) were used. These models are based on a variety of observational techniques based on radio emission from the solar corona. Figure 4.6a shows these electron density models, while Figure 4.6b shows how the plasma frequency varies with height for each model. Figure 4.6b also gives an example of how we estimated the source height of an S-burst with a frequency of ∼19 MHz. As shown, we calculated a minimum and maximum height and then used the average (dashed line) of these heights as our estimation. It is now possible to test this model further by inputting our data into Equation 4.8 to calculate the source region magnetic field strengths that it predicts at specific heights above the solar surface. We then compared the strength of the magnetic field at each estimated height with the active region magnetic field model of McLean et al. (1978) and a PFSS extrapolation.

To calculate the magnetic field strength at the source height of the bursts according to the model of Melnik et al. (2010), it is clear that a value of theta must be chosen. Melnik et al. (2010) found that this value must be between 50°-90° (partially or completely isotropic Langmuir turbulence) to satisfy the condition that S-burst sources move at velocities of ∼0.1 c. To constrain our choice of theta, we estimated the source electron velocities of all the S-bursts observed by UTR-2 and LOFAR. To do this, we calculated the source heights at the start and end of each burst via the density models, found the corresponding heights, and then calculated the velocities by dividing the distances travelled by the durations of the bursts. As shown in Figure 4.6c, the bursts were found to have a mode velocity of ∼0.07 c. A value of $\theta \sim 90°$ produces a distribution of magnetic fields that results in a mode velocity of $\sim$ 0.07 c, according to Equation 4.10, indicating isotropic Langmuir turbulence. Figure 4.6d shows the distri-

bution of velocities calculated via Equation 4.10. Figure 4.6e shows the magnetic field strengths predicted by the model of Melnik et al. (2010) at each of the source height estimates when we input our data. It was found that the magnetic field strengths ranged from 0.9-5.8 G between heights of ∼1.3-2 $R_{\odot}$. Overplotted is the active region magnetic field model of McLean et al. (1978) and a PFSS extrapolation taken at a longitude corresponding to active region NOAA 11785, where the highest magnetic field strengths were observed at the time. The McLean et al. (1978) model is accurate to within a factor of ∼3 between 1.02 $R_{\odot}$ and 10 $R_{\odot}$ and so the relevant error limits are included. The Dulk and Mclean (1978) model is given by the relation

$$B = 0.5\big[R/R_{\odot} - 1\big]^{-1.5}. \tag{4.11}$$

As shown in Figure 4.6e, the data points lie between the standard and upper limit of the McLean et al. (1978) model and appear to follow the same general form. A fit of the data was performed that allowed the coefficient (0.5) of Equation 4.8 to vary. A value of 1.1 was found and the corresponding fit is shown in red in Figure 4.6e. To verify the accuracy of the Melnik et al. (2010) model magnetic field strengths, we compared the magnetic field at 1.02 $R_{\odot}$ according to the PFSS extrapolation with the value found at the same height obtained via the extrapolation of the fitted data. The values were found to be ∼332 G and ∼389 G, respectively. These fields are in good agreement indicating that the fit to the data may provide us with the ability to conduct remote sensing of the coronal magnetic field on the day of the observations. It is thought that PFSS extrapolations underestimate the coronal magnetic field at high altitudes of the solar atmosphere, however, they are thought to be more accurate closer to the surface. The slow decrease in the magnetic field according to the fitted data may be attributed to the higher than usual surface magnetic fields observed on 9 July 2013 of ∼1.7 kG in the active region NOAA 11785.

We note that S-bursts are very narrow-band phenomena that are characterised by localised pockets of emission that occur over a wide range of heights. To explain these pockets of emission, we propose that S-burst sources propagate along closed coronal

loops. It is possible that the source particles are accelerated within the active region and then escape along a set of "stacked" coronal loops that stretch to higher and higher altitudes. The higher frequency emission would correspond to lower altitude loops, while the lower frequency emission would correspond to loops that stretch to higher altitudes. This would support our observations of reverse drift S-bursts and could explain their short durations and narrow frequency bands. High spatial resolution interferometric imaging is needed to confirm this idea.

4.3 Conclusions

Over 3000 S-bursts were observed in a frequency band of 18.7-83.1 MHz by UTR-2 and LOFAR on 9 July 2013 from the solar disc. The S-bursts were found to have short durations of ∼0.5-0.9 s. The FWHM durations of the S-bursts ranged from 0.02-0.6 s. The S-bursts were observed to have a total frequency bandwidths of 1.21 ± 0.32 MHz and 2.30 ± 0.43 MHz using the UTR-2 and LOFAR data, respectively. The instantaneous bandwidths of the bursts ranged from 0.14-2.04 MHz. These results agree well with those of previous authors (Dorovskyy et al., 2017; McConnell, 1982; Melnik et al., 2010; Morosan et al., 2015). A linear relation (slope of 0.022 and intercept of -0.22) between instantaneous bandwidth and frequency (central frequencies) was found, extending the results of Melnik et al. (2010) over a wider frequency band. A functional dependence between the frequency and drift rate of S-bursts was observed using data from multiple instruments. This dependence was represented by a power law of the form $df/dt = -af^b$, where a was found to be 0.0084 ± 0.006 and b was found to be 1.57 ± 0.17. These values are close to previously obtained results (Dorovskyy et al., 2017; McConnell, 1982; Morosan & Gallagher, 2018). The flux values of S-bursts, type III radio bursts, and type IIIb radio bursts were measured and compared. Type IIIb radio bursts were found to have a broader flux distribution. No dependence of flux on frequency or flux on FWHM duration was observed.

Leading theories of S-burst generation were investigated, particularly the models proposed by Melnik et al. (2010) and Zaitsev & Zlotnik (1986). Several active region

electron density models were used to estimate the heights at which the observed bursts would be generated (∼1.3-2 $R_{\odot}$). It was noted that the model of Zaitsev & Zlotnik (1986) was unable to account for the properties of S-bursts that are commonly observed at decametre wavelengths. The source electron velocities of S-bursts were found to be ∼0.07 c. According to the model of Melnik et al. (2010), it was found that the magnetic field strengths at the source heights of S-bursts ranged from 0.9-5.8 G. The model of Melnik et al. (2010) can enable us to conduct remote sensing of the coronal magnetic field. This model can account for the observed spectral properties of S-bursts and produced magnetic fields that are in good agreement with observations and coronal magnetic field models. However, a more detailed theoretical framework is needed to describe this mechanism in full. The study of S-bursts and their properties can help us to understand the physics of the coronal plasma. Higher time and frequency resolution imaging would enable us to study the spatial structure of S-bursts in more detail in order to further understand their nature. This work was published in the journal *Astronomy & Astrophysics* (Clarke et al., 2019).

5

Quasi-periodic Particle Acceleration in a Solar Flare

In this chapter, a study is presented that demonstrates prominent QPPs occurring over an unusually wide range of frequencies. We observe non-thermal emission in the form of HXRs produced via bremsstrahlung in the chromosphere, co-temporal thermal emission via SXR and EUV emission in the flare loops/transition region, as well as a sequence of low frequency type III bursts emanating from the high corona. We analyse the multiple types of emission mechanisms at play including thermal emission, plasma emission, and non-thermal bremsstrahlung. These mechanisms are all associated with the same intermittently accelerated electron beams which result in the pulsations that we can localise to a specific region of the flare site. This region is associated with a system of open and closed field lines. Identifying the source region responsible for the intermittent acceleration of the electron beams is novel from the perspective of analysing QPPs. This work provides new observational evidence that QPPs can originate from an identifiable specific regions of flares and manifest across the entire electromagnetic spectrum via multiple emission mechanisms. The QPPs observed in the radio regime are notably lower in frequency compared to what is typically observed. This indicates the considerable distances over which QPPs can manifest - from the solar chromosphere through to interplanetary space ($\sim$16 $R_{\odot}$)

The flare presented in this paper is a Geostationary Operational Environmental Satellite (GOES) M3.7 class flare that occurred on 04-Nov-2015. An overview of the

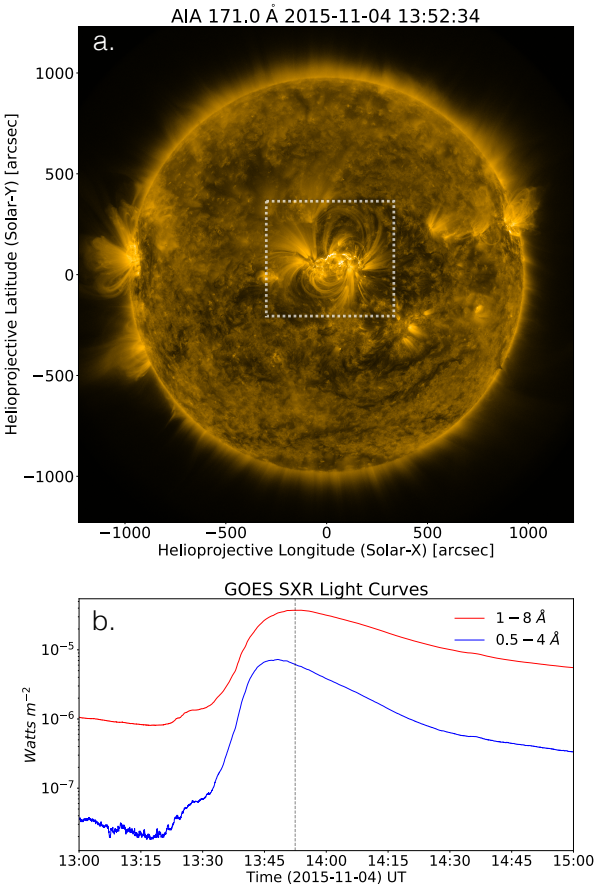

Figure 5.1: (a): SDO/AIA 171 Å passband image of the sun on 2015 Nov 4. The active region associated with the event is visible in the dashed box at the disk center. (b): The GOES SXR light curves showing the occurrence of the M3.7 class flare. The dashed grey line shows the time at which the image in panel a was taken.

active region located at the center of the solar disk as observed in 171 Å is shown in Figure 5.1a and the light curves of the flare from the GOES X-Ray Sensor (XRS) in two channels (1-8 Å in red and 0.5 - 4 Å in blue) is shown in Figure 5.1b. In Section 5.1.1, the instruments used for this study: The Atmospheric Imaging Assembly (AIA) on board the Solar Dynamics Observatory (SDO) (Lemen et al., 2012a), the Reuven Ramaty High Energy Solar Spectroscopic Imager (Lin et al., 2002), the WAVES instrument on board the WIND satellite (Bougeret et al., 2008), The Gamma-ray Space Telescope (GBM) onboard Fermi (Meegan et al., 2009), and the GOES XRS are briefly introduced. Details of the analysed event and data analysis techniques are also included in this section. In Section 5.2, we present our observations alongside our analysis of the QPPs. In Section 5.3, we present a discussion and interpretation of the work before concluding our findings.

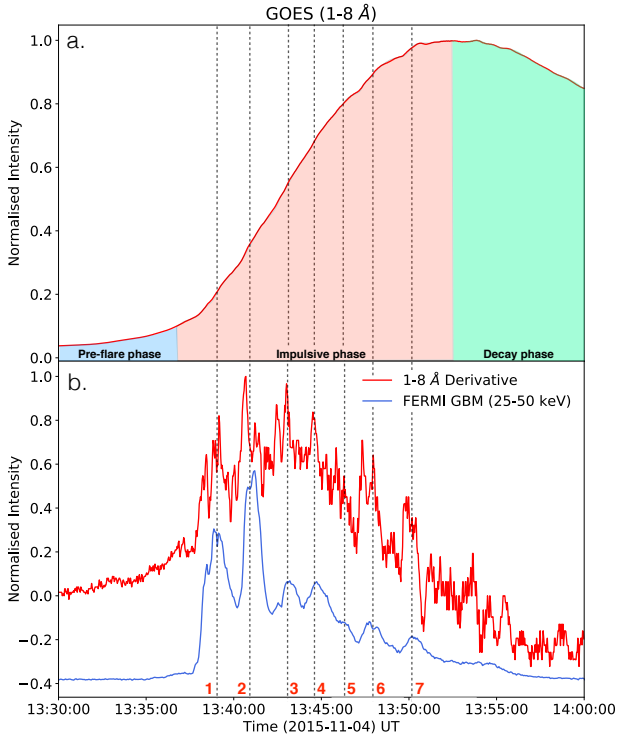

Figure 5.2: (a): The normalised SXR light curve from GOES (1-8 Å) at the time of the flare. (b): The time derivative of the SXR emission and the HXR light curve from FERMI GBM (25-50 keV). The QPPs present are labelled one through seven. Here, we see a clear illustration of the Neupert effect and indicate the seven primary QPPs analysed in this work.

5.1 Instrumentation, observations, and data analysis

5.1.1 Instrumentation and observations

The GOES XRS measures the solar SXR fluxes integrated over the entire solar disk. It has a cadence of 2 s with two channels of 0.5-4 Å and 1-8 Å. In this work, we primarily focus on the 1-8 Å channel as it exhibited the most pronounced QPPs. Figure 5.2a shows this light curve. The pre-flare, impulsive, and decay phases are also indicated. The event began at 13.31 UT and peaked at 13.52 UT. Figure 5.2b shows the time derivative of this light curve with the HXR light curve observed by FERMI GBM (25-50 keV) overplotted. The Neupert effect, which refers to the observed phenomenon that non-thermal HXR emission coincides temporally with the rate of rise of the thermal

SXR emission (i.e. the derivative), is observed here as it is clear that the pulsations in the SXR derivative are coincidental with those observed in the HXR emission (Neupert, 1968b). This relates the HXR flux from the flare 'footpoints' to the thermal SXRs observed from the heated plasma. We identify seven distinct pulsations throughout the event as shown in Figure 5.2b. One can see that these pulsations all occur during the impulsive phase of the flare. This indicates that the mechanism producing these QPPs must be able to modulate the acceleration of electrons. However, it is clear that some pulsations do persist into the decay phase within the SXR emission.

The most pronounced pulsations we observed with AIA were from the 171 Å and 1600 Å passbands. Images from these passbands were used to analyse the periodicity and spatial distribution of the QPPs in EUV. The cadences of these images were 12 s and 24 s, respectively. The 171 Å passband is dominated by the Fe XI line and most represents emission from the corona and upper transition region while the 1600 Å passband is dominated by C IV and images primarily the upper photosphere/transition region (Lemen et al., 2012b). These images enable us to estimate the layer of the atmosphere from which the QPPs we observe originate and how they relate to one another.

RHESSI observed the event up until 13:43 UT before entering spacecraft night. This allowed us to image the location of the HXRs produced during the flare for our analysis. Although RHESSI was unable to observe all the HXR emission throughout the flare, Fermi GBM captured this information which we incorporate into our analysis. The WIND/WAVES RAD2 instrument was used to gather radio data. Dynamic spectra from 0.02-13.85 MHz (cadence: 16.188 s) were analysed to investigate the low-frequency aspect of the QPPs in the event. The emission at these wavelengths manifests in the form of type III radio bursts which are a result of plasma emission (Reid & Ratcliffe, 2014). Within this mechanism, the frequency, f_p, of the radiation is proportional to the local electron density n_e via $f_p \sim 8980\sqrt{n_e}$. The electron density in the corona decreases with height. Hence, by using an electron density model, the height of a radio source produced through plasma emission may be estimated. At the frequency of 2.5

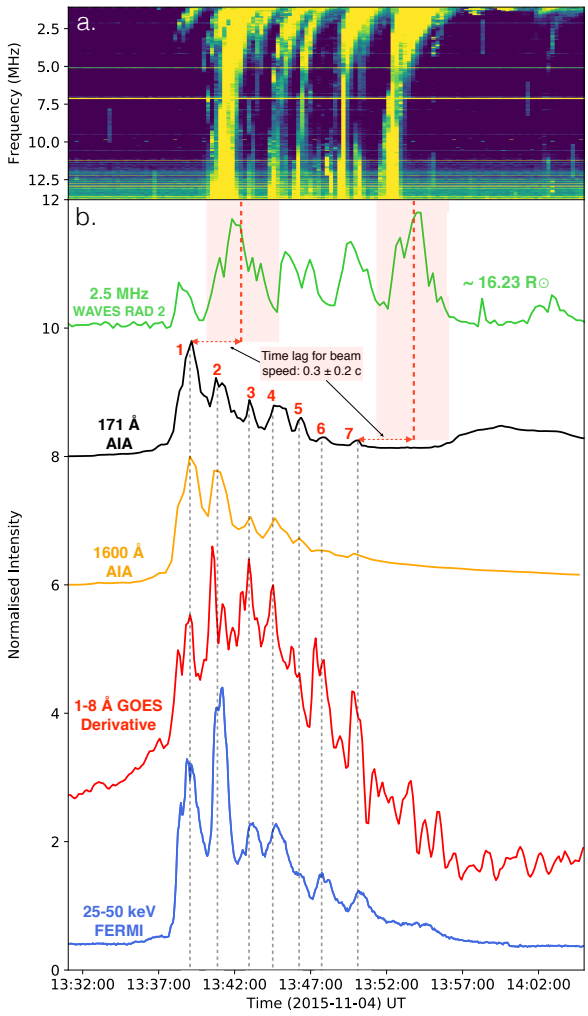

Figure 5.3: (a): Dynamic spectrum from WIND/WAVES RAD2 showing a series of pulsed type III radio bursts. (b): Multi-wavelength light curves observed from a number of instruments. From top to bottom the lightcurves go from longer to shorter wavelenghts. This is a proxy for altitude of the flaring emission source with the radio data representing emission originating from high in the corona down to the HXR emission originating from the footpoints. The black, orange, red, and blue light curves have QPPs well correlated in time. The green light curve shows the radio emission at 2.5 MHz. This frequency was chosen as it captured each pulse most effectively. The radio QPPs have a longer periodicity which we elaborate on in the discussion section. Lines drawn from pulses 1 and 7 show the time lag needed for the source electron beams of typical speeds to reach 16 $R_\odot$ (approximate height of the radio source) from the flare site.

MHz, most of these bursts are captured and so we use this frequency to generate a light curve of the radio data. Using the electron density model from Newkirk Jr. (1967), this corresponds to a height of $\sim$16 $R_\odot$.

Together, we can use these data to determine information about the periodicity and location of the QPPs observed from the HXR footpoints through to the upper transition region and corona. The altitude at which each different waveband emits

differs significantly. For example, the HXRs are produced through bremsstrahlung by non-thermal electrons colliding with the chromosphere while the type III radio bursts are produced via plasma emission. Figure 5.3 is summary of the QPPs analysed in this work. Figure 5.3a shows the dynamic spectrum of the radio emission containing a sequence of type III radio bursts and Figure 5.3b shows the EUV, SXR and HXR light curves in which we identify 7 distinct QPPs. The EUV light curves were extracted from the QPP source region we identified which is explained in Section 5.2.2.

5.1.2 Data analysis and imaging

5.1.2.1 Wavelet analysis

Wavelet analysis using a Morlet wavelet was performed on the multiwavelength light curves to determine their periodicities using the software[1] developed by Torrence & Compo (1998). This technique is a powerful tool for searching within time-series for periodic signatures as, unlike Fourier analysis, it provides a 2D spectrum of both frequency and time allowing one to assess if a quasi-periodic signature varies in time (De Moortel et al., 2002).

Wavelet analysis involves involves carrying out a convolution of a wavelet function, $\psi(\eta)$, with time-series data. The wavelet function must have a non-zero mean, be localised in time and frequency space, and depends on a time parameter, η. A plane wave modulated with a Gaussian, known as a Morlet wavelet, is typically used and is given by

$$\psi_0(\eta) = \pi^{-1/4} e^{i\omega_0 \eta} e^{-\eta^2/2} \tag{5.1}$$

where ω_0 is the associated frequency. For a time series, x_n, its wavelet transform is then given by

$$W_n(s) = \sum_{n'=0}^{N-1} x_{n'} \psi^* \left(\frac{(n'-n)\delta t}{s} \right) \tag{5.2}$$

where ψ^* is the complex conjugate of the wavelet and the wavelet scale is described by s. The scale parameter is then allowed to vary resulting in an array of wavelet

[1] http://atoc.colorado.edu/research/wavelets/

transforms. Taking the square of $W_n(s)$ yields the wavelet power spectrum at each scale indicating the dominant periodicities present. A red noise background model was used to determine the significance of the wavelet power which is given by

$$x_n = \alpha x_{n-1} + z_n \tag{5.3}$$

where z_n represents white noise and α represents the lag-1 autocorrelation.

In order to more accurately determine the period of the QPPs via the wavelet analysis, the slowly varying background trend of the flare emission was removed from each time-series. This process is shown in Figure 5.4 for the case of the SXR emission from GOES. To do this, a spline fit was constructed using a 3rd order polynomial with 28 samples between nodes. The fit was then subtracted from the original data resulting in a time-series containing only the modulation of the emission resulting from the QPPs. This process was repeated for each time-series we analysed. No subtraction was required for the radio light-curve at 2.5 MHz as there was little background in this data. Care was taken to ensure each fit accurately represented the slowly varying background emission in order to avoid introducing any artefacts during the subtractions.

In addition to carrying out the wavelet analysis on the multi-wavelength detrended time-series, we also performed the same analysis on the relevant data without detrending in order to cross-check our results. We also manually determined the period of the QPPs. This was achieved by visually identifying the time of each pulse and plotting these times against pulse number (1-7). The period can then be simply estimated by fitting a straight line to this data and finding the slope.

5.1.2.2 Imaging

The PIXON algorithm was used to image the RHESSI HXR sources. It seeks a superposition of circular sources of different sizes and parabolic profiles that most replicate the modulations measured by the detectors, while maintaining the fewest degrees of freedom possible. PIXON is thought to provide accurate image photometry in comparison to the other faster algorithms such as CLEAN (Hurford et al., 2002). Images taken

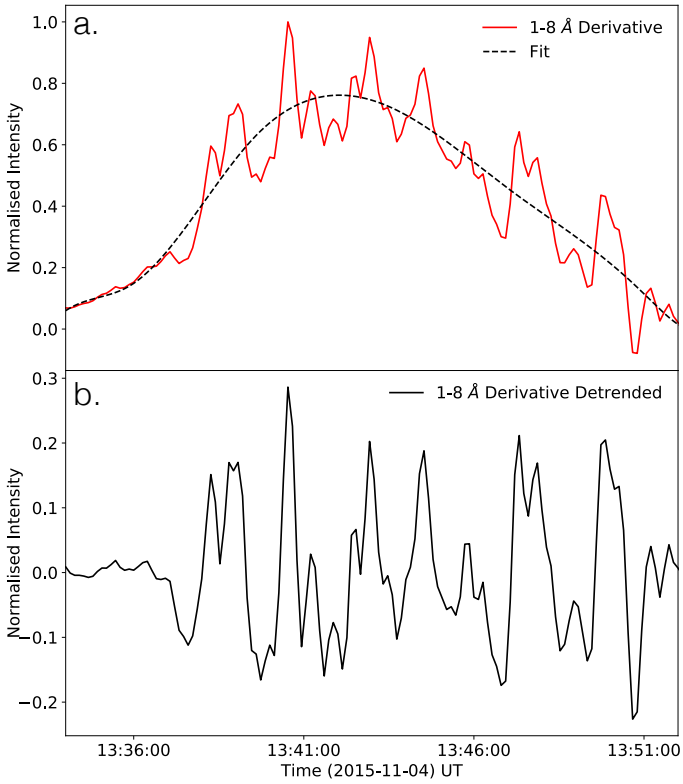

Figure 5.4: Example of the background subtraction technique used to isolate the QPPs. (a): The time derivative of the SXR emission is shown in red with a spline fit to the overall large-scale slowly varying emission overplotted in black . The fit excludes the shorter time-scale variation of the QPPs. (b): The subtraction of the fit from the SXR emission resulting in a time-series containing the QPPs without the slowly varying background emission.

by SDO/AIA were used to analyse the most prominent pulsations in the EUV regime which were found in the 171 Å and 1600 Å passbands. Time-series were constructed from these images by integrating the emission over various regions of the flare in order to localise the area producing the pulsations. This is discussed further in Section 5.2.2. Additional data analysis was carried out to estimate the height of the source producing the radio emission via the Newkirk Jr. (1967) electron density model. This height was determined to be $\sim$16 $R_{\odot}$. Figure 5.3b shows the time lag required to reach this height from the flaring region with beam speeds of 0.1-0.5 c. Type III radio bursts typically have source electron beam velocities of $\sim$0.3 c but have been found to vary from 0.1-0.5 c in some cases (Reid & Ratcliffe, 2014).

5.2 Results

Across the electromagnetic spectrum, the impulsive nature of the event begins at approximately 13.37 UT and continues until approximately 13.57 UT. Figure 5.3 shows the normalised lightcurves under investigation that spans from the HXR to the low frequency radio emission, all of which contain QPPs. The lightcurves were normalised by dividing each time series by its peak value. They were then scaled in order to plot them in a vertical sequence for ease of comparison, going from higher frequency to lower frequency (bottom to top). The HXR light curve (25-50 keV) from Fermi/GBM in blue is at the bottom of Figure 5.3b, with the most prominent pulsations labelled one through seven. Above in red, is the derivative of the GOES light curve (1-8 Å), followed by the 1600 Å curve in orange, and the 171 Å curve in black. The clear co-temporal presence of the pulsations in each of these light curves obtained by simultaneous observations from different instruments makes clear that these QPPs are of solar origin and are not due to some instrumental effect. Figure 5.3a shows the dynamic spectrum from WIND/WAVES RAD2 (1.075–13.825 MHz) that contains a series of pulsed type III radio bursts during the same time frame in which the QPPs were observed. The green light curve in Figure 5.3b shows a slice from this dynamic spectrum at 2.5 MHz. This frequency was chosen as it contained the majority of the bursts. Using the Newkirk Jr. (1967) electron density model, we can estimate the height at which this radio emission is emitted: $\sim$16 $R_{\odot}$. Lines drawn from the peaks of pulses 1 and 7 from the 171 Å curve are shown that indicate the time delay required for electron beams of velocities between 0.1 and 0.5 c to reach this height. For both pulse 1 and 7, there appears to be radio pulsations that occur at the expected times. This analysis suggests that the electron beam speeds are close to the typical value of 0.3 c for type III radio bursts. It is clear that the radio QPPs at 2.5 MHz are less correlated with the higher frequency radiation. There are a number of reasons for which one would not expect a one-to-one relation between radio pulsations produced via plasma emission in interplanetary space and the higher frequency emission produced via bremsstrahlung/heating close to the

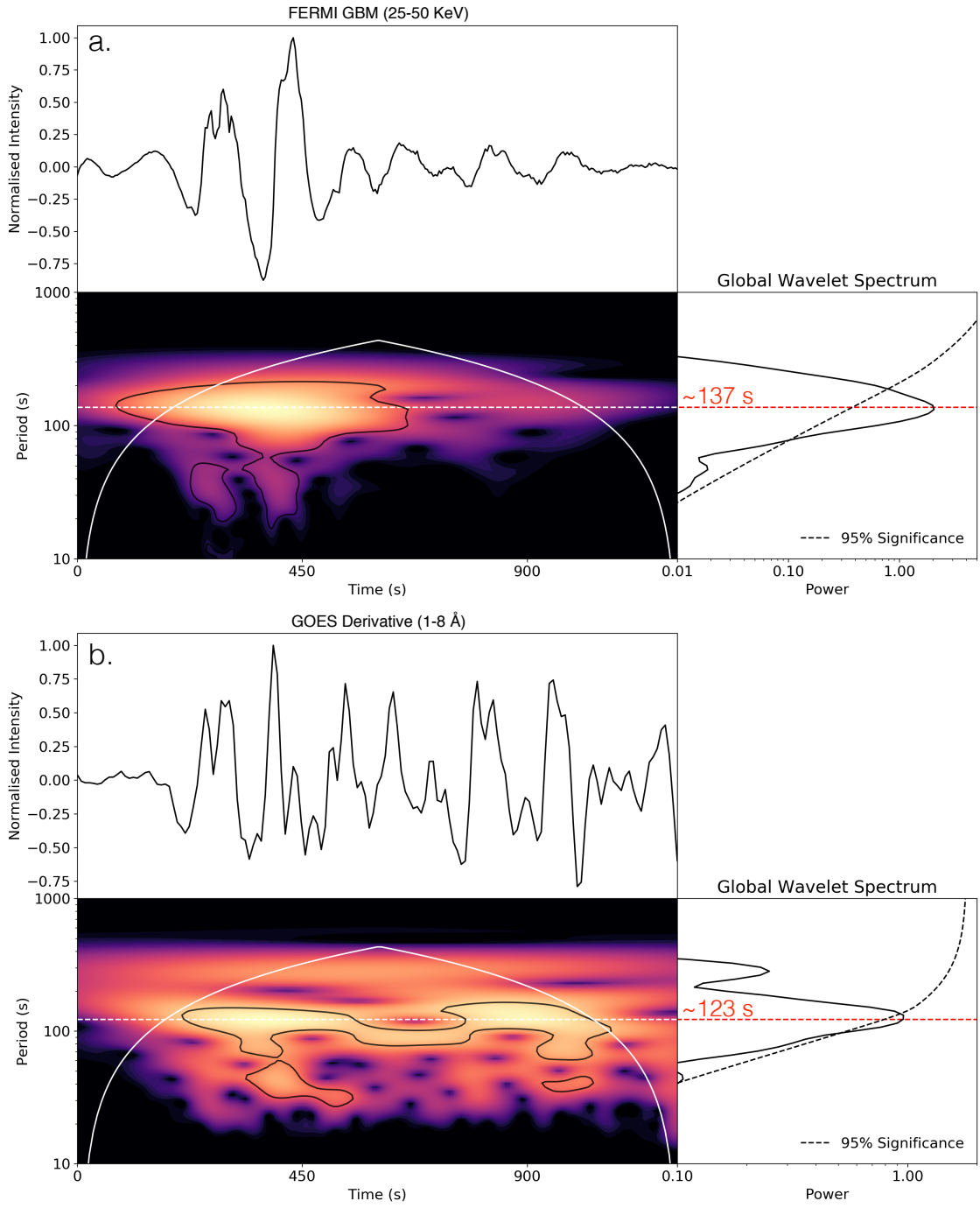

Figure 5.5: Wavelet analysis of the detrended (a): HXR and (b): SXR derivative emission from the flare. The periods were found to be 137^{+49}_{-56} s and 123^{+11}_{-26} s, respectively. These values were found via the peaks of the global wavelet spectra and the errors are taken as the range over which each global power spectrum is above 95% significance.

flare site despite originating from the same populations of accelerated electrons. These differences are elaborated upon in the discussion section.

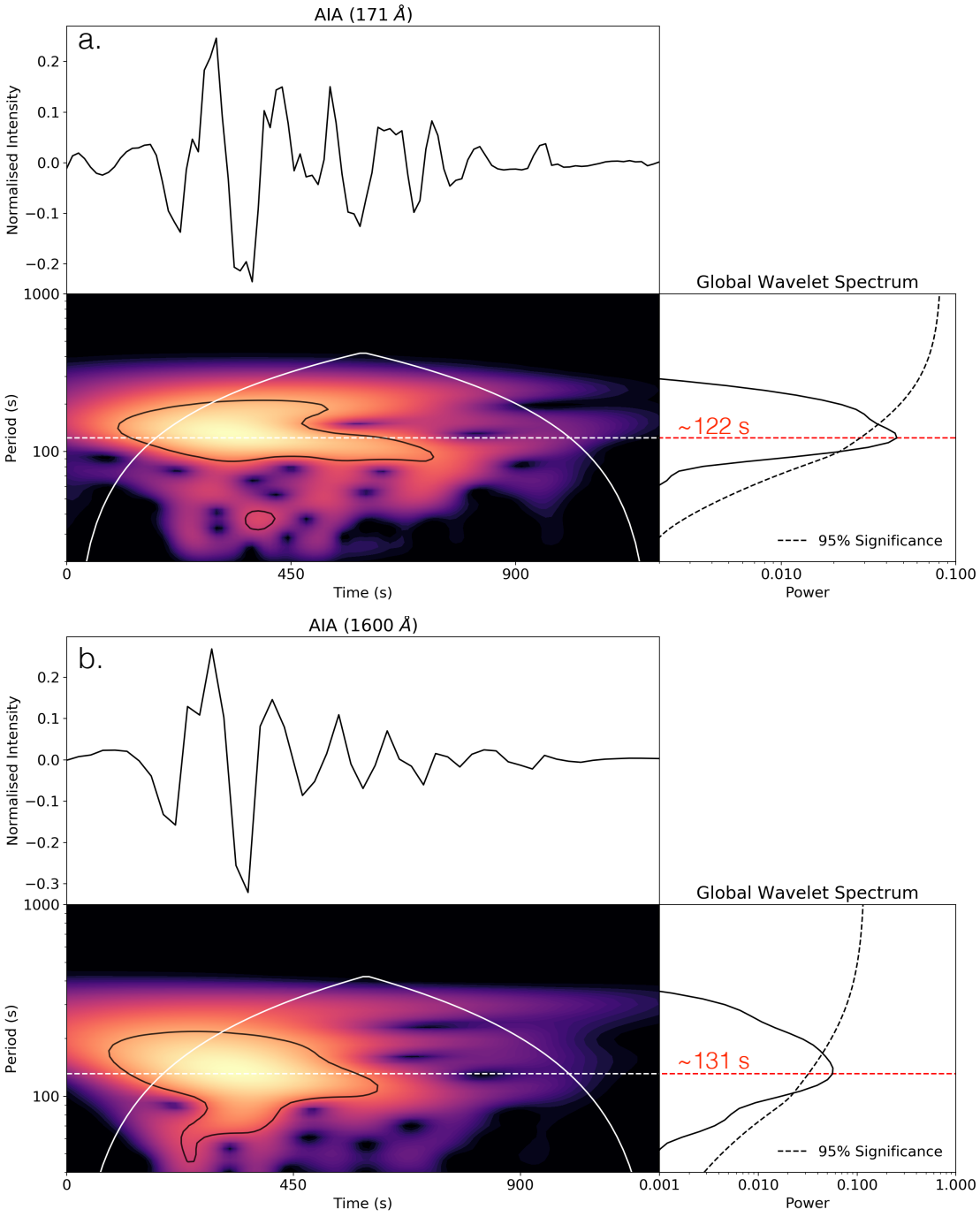

Figure 5.6: (a): Wavelet analysis of the detrended emission at 171 Å. (b): Wavelet analysis of the emission at 1600 Å. The periods were found to be 122^{+26}_{-22} s and 131^{+36}_{-27} s respectively.

5.2.1 Periodicities

For each lightcurve, wavelet analysis was conducted over the same time period: 13:34-13:54 UT. The error for each result was taken as the range over which the global power spectrum was above the 95% significance curve. The analysis was carried out on the

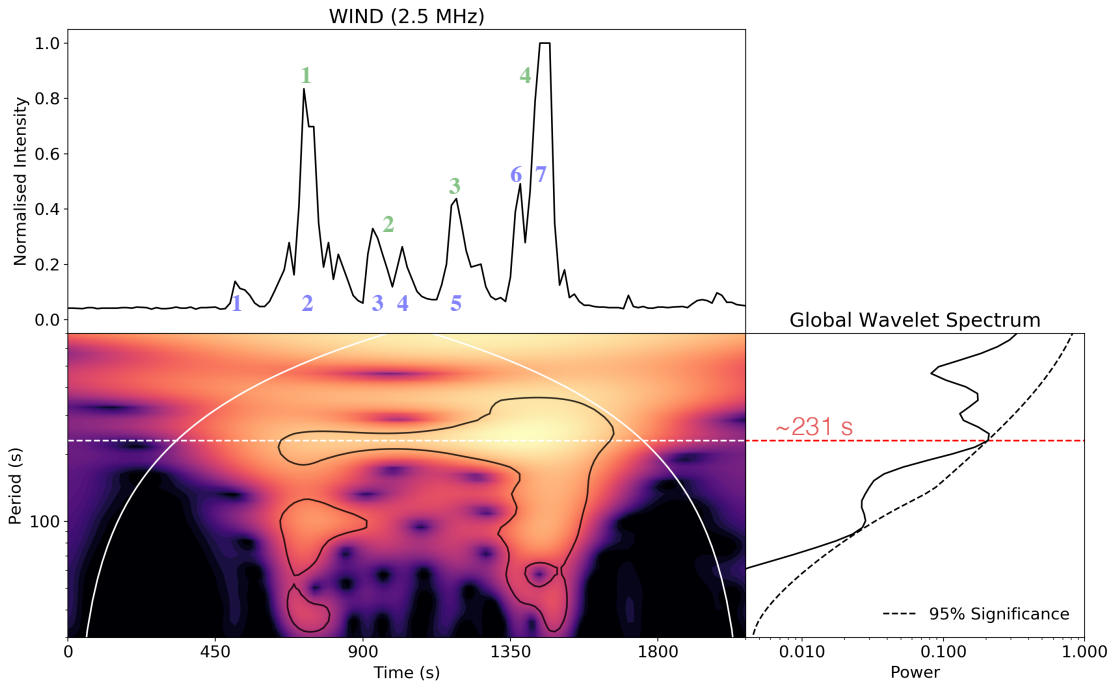

Figure 5.7: Wavelet analysis of the radio emission at 2.5 MHz. The period was found to be ∼231 s.

detrended light curves. However, the same analysis for the data without detrending. The results agreed in both cases.

Figure 5.5a shows the wavelet analysis that was carried out on the GBM 25-50 keV lightcurve. In this plot, the HXR time-series, the wavelet power spectrum, illustrating power at particular periodicities as a function of time, and the global power spectrum are shown. A period of 137^{+49}_{-56} s was found in this channel. Figure 5.55b, Figure 5.6, and Figure 5.7 show this same analysis for the SXR, EUV, and radio wavelengths, respectively. The SXR emission contained a period of 123^{+11}_{-26} s, while the pulsations within the 171 Å and 1600 Å light curves yielded periodicities of 122^{+26}_{-22} s and 131^{+36}_{-27} s, respectively. The 2.5 MHz light curve was found to have significant period at a time-scale of ∼231 s. The time-scales of the QPPs in in the 171 Å, 1600 Å, SXR (1-8 Å), and HXR (25-50 keV) are therefore all in good agreement within error. These results are summarised in Table 5.1.

In addition to calculating the periods of the light curves via wavelet analysis, we also estimated them manually by visually identifying peaks. Figure 5.8 shows the time of the HXR, EUV, and SXR pulsations versus pulse number (see pulses 1-7 in

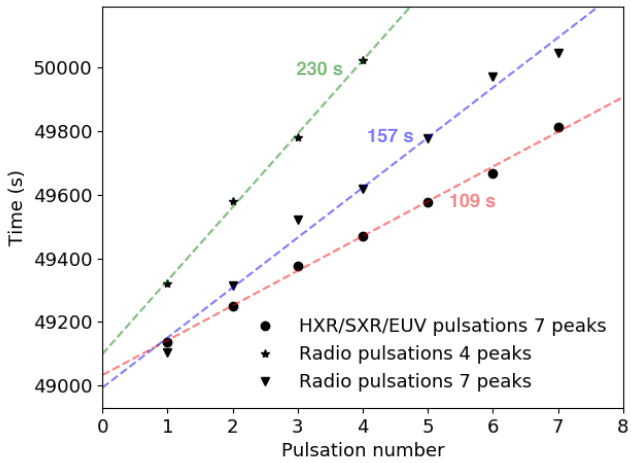

Figure 5.8: Pulse number versus time of each pulse. The 7 HXR/SXR/EUV pulses shown in Figure 5.3 are plotted using the circle symbols. The slope of the straight line fitted to the data provides an estimate of the period: $\sim$ 109 s. For the radio emission at 2.5 MHz, this analysis was done for the four main peaks in the time-series, as well as for seven peaks in the case where lower amplitude peaks are included. This resulted in periods of $\sim$ 230 s and $\sim$ 157 s, respectively.

Figure 5.3). The slope of this line provides an estimate of the period. The result was found to be $\sim 109 \pm 13$ s (5σ uncertainty). This agrees with the results of the wavelet analysis within error. For the radio emission at 2.5 MHz, this analysis was done for the four main peaks in the time-series, shown in green in Figure 5.8 as well as seven peaks which include lower amplitude pulsations, shown in blue in Figure 5.8. This resulted in periods of $\sim$ 230 s and $\sim$ 157 s, respectively. Therefore, this result matches well with the wavelet analysis when only the four main peaks are accounted for. When the less significant peaks are included, we see that the period draws closer to that of the higher frequency radiation. The matching time-scales of the 171 Å, 1600 Å, SXR, and HXR light curves indicate that the mechanism producing the QPPs in these wavebands must have the same progenitor, that is also likely related to the radio emission observed. Our interpretation of these results and the relationship between the emission in each waveband is detailed in Section 5.3.

Table 5.1: Comparison of the periods found in the lightcurves for each analysed wavelength via wavelet analysis. The cadence of the data in each case, Δt, is also shown.

λ	2.5 MHz	171 Å	1600 Å	1-8 Å	25-50 keV
Period	$\sim$231 s	122^{+26}_{-22} s	131^{+36}_{-27} s	123^{+11}_{-26} s	137^{+49}_{-56}
Δt	16.2 s	12 s	24 s	2 s	1.6

5.2.2 Spatial analysis

To investigate spatially the regions of the flare from which the QPPs originate, we conducted imaging analysis using RHESSI and SDO/AIA. No radio imaging instrument was available during the observation. Firstly, we used the PIXON algorithm to determine where the non-thermal HXRs originated from. The imaging was carried out over an energy band of 35-70 keV during the available time period when RHESSI was observing the event before entering spacecraft night: ∼13.35-13.42 UT. This includes the first two prominent pulsations in the sequence of 7. The light curve showing the available RHESSI data is shown in Figure 5.9 in magenta. It was found that there were three HXR sources on the map which are labelled within three kernels as K1, K2, and K3. The ribbons of the flare are clearly in visible in Figure 5.9a. K1 and K2 lie along the higher ribbon while K3 is located on the lower ribbon. A system of flare loops connects these ribbons. Figure 5.9a and Figure 5.8e show these sources in red overlaid on top of the 1600 Å and 171 Å backgrounds, respectively. The event occurred close to the disk centre and had a loop footpoint separation of ∼50 Mm and a loop height of ∼25 Mm. This was estimated by measuring the separation of the HXR footpoints and assuming a semi-circular geometry of the loops.

These HXRs are produced through non-thermal bremsstrahlung through interaction of the flare accelerated electrons with the dense chromosphere which acts a 'thick-target' (Brown, 1971). The mechanism modulating the HXRs that produces the observed QPPs must be causing a sequence of episodic or 'bursty' energy releases that intermittently accelerates electrons resulting in a modulation of the non-thermal bremsstrahlung emission. We discuss this further and its relevance to the QPPs in the other wavebands in Section 5.3.

To determine the location within the flaring region producing the QPPs in the 171 Å and 1600 Å emission, we created time-series from the images taken from SDO/AIA. To localise the QPP source, we integrated the emission from each image over each region of the entire active region using various kernel sizes, generated time-series for each of these kernels for the duration of the flare, and compared the profiles of the time-series

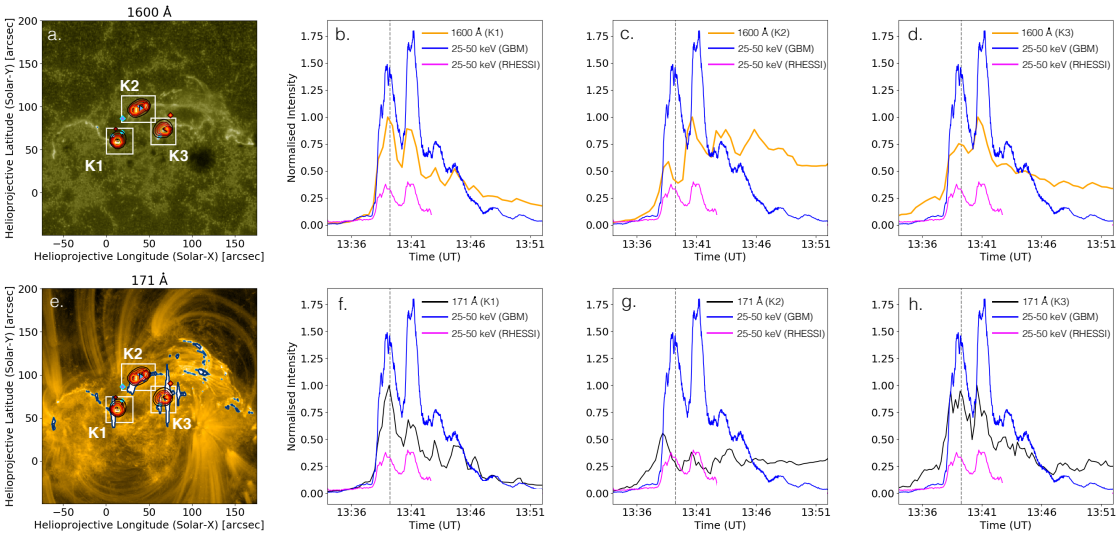

Figure 5.9: Spatial analysis of QPPs. (a): Image of the flaring region in 1600 Å taken at the time of the first QPP. The RHESSI image of the three HXR footpoints is overlaid which are labelled within three kernels as K1, K2, and K3. K1 and K2 lie along one flare ribbon while K3 is located on the other. This image was constructed using the PIXON algorithm over the available time period during which RHESSI captured the emission. This time period is shown in magenta with the time-series data in (b). (b-d): Light curves of the HXRs observed by GBM and RHESSI (25-50 keV) and the light curves extracted from the 1600 Å images taken by AIA at each HXR source location. The light curves were constructed by integrating over the pixels contained in the boxes surrounding the HXR sources in (a). The same analysis is done for the 171 Å images as shown in (e-h). It was found that the emission in EUV from within K1 produced light curves containing QPPs most correlated with those seen in the HXR emission (b+f). This localises the source of the QPPs to this region of the flare site which is close to a nearby system of open and closed magnetic field lines. The animation related to this Figure, provided in the online version of this article, shows the evolution of the flare at each time step from 13:34 - 13:53 UT.

to that of the HXR emission. This allowed us to obtain the flux from within each test kernel at each time-step to compare to the HXR emission. It was found that the kernel that produced the most prominent QPPs, as well as having the same characteristic periodicity as the HXR QPPs, spatially coincided with the location and size of the HXR source at K1. Figure 5.9b and Figure 5.9f illustrate this in that there is a strong correlation between the QPPs in the EUV emission extracted from K1 and the HXR emission. The EUV emission from K2 and K3 is significantly less correlated to the HXR emission as shown in Figures 1.9c, 1.9d, 1.9g, and 1.9f.

It is clear that there is an asymmetry between the light curves obtained for the EUV emission at each HXR source location with K1 being the most correlated to the

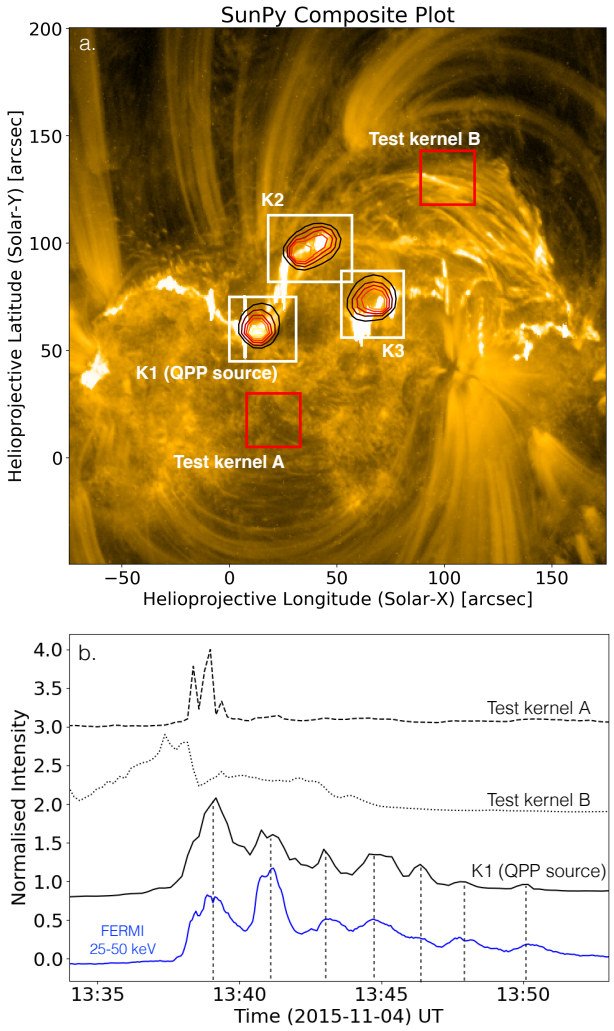

Figure 5.10: (a): SDO/AIA 171 Å passband image of the flare site on 2015 Nov 4. Shown are the QPP source (within K1), the additional two HXR sources (within K1 and K2), and two test kernels representing the arbitrary regions of the map. (b): The time-series obtained from K1 (QPP source) compared against those obtained from the test kernels. It is clear that the time-series constructed using the test kernels are uncorrelated to the HXR QPPs while the light curve obtained from K1 matches the HXR profile.

HXR QPPs. This analysis suggests that K1 is the region of the flare site in which the QPPs originate. Figure 5.10 shows an additional comparison of the EUV emission from K1 (QPP source) and the emission obtained from two test regions not associated with the HXR sources. Here, we can see again that integrating each time step over K1 produces QPPs highly correlated with the HXR emission while doing so for each test kernel does not. This trend continues no matter which region of the flare is used to construct the EUV time-series.

K1 is associated with open magnetic field lines, identified in the potential field

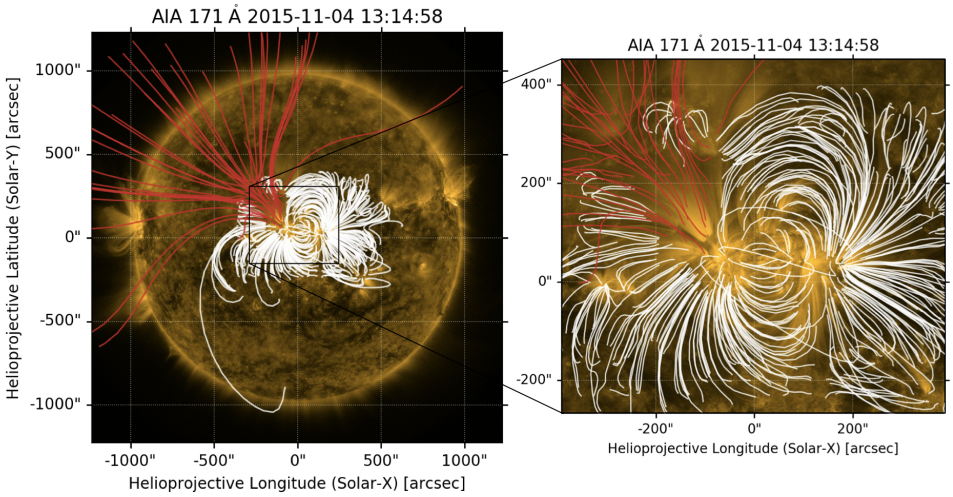

Figure 5.11: Potential Field Source Surface (PFSS) extrapolation showing the geometry of the magnetic field lines of the flaring region overlaid on the AIA 171 Å image. The open field lines are plotted in red and the closed lines in white. It is clear that the K1 has an open field line source and we propose that the interaction between the closed and open field lines at this footpoint result in 'bursty' magnetic reconnection giving rise to the QPPs we observe. The open field lines allow the flare-accelerated electrons to escape that produce the Type III radio emission.

source surface extrapolation (PFSS) shown in Figure 5.11. PFSS models provide an approximation of the coronal magnetic field up to 2.5 $R_{\odot}$ based on the observed photospheric field (Schrijver & De Rosa, 2003). Here the PFSS is calculated using `pfsspy` (Stansby et al., 2020). This is a python package used to carry out Potential Field Source Surface modelling. This magnetic field geometry allows for a mechanism for the escape of the electrons responsible for producing the radio emission. In the following section, we discuss the interpretation of these data and what proposed models of QPP generation allow for these observations.

5.3 Discussion and conclusions

Our results indicate that the EUV (171 Å and 1600 Å), SXR, and HXR QPPs contain approximately the same periodicity. We also observe QPPs in the low frequency radio domain in the form of a sequence of type III radio bursts that occur during the time of the flare that have a longer periodicity. Our spatial analysis suggests that the EUV and HXR QPPs originate from the same region of the flare - the HXR footpoint at K1. This

points towards a scenario in which intermittent particle acceleration is occurring due to a process inducing time-dependent magnetic reconnection. This particle acceleration occurs in a quasi-periodic fashion and results in bursty non-thermal bremsstrahlung that modulates the HXR emission occurring at the footpoints. The EUV emission would then be a consequence of this process as the ambient plasma is heated as the precipitating accelerated particles lose their energy.

The asymmetry of the EUV pulsations present at each HXR source, as shown in Figure 5.9, suggests that the electrons from the reconnection site must be preferentially accelerated between the closed loops and open field lines close to K1. Figure 5.11 shows these systems of open and closed field lines obtained via a PFSS extrapolation. It is likely that the radio emission observed is a consequence of the same intermittent particle acceleration that resulted in the EUV and HXR pulsations. However, the electrons accelerated along the open magnetic field lines from flare region result in the radio emission while it is the precipitating electrons accelerated towards the chromosphere which result in the HXR/SXR/EUV emission. Unfortunately no imaging observations at these radio frequencies are available during this event, and so we could not image the radio source to localise its origin. However, there are no nearby active regions at the time of the flare that could have coincidentally produced this radio emission.

To explain our observations we interpret the QPPs identified in this flare in terms of pulsed electron acceleration caused by time-dependent intermittent reconnection. In Figure 5.12 we show a cartoon scenario of the flare site to illustrate how the QPP sources are related to the magnetic field configuration. Following each burst of electron acceleration, those that escape upwards along the open magnetic field lines result in the type III QPPs, and those that travel along closed lines precipitate in the chromosphere to cause the QPPs we observe in hard X-ray and EUV. But what causes the reconnection and particle acceleration itself to be quasi-periodic? As mentioned in the introduction, this could be due to either the process itself being time-dependent (self-oscillatory) or indeed due quasi-periodic triggering of magnetic reconnection due to external MHD waves. We can rule out the latter, as it is unlikely as there are no

active regions nearby.

Plasmoid magnetic island reconnection or oscillatory reconnection are both good candidates. Given that the period of the QPPs analysed in this work match well with the simulations in McLaughlin et al. (2012) (105-121.5 s), this mechanism may be responsible. McLaughlin et al. (2012) outline how the interaction of magnetic flux emerging from the tachocline with an existing magnetic topology such as a flaring system can result in oscillatory reconnection and pulsed particle acceleration. It is possible that this flux emergence is localised to the region of the flare site we identified as the QPP source. This could then give rise to the QPPs we observe across the electromagnetic spectrum. However we are unable to rule out the possibility of plasmoid magnetic island reconnection or other self-oscillatory processes. There are a number of arguments that point towards a relation between the HXR/SXR/EUV QPPs and the radio QPPs we observe despite them having different periods according to our wavelet analysis. We outline below our argument that they are indeed a consequence of the same progenitor.

1. The emission mechanism involved that produces the radio (plasma emission) versus the mechanism producing the EUV, SXR, and HXR (non-thermal bremsstrahlung versus heating) are very different in nature - i.e incoherent free-free emission versus coherent collective emission. In the plasma emission mechanism, accelerated electron beams travel to large heights (for the frequencies we observe) along open magnetic field lines, induce the growth of Langmuir waves, and then these Langmuir waves must interact to finally produce radio emission (Melrose, 2017). Many factors, such as the electron energy (which can vary from pulse to pulse), velocity dispersion, Coulomb collisions, Langmuir wave growth and interaction, to name a few, play a role in generating the emission. It is a multi-stage process, and variability in any of these stages can change the characteristics of the radio pulses. In contrast, the electrons producing the higher energy radiation, via non-thermal bremsstrahlung and subsequent heating of the surrounding plasma, must only travel from the acceleration site within the flaring region to the chromosphere. Bremsstrahlung then occurs quickly followed by

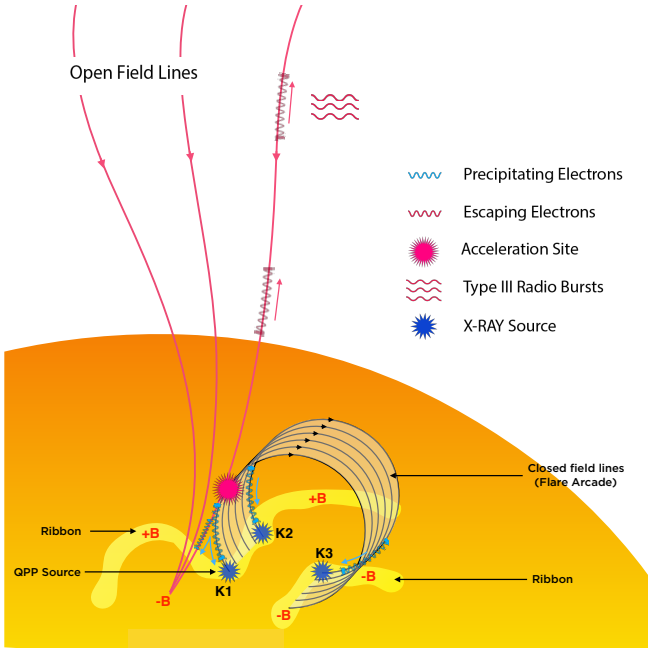

Figure 5.12: Cartoon of the flaring region illustrating the likely mechanism through which we observe the episodic particle acceleration resulting in QPPs in EUV, radio, SXR, and HXR. The QPP source footpoint is related to the open and closed field lines allowing for the escape of the electrons resulting in the radio emission and the precipitation of the electrons giving rise to the higher frequency emission.

instantaneous heating resulting in co-temporal pulsations in the EUV, SXR, and HXR wavebands (White et al., 2011). Due to these factors, it is expected that not every HXR/SXR/EUV pulsation would have a corresponding radio burst, as we observe, despite being a consequence of the same intermittent particle acceleration.

2. The region of the flare site we have identified as the QPP source is in close proximity to open and closed magnetic field lines. This magnetic field geometry allows for reconnection to occur between the open and closed field lines, providing a natural route for the escaping electrons to produce the radio emission and the precipitating electrons to produce the X-rays/EUV as shown in Figure 5.11.

3. The time delay between the HXR emission and the onset of the prominent type III radio bursts is consistent with the estimated distance over which the radio electron beam sources must travel before they emit at 2.5 MHz, as shown in Figure 5.3. This source height of $\sim$16 $R_{\odot}$ was obtained by the Newkirk Jr. (1967) electron density model.

4. The wavelet analysis of the 2.5 MHz light curve only picks up the four main

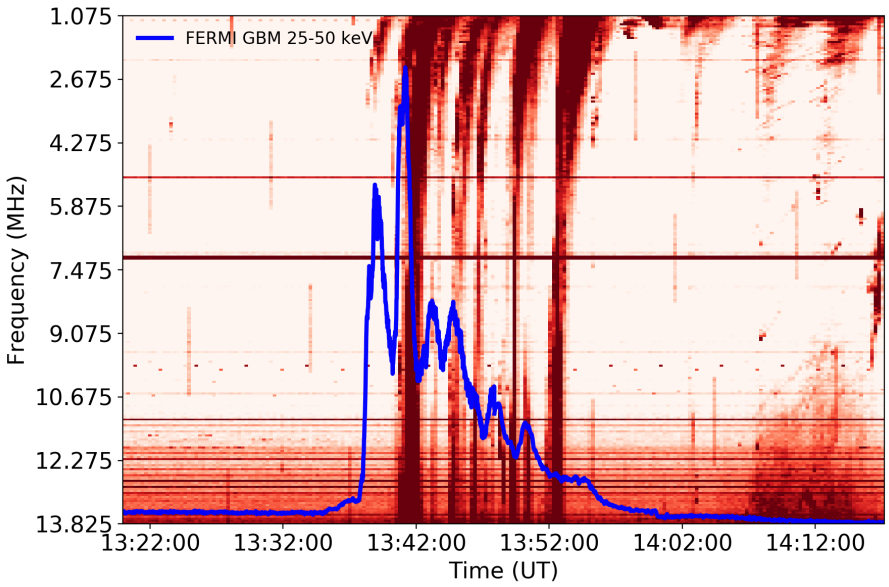

Figure 5.13: The HXR emission from FERMI GBM (25-50 KeV) overplotted against the dynamic spectrum from WIND/WAVES showing the low frequency radio emission in the form of a sequence of type III radio bursts.

peaks in the time series. Smaller amplitude peaks fail to contribute significantly to the result. In Figure 5.8 we manually find the period by identifying the four most prominent peaks, which matches the result of the wavelet analysis. However when the smaller amplitude peaks are accounted for, amounting to a total of 7 pulses, the period of the radio emission comes within error of the period of the HXR/SXR/EUV. An additional difficulty in accurately calculating the period of the radio emission is that certain bursts are more intense at different frequencies as is clear in the dynamic spectra. However, from inspecting Figure 5.13 where the HXR emission is overplotted on the dynamic spectrum, there is quite a clear relation between the radio bursts and the HXR peaks when the entire frequency band is taken into account.

Cairns et al. (2020) point out that a type II radio burst occurs at the time of this flare and suggest that the associated shock may be responsible for accelerating the electrons that result in the low frequency radio emission. However, considering the arguments above (points 1-4), we conclude that it is more likely that the type III radio bursts are due to pulses of electron beams accelerating along the open magnetic lines close to the QPP source region. Additionally, the dynamic spectra of the radio emission from kHz to GHz shows traces of type III bursts that extend to high frequencies, above

the frequency of the type II burst (see Cairns et al. (2020) Figure 15). This suggests that they originate from a region closer to the flare site.

In summary, A multi-wavelength analysis of QPPs in an M-class flare has been conducted. Several instruments were used to allow for the analysis of the HXR, SXR, EUV, and radio emission detected during the event. The 171 Å, 1600 Å, SXR, and HXR light curves yielded similar periods of 122^{+26}_{-22} s, 131^{+36}_{-27} s, 123^{+11}_{-26} s, and 137^{+49}_{-56} s, respectively, indicating a common underlying mechanism, while the radio emission at 2.5 MHz contained a longer period of ∼231 s. X-ray and EUV imaging enabled us to localise the QPP source to a region of the flare site associated with open magnetic field lines. We found that the time delay between the X-ray/EUV emission and the radio emission is consistent with the estimated distance over which the electron beam sources must travel. We discuss the differences between the emission mechanisms responsible for the HXR/SXR/EUV emission versus the radio emission and determine that the QPPs in each waveband are linked to the same populations of accelerated electrons. We conclude that the QPPs in this event are due to some time-dependent self-oscillatory reconnection mechanism. Magnetic reconnection occurring in this bursty fashion injects populations of non-thermal electrons into the flare site giving rise to the sequence of pulses we observe in the SXR, HXR, and EUV as electrons collide with the chromosphere while the electrons accelerating away from the flare site along open magnetic field lines produce the type III radio bursts. This work provides new evidence that oscillatory reconnection can naturally generate quasi-periodic periodic pulsations providing an explanation for their presence across the entire spatial range of flaring emission. This work also shines light onto the nature of energy release in flares and provides new insight into how QPPs may be localised to specific regions within flare sites. Future work that investigates the details and conditions required for the triggering of magnetic reconnection in this bursty fashion is needed. This work was published in *The Astrophysical Journal* (Clarke et al., 2021).

6

X-ray and Radio Diagnostics of Accelerated Electrons Using STIX

Building on from the themes of Chapter 5, here work is presented that further investigates the relationship between HXR emission and radio emission using cutting edge, state-of-the-art instrumentation. The Spectrometer Telescope for Imaging X-rays (STIX) is one of ten instruments that was launched in February 2020 onboard Solar Orbiter (see Section 3 for instrument details). Using STIX in combination with other radio instruments provides unique observational capabilities in furthering our understanding of high energy electrons accelerated during solar flares. In this chapter, software that was developed as part of the *STIXpy* visualisation package, and its application for this work, is presented. The software reprojects image maps from other instruments to the perspective of STIX, or any general observer, and also provides a tool for generating summary plots of radio spectrograms alongside STIX and GOES time-series data. This software helps to facilitate multi-instrumental analysis involving STIX.

In addition to the software, preliminary analysis is discussed that attempts to identify a relationship between X-ray spectra and the velocity of the electron beams involved in the generation of type III radio bursts. This work has been done in collaboration with Dr. Shane Maloney and by Mr. Thomas Long.

6.1 Software Development

The work presented in Chapter 5, illustrates the importance of investigating solar phenomena, such as QPPs, from a multi-wavelength perspective. In Figure 5.3, data from WIND/WAVES, SDO/AIA, GOES, and FERMI GBM together form a rich picture of the scenario at play by incorporating the low frequency radio components of the flare emission through to the high energy X-ray counterparts of the event. Additionally, RHESSI was used to image the X-ray sources associated with that event.

Although it well established that using multiple instruments helps us to build up the best complimentary data to aid us in understanding interesting events, it can often be cumbersome and time-consuming to manually download, process and analyse the many data sets appropriately. In this section, software, and its utility, is presented that aims to facilitate convenient quick-look analysis of multi-instrumental data involving STIX. These tools will form part of *STIXpy*, a python based analysis software for STIX data that will be part of *SunPy* (The SunPy Community et al., 2020). Applications of these tools are then presented with a focus on the signatures of accelerated electrons in X-ray and radio data.

6.1.1 Map Reprojection Tool

Different spacecraft observe the Sun from different perspectives depending on their positions in space. This can be a useful effect in order to gain different perspectives of various types of solar activity. However, understanding the viewpoints instruments have with respect to one another is crucial in order to carry out multi-instrumental imaging and spectral analysis correctly. This tool enables users to input an image map from an arbitary instrument, such as AIA onboard SDO, and reproject the map so that it appears as if it were viewed from the perspective of STIX. This works by extracting the observation time from the input map and using this information to find the position of Solar Orbiter at that time. The coordinate frames of STIX and the input map observer are then set, before a new header containing the position information is

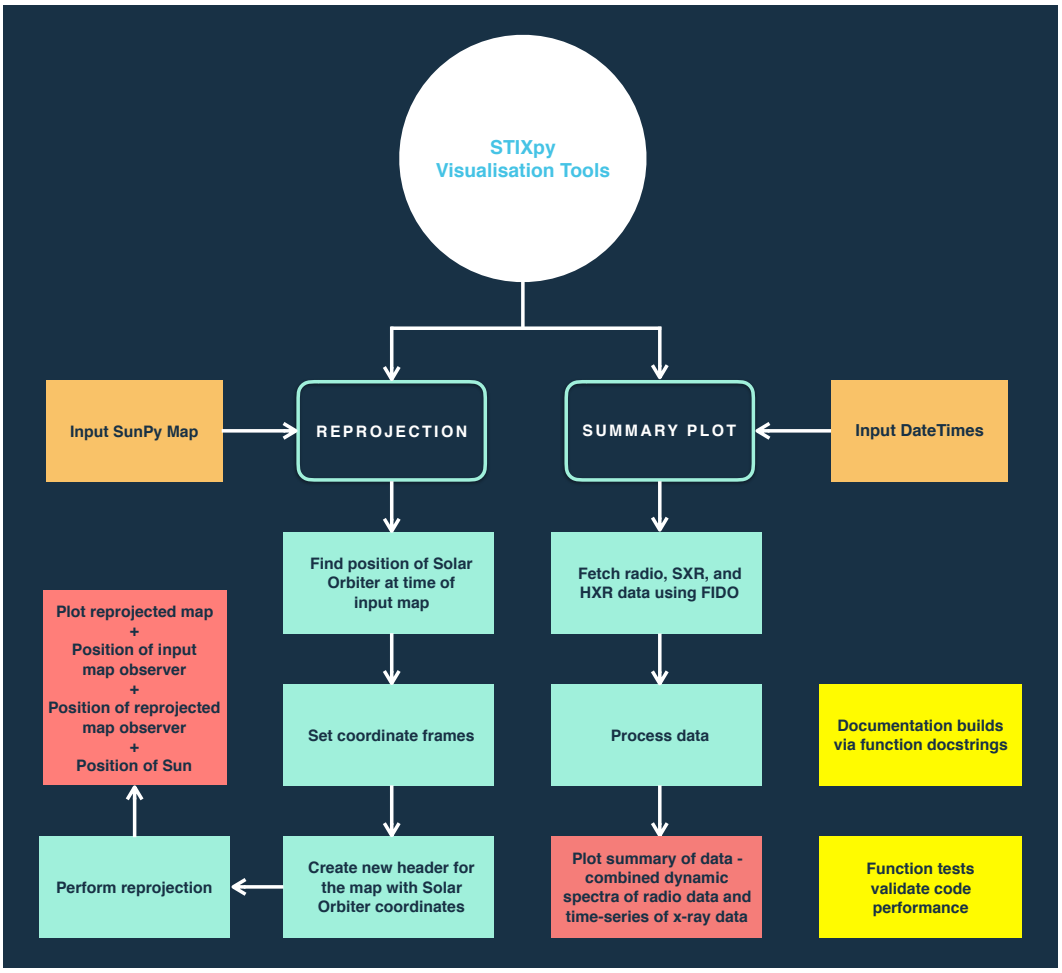

Figure 6.1: Flowchart of the map reprojection and summary plot software tools developed for STIXpy.

generated for the reprojected map. The reprojection is then performed and the new header is used to generate a SunPy map object containing the reprojected image. The tool then plots the original map, the reprojected map, and the observer locations in polar coordinates. The position of the Sun is also plotted. The left side of Figure 6.1 summarises this process in a flowchart.

The reprojection process itself is performed using an interpolation algorithm. This is an efficient method suitable to most cases, however, it is important to note that it does not conserve flux. The order of the interpolation can be controlled by setting the method to 'nearest neighbour', 'bilinear', 'biquadratic', or 'bicubic'. Full documentation of the interpolation algorithm used is provided at *https://reproject.readthedocs.io/*.

An example of the output of this software for the case in which the input map is an 193 Å AIA map is shown in Figure 6.2. From inspecting the polar positions of the

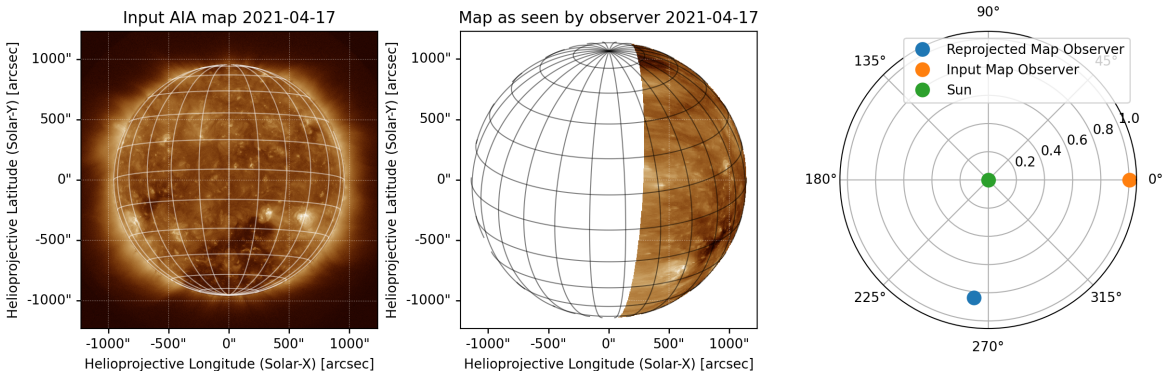

Figure 6.2: Output of map reprojection software developed for STIXpy visualisation package as part of SunPy.

observers on the right side of the Figure, Solar Orbiter (blue dot) has a perspective from which it can only see a portion of the eastern hemisphere of the solar disk. This is reflected in the central panel of the Figure containing the reprojected map. An example of a convenient application of this tool would be quickly determining the active regions visible to both STIX and AIA at some observation time. It also allows for the possibility of overplotting STIX images on to other maps (e.g AIA or HMI maps).

6.1.2 Summary Plot Tool

The right side of Figure 6.1 provides a flowchart of the second software tool developed as part of this work. The tool takes datetimes (start and end) as the inputs and proceeds to fetch radio data and X-ray data using the FIDO facility of SunPy. Initially, STEREO/WAVES data was used to cover the low frequency radio waveband, GOES was used for the SXR regime, and STIX was used to cover the 4.0 - 84 keV energy X-rays. The software then processes the data in various ways. This includes concatenating the time-series when appropriate, preparing the radio data to be plotted as a cleaned spectrogram with the correct normalisation and axes, and producing legends and labels etc. An example of the output of this tool for a time range of 04:00:00-23:00:00 on 2020-11-20 is shown in Figure 6.3. In this example, a number of Type III radio bursts are visible in the STEREO/WAVES spectrogram that have associated SXR counterparts in the GOES data. Two STIX flares are also clearly visible in the softer channels during time of radio activity indicating likely related populations of accelerated electrons.

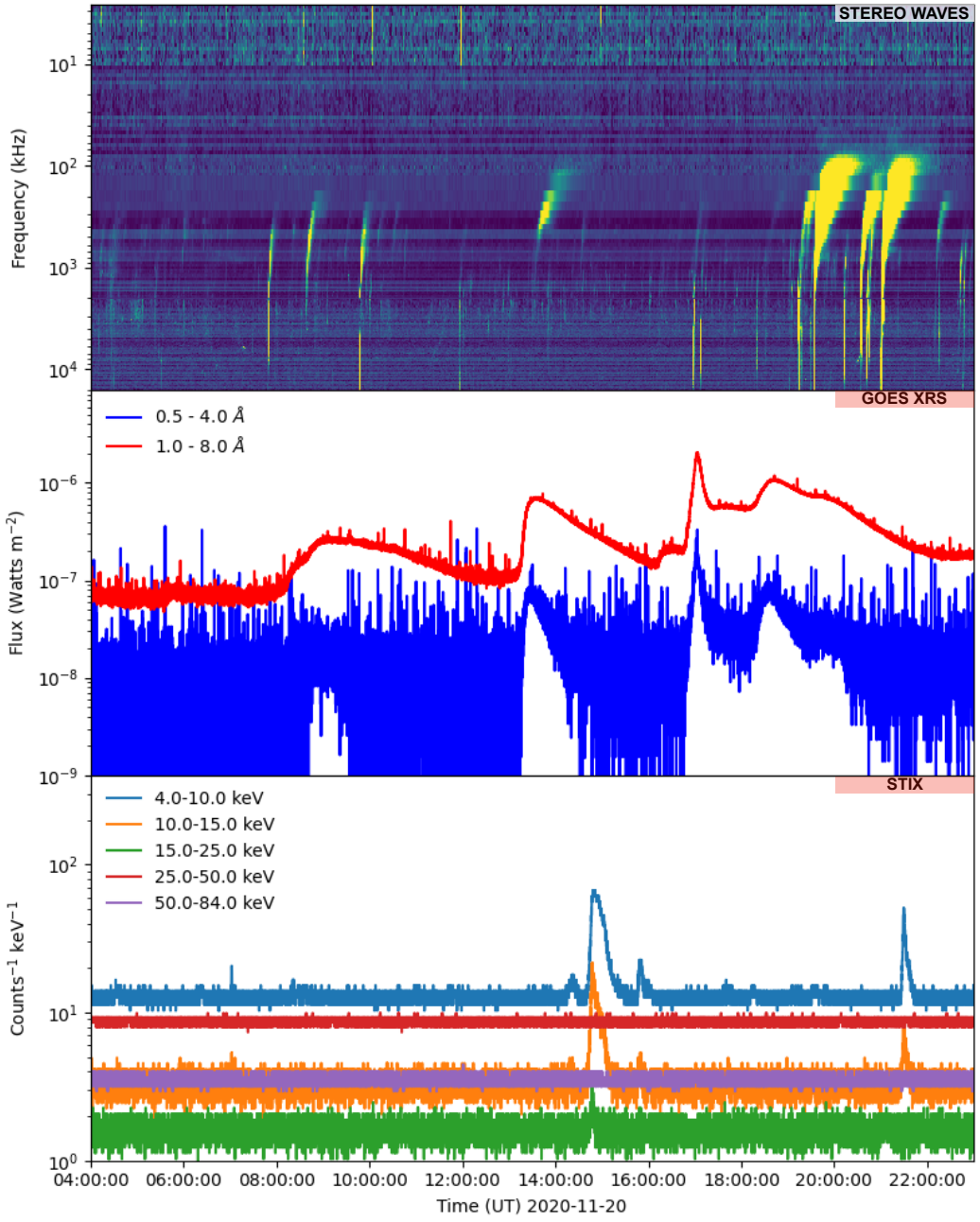

Figure 6.3: Automated summary plot of X-ray and radio observations. This iteration of the tool produces plots using STEREO/WAVES data, GOES data, and STIX data.

This tool was then developed further to incorporate higher cadence radio instrumentation. The publicly available STEREO/WAVES data has a time resolution of 60 s. This restricts our ability to analyse the fine structure of radio bursts in detail. Matching the radio time resolution with the high time cadence of STIX (0.1-1s) provides a much better facility for comparing the two emission bands. To do this, data from our own national radio interferometer, I-LOFAR, was added to the software

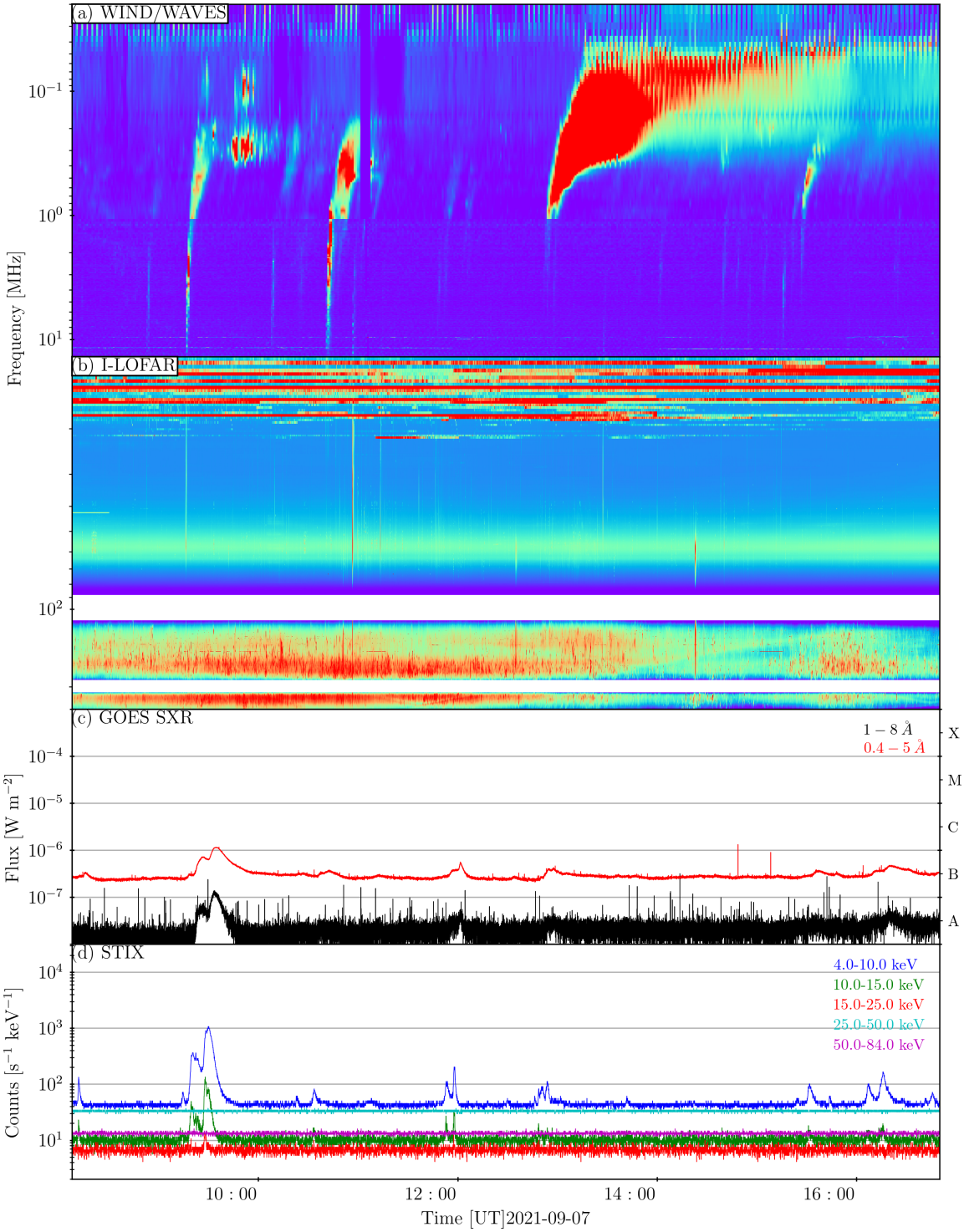

Figure 6.4: Automated summary plot of X-ray and radio observations. This iteration of the tool produces plots using higher cadence radio instrumentation. I-LOFAR data, WIND/WAVES data, GOES data, and STIX data comprise the summary plot.

pipeline. WIND/WAVES data was also added to cover the very low frequency (20 kHz - 13.825 MHz) emission. Figure 6.4 shows an example of the output of this newer version of the summary plot tool. Here, one can clearly note time correlated flares in

the STIX and GOES data as well as associated type III radio bursts in the I-LOFAR and WIND/WAVES data. This tool facilitates users to quickly inspect radio and X-ray data of interest for specific time ranges.

6.2 X-ray & Radio Producing Electrons

6.2.1 Introduction

In Chapter 5, evidence was presented that related HXR quasi-periodic pulsations (QPPs), to QPPs seen in the SXR, EUV and decimetric radio wavebands. It was concluded that bursty magnetic reconnection likely was producing pulsed electron acceleration at the energy release site of the flare. The electrons precipitating down towards the chromosphere produced the HXR QPPs, while the electrons escaping towards interplanetary space resulted in a sequence of type III radio bursts. Here, preliminary analysis is presented that attempts to strengthen the aforementioned argument that radio and X-ray producing electrons can share the same source of energy release and that they can originate from the same population of accelerated electrons.

Figure 2.7 shows a typical HXR spectrum observed during a solar flare. It consists of an exponential thermal component and a power–law nonthermal component. It is during the impulsive phase of the flare when the non-thermal component dominates the emission. This period of the flare is most associated with particle acceleration. The spectral index of the power law fitted to the non-thermal component provides information about the electron acceleration efficiency. Low value spectral indices, indicating a flat fit, are referred to as *hard* distributions. These hard distributions point towards a slow fall off of high energy X-rays with increasing energy. Therefore, more energetic electrons have been accelerated in cases when a hard distribution is observed. High value spectral indices, indicating a steep fit, is representative of a *soft* distribution. In this case, the number of high energy X-rays more rapidly decreases with increasing energy (da Silva & Valio, 2021).

Given flares evolve from the pre-flare phase, to the impulsive, and then to the

gradual phase, one would expect the power law spectral index to evolve as well. This indeed is the case, and is referred to as *soft-hard-soft* evolution (Parks & Winckler, 1969). The hard phase corresponds to the impulsive phase of the flare when electron acceleration is at its most efficient. Using kinetic simulations, Reid & Kontar (2018) found that the velocity of electron beams producing type III radio bursts increases with decreasing initial spectral index of the accelerated electron beams. This indicates that faster type III bursts are a consequence of higher energy electron beams. In the analysis presented below, we investigate this observationally to determine if the radio and X-ray producing electrons can be linked.

6.2.2 Observations & Data Analysis

Several events have been analysed as part of this work to date. To illustrate the analysis carried out and the type of data used so far in this study, an example event is shown. This event was an M-class flare that took place on 2021-05-23. Figure 6.5 shows a summary of the data. Panel a shows a dynamic spectrum, observed by eCALLISTO (Glasgow), containing several type III radio bursts that begin close to the time of the impulsive phase of the flare. Panels b-d show time series data from the dynamic spectrum at a number of frequencies. These data reveal the bursty and perhaps quasi periodic nature of this sequence of radio bursts. Panel e shows the SXR emission observed by GOES. Also plotted is the derivative of the 1.0-8.0 Å channel which appears to roughly correspond to the radio time-series data. Given the Neupert effect relates the SXR derivative to the HXR emission, this may be indicative of impulsive heating and particle acceleration. Panel f shows the STIX time series data for the event. The vertical dashed line shows the time that was used to generate the X-ray spectrum. Care was taken to ensure this time was during the impulsive phase of the flare when the non-thermal component of the emission dominates.

Figure 6.6 shows this X-ray spectrum fitted to a power law. The value of the spectral index this particular fit yielded was $\sim$4.41. Several similar events to this were analysed in this way in order to build up a small database of X-ray spectral indices.

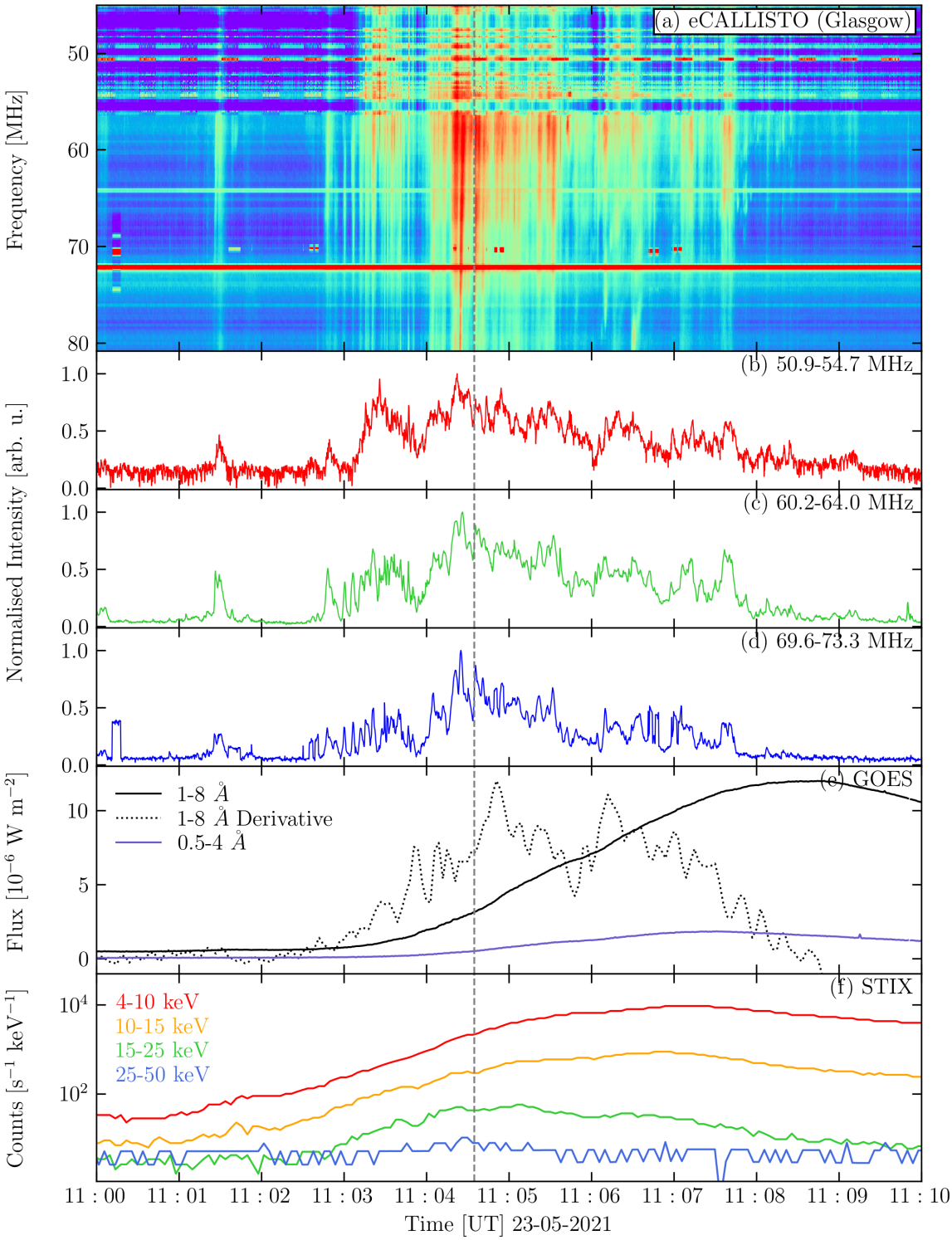

Figure 6.5: Summary of X-ray and radio observations on 2021-05-23. (a): Spectrogram from eCALLISTO containing several type rom3 radio bursts. (b)-(d): Time-series data from the eCALLISTO at several frequencies. (e): GOES XRS data. The derivative of the 1.0-8.0 Å channel is also shown. (f): STIX time-series data. The vertical dashed line shows the time at which the X-ray spectrum was made.

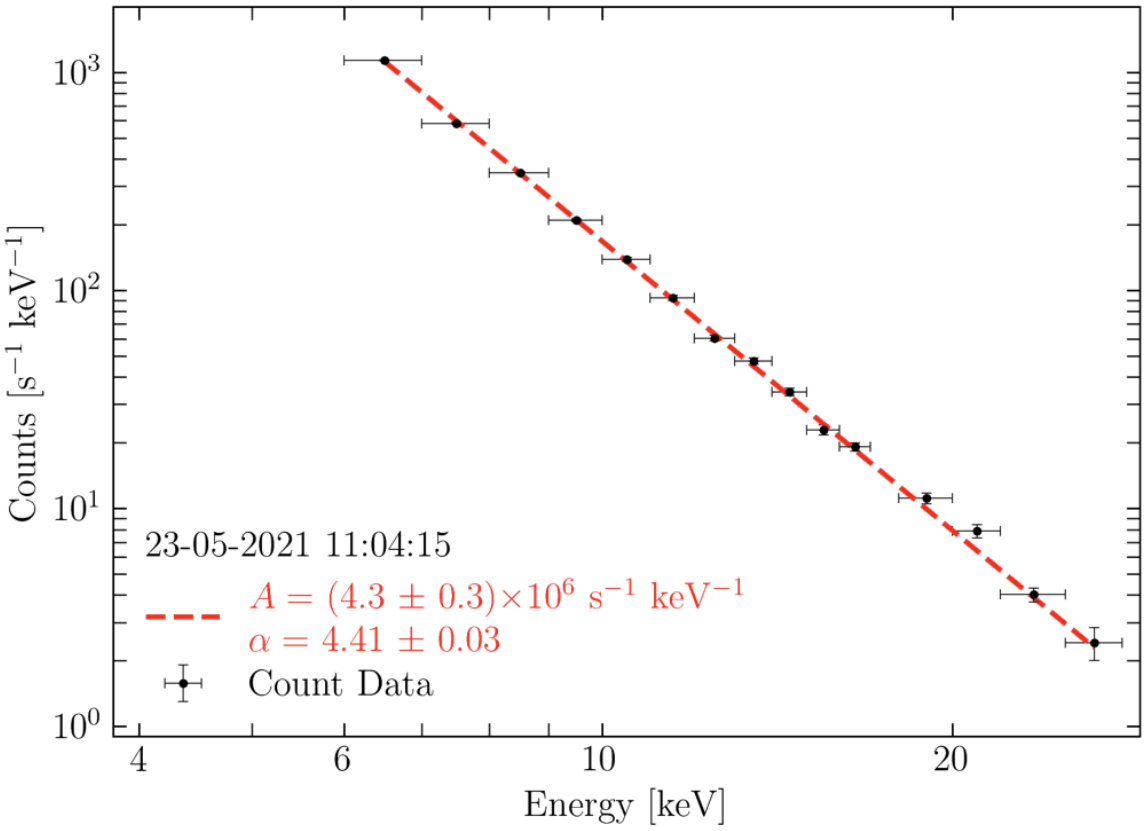

Figure 6.6: X-ray spectrum of flare that occurred on 2021-05-23.

The velocities of the approximately co-temproal type III bursts contained in each event were then estimated via their drift rates. This was achieved using a variety of electron density models (Mann et al., 1999; Newkirk Jr., 1961; Saito et al., 1977) to convert frequency information to height information (as outlined in Section 2.6.1) at the start and end of each burst.

6.2.3 Results & Discussion

Figure 6.7 shows a plot of the collated spectral indices for each analysed event versus their corresponding type III burst velocity. At this preliminary stage we clearly see a result which matches the modelling from Reid & Kontar (2018) - that the type III burst velocities increase with decreasing values of the spectral index. This suggests that in cases in which there is efficient electron acceleration at the energy release site of flares, faster electron beams are produced both in the direction towards the solar surface

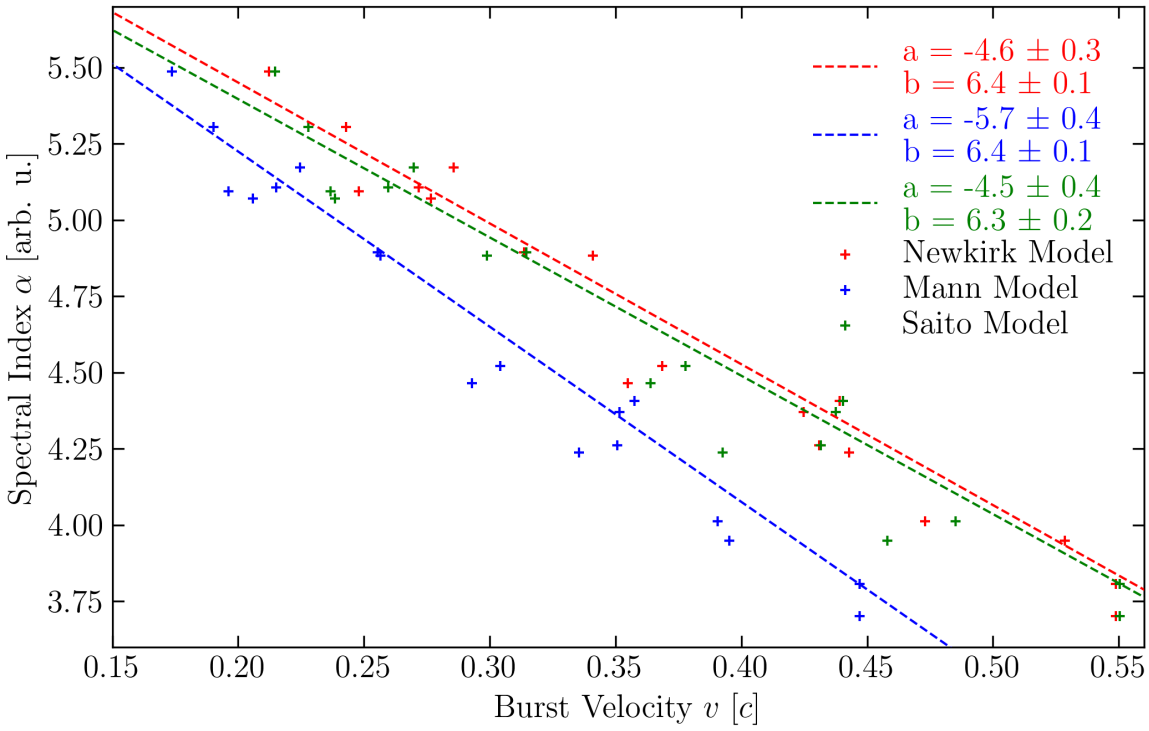

Figure 6.7: X-ray spectral index versus type III burst velocity. The results are shown for bursts speeds calculated using three distinct electron density models (Mann et al., 1999; Newkirk Jr., 1961; Saito et al., 1977) as shown.

where the X-rays manifest, and in the direction outwards towards interplanetary space where the radio bursts are produced via plasma emission.

Software currently under development for STIXpy will help to further solidify this analysis. This software will allow for the conversion of the HXR photon spectrum to the electron distribution function for each event. At this stage, it will be possible to estimate the velocity of the electrons directly and compare them against the velocities obtained from the drift rates of the type III bursts. This can be achieved by assuming the electron energies are primarily kinetic in nature: $E \approx E_k = 1/2mv^2$. In addition, radio imaging using I-LOFAR combined with X-ray imaging using STIX will further enable this result to be verified by tracing both types of emission back to the same region.

7

Conclusions & Future Work

The work presented in this thesis aims to further current understanding of phenomena associated with particle acceleration in solar energetic events such as flares. These energetic events are a consequence of magnetic energy being released from the Sun's atmosphere in the form of thermal and kinetic energy. In Chapter 4, an investigation into Solar S-bursts was presented. Few large scale observational studies of S-bursts have been conducted. However, here we characterise their properties and determine that they are likely generated via a variation of the plasma emission mechanism. This mechanism enables us to use the observational properties of S-bursts as a tool for remote sensing the coronal magnetic field. Due to the difficulty in determining the magnetic field strength in the corona, this result provides a useful method for doing so.

Chapter 5 investigated the phenomenon of quasi periodic pulsations in flares. These modulations of electromagnetic emission as a function of time are ubiquitous in flares. However, there is still great debate surrounding their origin. In this chapter, an M-class solar flare exhibiting pronounced, oscillatory pulsations was studied in detail. The QPPs in this study were found to be extremely broad-band, being observed at HXR wavelengths through to low energy radio wavelengths. It is shown that the source of these QPPs originate from near the energy release site of the flare and manifest across vast distances, from the flare footpoints through to interplanetary space. It is determined that the QPPs in this event are a consequence of bursty magnetic reconnection which results in quasi periodic particle acceleration. This result shines light onto the

nature of energy release in flares.

Lastly, in Chapter 6, a preliminary analysis of the relationship between HXR emission and radio emission using STIX and various radio instruments including I-LOFAR is presented. It is shown that HXR photon spectral index correlates with the beam speeds of type III burst sources. Additionally, software to further aid this investigation was developed for and added to the STIXpy visualisation package. Future investigation of this work is then outlined which aims to relate the energy of the electrons responsible for the HXR emission to the energy of the electrons that give rise to the corresponding radio emission. In this final Chapter, each of these results is reviewed in detail and potential avenues of future work are outlined.

7.1 Properties and Magnetic Origins of Solar S-bursts

In this work, the largest observational study of solar S-bursts, to date, was conducted. 3000 S-bursts were observed using LOFAR and UTR-2 in a frequency band of 18.7-83.1 MHz. All of these observations were made on 9 July 2013. Their spectral properties, including their frequency bandwidths, durations, central frequencies, drift rates, and flux values, were measured. The bursts were short in total duration and FWHM duration, ranging from $\sim$0.5-9 s and 0.02-0.6 s, respectively. Their total frequency bandwidths were found to have mode values of 1.21 ± 0.32 MHz and 2.30 ± 0.43 MHz using the UTR-2 and LOFAR data, respectively. The instantaneous bandwidths of the bursts were also measured. This property describes the frequency bandwidth of a burst during a single time of its emission, and is a proxy for the source size. The values measured for this property ranged from 0.14-2.04 MHz, agreeing with previous results (Dorovskyy et al., 2017; McConnell, 1982; Morosan et al., 2015).

The instantaneous bandwidths and central frequencies of the bursts were found to be linearly related, indicating that S-burst source sizes tend to increase with increasing central frequency. The slope of the linear fit was found to be 0.022 and the intercept

was -0.22. This result confirmed the original report of this correlation given by Melnik et al. (2010). A functional dependence between the frequency and drift rate of the S-bursts was observed using data from all 3000 observations. This dependence was represented by a power law of the form $df/dt = -af^b$, where a was found to be 0.0084 and b was found to be 1.57. These fit parameters agree well with Dorovskyy et al. (2017), McConnell (1982), and Morosan & Gallagher (2018). This confirms that S-bursts sources have faster velocities with increasing central frequency. The flux of the S-bursts, as well as co-observed type III and type IIIb radio bursts were were measured and compared. No dependence of flux on frequency or flux on FWHM duration was observed. A number of electron density models were used to estimate the heights at which the S-bursts are generated. These source heights were found to range from $\sim 1.3 - 3\ R_\odot$. The source electron velocities of the S-bursts were also measured and found to be $\sim$0.07 c.

The leading theories of how S-bursts are generated was then investigated. These included the models proposed by Melnik et al. (2010) and Zaitsev & Zlotnik (1986). It was shown that the Zaitsev & Zlotnik (1986) model could not account for the observations made as part of this study. However, it was found that the Melnik et al. (2010) model can account for the observed spectral properties of S-bursts. Using the Melnik et al. (2010) model, the magnetic field strengths at the source heights of S-bursts was estimated and were found to range from 0.9-5.8 G. These magnetic field values agree with observations and coronal magnetic field models indicating the Melnik et al. (2010) model can enable us to conduct remote sensing of the coronal magnetic field. This work was published in *Astronomy & Astrophysics* (Clarke et al., 2019).

7.1.1 Future comparisons of coronal magnetic field strengths

To further test the Melnik et al. (2010) model, it is possible to compare the coronal magnetic field strengths it predicts in the solar atmosphere against other techniques. S-bursts typically appear against the background of other types of solar radio activity. Type II radio bursts (see schematic of radio bursts in Figure 1.16) are such an example

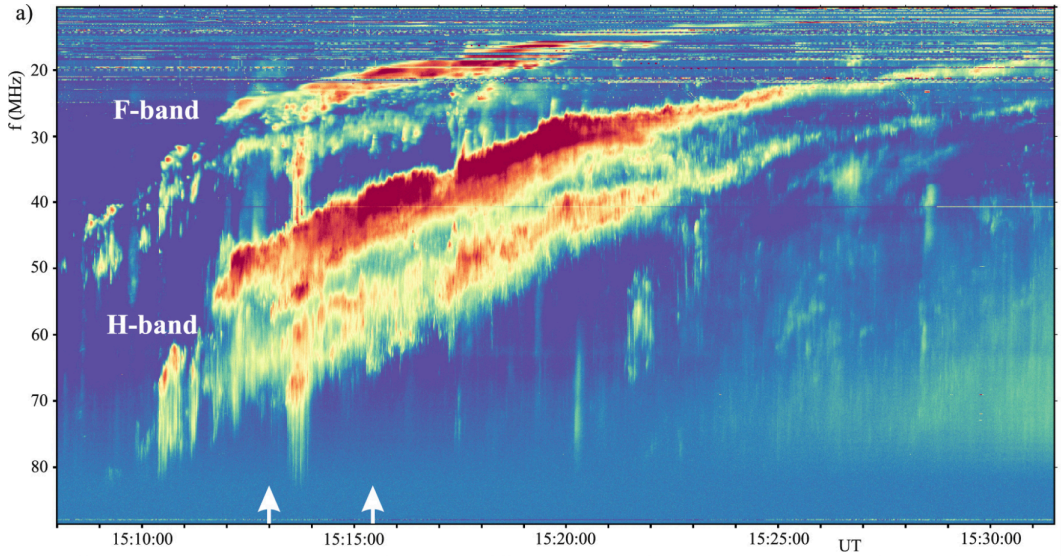

Figure 7.1: Type II burst observed by LOFAR. Shown are the fundamental are harmonic Taken from Magdalenić et al. (2020)

of radio emission that may be co-temporally observed with S-bursts. Type II bursts are indicative of shock propagation in the corona. On a dynamic spectrum, they appear as slowly drifting emission bands.

Figure 7.1 shows the fundamental and harmonic emission of a type II burst observed with the high frequnecy and time resolution capabilities of LOFAR (Magdalenić et al., 2020). A splitting of the bands is visible in both the fundamental and harmonic emission. It is believed that this band-splitting may be a consequence of plasma emission occurring in the upstream and downstream shock regions (Vršnak et al., 2002). Adopting the upstream/downstream interpretation allows for the inference of the coronal magnetic field strength via the measured amount of band-splitting, Δf (Smerd et al., 1974). Searching for examples of band-split type II for which S-bursts are co-observed would provide opportunity to compare the inferred magnetic field strengths which should be in agreement.

7.2 Quasi-periodic Particle Acceleration in a Solar Flare

Chapter 5 presented a study of QPPs in an M-class flare. Multiple instruments including RHESSI, FERMI GBM, GOES, SDO/AIA, and WIND/WAVES were used analyse the HXR, SXR, EUV, and radio emission detected during the event. This provided a broad-band, multi-wavelength perspective on the QPPs. QPPs were found to be occurring in each of the different wavebands and in each case, their periods were measured. The 171 Å, 1600 Å, SXR, and HXR light curves had similar periods of 122^{+26}_{-22} s, 131^{+36}_{-27} s, 123^{+11}_{-26} s, and 137^{+49}_{-56} s, respectively. This indicates a common underlying mechanism is responsible for the QPPs occurring at these different energies. The low frequency radio emission at 2.5 MHz contained a longer period of $\sim$231 s.

X-ray and EUV imaging enabled us to locate the QPP source. This location of the flare site was found to be associated with open magnetic field lines that were revealed by a PFSS extrapolation. The time delay between the X-ray/EUV emission and the radio emission was then measured. This delay was found to be consistent with the estimated distance over which the electron beam sources travelled between the energy release site and the source region of the radio emission. The differences between the emission mechanisms responsible for the HXR/SXR/EUV emission versus the radio emission, responsible for the different observed periods, were then discussed in detail. It was determined that the QPPs in each observed waveband are linked to the same populations of accelerated electrons. We then concluded that the QPPs in this investigated event are due to some time-dependent self-oscillatory reconnection mechanism. Magnetic reconnection occurring in this bursty fashion injects populations of non-thermal electrons into the flare site giving rise to the sequence of pulses we observe in the SXR, HXR, and EUV as electrons collide with the chromosphere while the electrons accelerating away from the flare site along open magnetic field lines produce the type III radio bursts.

These results provide new evidence that oscillatory reconnection can result in QPPs.

This mechanism explains their presence across the entire spatial range of flaring emission and shines light onto the nature of energy release in flares. Additionally, we show that QPPs may be localised to specific regions within flare sites. This work was published in *The Astrophysical Journal* (Clarke et al., 2021).

7.2.1 Statistical Studies of QPPs and Categorisation of Mechanisms

While detailed case studies are essential to understand the physical processes that occur in flares exhibiting QPPs, statistical studies are required for us to categorise the prevalence of different types of QPP emission mechanisms. One challenge in this field is disentangling the many mechanisms through which QPPs are theorised to occur. To date, at least fifteen physical mechanisms / models have been proposed to explain QPPs in solar flares (Zimovets et al., 2021). What proportion of QPPs observed in flares are due to oscillatory reconnection and how does this compare to the proportion of flares exhibiting QPPs by other means? Do these different mechanisms have characteristic time scales and if so do can they be related to length scales of the flare site? Statistical analysis of the many QPP case studies reported in the literature will provide insight that may help to answer these questions.

7.2.2 HXR Imaging of QPP Sources

An interesting avenue of inquiry that was unable to be carried out in the QPP study presented in this thesis, is to use high time resolution HXR imaging of the QPP source region. Using AIA, it was possible to localise the QPP source to a region associated with open magnetic field lines. However, X-ray imaging would enable us to determine if there HXR footpoint motions of the source, or if the source changes in its morphology as a function of time. For example, will the HXR source size modulate temporally with a time-scale that matches the QPP period? If there are footpoint motions of the source, do they relate to some properties of the flare site, or are they random? Future work using STIX will allow us to answer these questions and determine further details

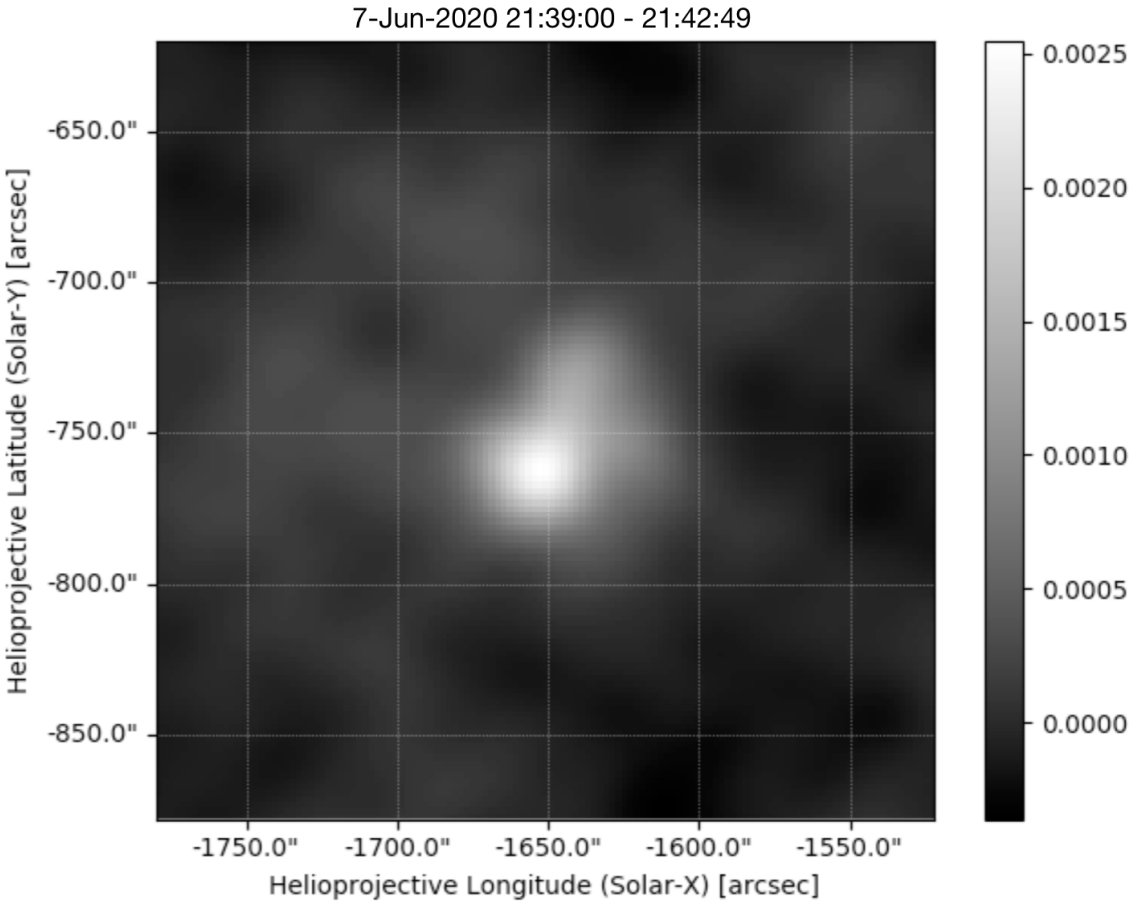

Figure 7.2: Test X-ray image made using STIX with software that is currently under development. The image shows an active region observed 7-06-2020. The energy range of the image is 6-10 keV with an integration time of *

surrounding the nature of QPPs produced via oscillatory reconnection. The STIX imaging software is currently under development. Figure 7.2 shows a test image of an active region observed 7-06-2020 that was constructed using the CLEAN algorithm over an energy range of 6-10 keV.

7.3 X-ray and Radio Diagnostics of Accelerated Electrons Using STIX

Chapter 6 presents preliminary analysis that investigates the relationship between radio and X-ray producing electrons. To carry out this work, software was developed that enables users to produce summary plots of radio and X-ray data. This summary plot tool takes datetimes (start and end) as the inputs and proceeds to fetch radio data

and X-ray data using the FIDO facility of SunPy. It then processes and plots X-ray time-series data alongside radio dynamic spectra. Using this tool, events exhibiting impulsive X-ray emission with associated type III radio bursts were identified. A small database of X-ray spectral indices was then collected for these events. It was ensured that the time at which each spectrum was analysed was during the impulsive phase of the flare when the non-thermal component of the emission dominates.

The velocity of the co-observed type III radio bursts was also measured for each identified event. The collated spectral indices for each analysed event versus their corresponding type III burst velocity was then plotted. It was found that the type III burst velocities increase with decreasing values of the spectral index. This suggests that in cases in which there is efficient electron acceleration at the energy release site of flares, faster electron beams are produced. This preliminary result agrees well with the modelling of Reid & Kontar (2018). Additionally, software was developed that enables users to input an image map from an arbitary instrument, such as AIA onboard SDO, and reproject the map so that it appears as if it were viewed from the perspective of STIX. This tool will facilitate future work involving imaging by allowing for the possibility of overplotting STIX images on to other maps (e.g AIA or HMI maps).

To expand upon the work presented in Chapter 6, more data will be collected to ensure the validity of the observed correlation between the X-ray spectral indices and source velocities of the type III bursts. Software currently under development will be used to convert the HXR photon spectrum to the electron distribution function for each event. This will then be used to directly compare the velocities of the type III bursts with the velocity of the electrons producing the X-ray emission.

The research presented in this thesis has examined a range of solar magnetic phenomena associated with particle acceleration. It has improved our understanding of the nature of low frequency radio bursts, quasi-periodic pulsations in flares, and the relationship between X-ray and radio signatures of accelerated electrons.

References

Allen, C. W. 1947, *Monthly Notices of the Royal Astronomical Society*, 107, 386 22

Anfinogentov, S. A., Nakariakov, V. M., & Nisticò, G. 2015, Astronomy Astrophysics, 583, A136 36, 66

Antiochos, S. K. & Sturrock, P. A. 1978, *Astrophysical Journal*, 220, 1137 25

Aschwanden, M. J. 2004, Physics of the Solar Corona. An Introduction 53

Aschwanden, M. J. 2005, Physics of the Solar Corona. An Introduction with Problems and Solutions (2nd edition) 12, 13, 18, 62, 63, 87, 96, 97

Aschwanden, M. J. & Benz, A. O. 1997, The Astrophysical Journal, 480, 825 25

Aschwanden, M. J., Benz, A. O., & Montello, M. L. 1994, *Astrophysical Journal*, 431, 432 34

Aschwanden, M. J., Benz, A. O., & Schwartz, R. A. 1993, *Astrophysical Journal*, 417, 790 35

Babcock, H. W. 1961, *Astrophysical Journal*, 133, 572 10

Bastian, T. S., Benz, A. O., & Gary, D. E. 1998, Annual Review of Astronomy and Astrophysics, 36, 131 57

Basu, S., Chaplin, W. J., Elsworth, Y., New, R., & Serenelli, A. M. 2009, *Astrophysical Journal*, 699, 1403 5

Bengston, C. & McCuistion, D. 1996, in Society of Photo-Optical Instrumentation Engineers (SPIE) Conference Series, Vol. 2812, GOES-8 and Beyond, ed. E. R. Washwell, 40–47 24

Benz, A. A. O. A., Csillaghy, A., & Aschwanden, M. J. J. 1996, Astronomy & Astrophysics, 309, 291 28

Benz, A. O. A., Jaeggi, M., Zlobec, P., & Jaeggi, M. 1982, Astronomy & Astrophysics, 109, 305 28

Bougeret, J.-L., Goetz, K., Kaiser, M., et al. 2008, Space Science Reviews, 136, 487 83, 102

Brown, J. C. 1971, *Solar Physics*, 18, 489 25, 61, 62, 63, 114

Brown, M. R., Cothran, C. D., Landreman, M., Schlossberg, D., & Matthaeus, W. H. 2002, *Astrophysical Journal Letters*, 577, L63 52

Browning, P. K., Gerrard, C., Hood, A. W., Kevis, R., & Van der Linden, R. A. M. 2008, Astronomy and Astrophysics, 485, 837 19

Cairns, I. H., Kozarev, K. A., Nitta, N. V., et al. 2020, *Solar Physics*, 295, 32 121, 122

Carley, E. P., Hayes, L. A., Murray, S. A., et al. 2019, Nature Communications, 10, 2276 34, 36, 66

Carmichael, H. 1964, A Process for Flares, Vol. 50, 451 25

Charbonneau, P. 2010, Living Reviews in Solar Physics, 7, 3 10

Christensen-Dalsgaard, J., Dappen, W., Ajukov, S. V., et al. 1996, Science, 272, 1286 5, 6, 8

Clarke, B. P., Hayes, L. A., Gallagher, P. T., Maloney, S. A., & Carley, E. P. 2021, *Astrophysical Journal*, 910, 123 122, 140

Clarke, B. P., Morosan, D. E., Gallagher, P. T., et al. 2019, *Astronomy & Astrophysics*, 622, A204 100, 137

Culhane, J. L., Phillips, A. T., Inda-Koide, M., et al. 1994, *Solar Physics*, 153, 307 25

da Silva, D. F. & Valio, A. 2021, *Astrophysical Journal Letters*, 915, L1 37, 129

Davis, R., Harmer, D. S., & Hoffman, K. C. 1968, , 20, 1205 5, 7

De Moortel, I., Ireland, J., Walsh, R. W., & Hood, A. W. 2002, *Solar Physics*, 209, 61 106

Dennis, B. R., Tolbert, A. K., Inglis, A., et al. 2017, The Astrophysical Journal, 836, 84 34

Dolla, L., Marqué, C., Seaton, D. B., et al. 2012, *Astrophysical Journal Letters*, 749, L16 34

Dominique, M., Zhukov, A. N., Dolla, L., Inglis, A., & Lapenta, G. 2018, *Solar Physics*, 293, 61 34

Dorovskyy, V., Melnik, V., Konovalenko, A., et al. 2017, Austrian Academy of Sciences Press, Vienna, 369 30, 91, 92, 99, 136, 137

Drake, J. F., Swisdak, M., Che, H., & Shay, M. A. 2006, *Nature*, 443, 553 66

Dulk, G. A. 1985, Annual Review of Astronomy and Astrophysics, 23, 169 32

Dulk, G. A. & Dennis, B. R. 1982, *Astrophysical Journal*, 260, 875 38

Elgaroy, O. & Sveen, O. P. 1979, Nature, 278, 626 28

Ellis, G. R. A. 1969, Australian Journal of Physics, 22, 177 29, 30

Fludra, A., Del Zanna, G., Alexander, D., et al. 1999, Journal of Geophysics research, 104, 9709 60

Foukal, P. V. 2004, Solar Astrophysics, 2nd, Revised Edition (Wiley) 5

Gallagher, P. T. T., Mathioudakis, M., Keenan, F. P. P., Phillips, K. J. H. J. H., & Tsinganos, K. 1999, Astrophysical Journal, 524, L133 60

Gary, D. E. 2012, lecture notes distributed for radio astronomy graduate Course - Phys 728 (New Jersey Institute of Technology) 16, 61

Gary, D. E. & Hurford, G. J. 1989, Washington DC American Geophysical Union Geophysical Monograph Series, 54, 237 28

Gary, G. A. 2001, *Solar Physics*, 203, 71 49

Ginzburg, V. & Zhelesniakov, V. 1958, Soviet_Astronomy 57

Glesener, L., Krucker, S., Christe, S., et al. 2016, in Society of Photo-Optical Instrumentation Engineers (SPIE) Conference Series, Vol. 9905, Space Telescopes and Instrumentation 2016: Ultraviolet to Gamma Ray, ed. J.-W. A. den Herder, T. Takahashi, & M. Bautz, 99050E 70

Guidoni, S. E., DeVore, C. R., Karpen, J. T., & Lynch, B. J. 2016, *Astrophysical Journal*, 820, 60 66

Haarlem, M. P. V., Wise, M. W. W., Gunst, A. W. W., et al. 2013, Astronomy & Astrophysics, 556, A2 82

Hayes, L. A., Gallagher, P. T., Dennis, B. R., et al. 2019, *Astrophysical Journal*, 875, 33 34

Hayes, L. A., Gallagher, P. T., Dennis, B. R., et al. 2016, The Astrophysical Journal, 827, L30 34

Hayes, L. A., Inglis, A. R., Christe, S., Dennis, B., & Gallagher, P. T. 2020a, *Astrophysical Journal*, 895, 50 35, 36

Hayes, L. A., Inglis, A. R., Christe, S., Dennis, B., & Gallagher, P. T. 2020b, *Astrophysical Journal*, 895, 50 34

Hirayama, T. 1974, *Solar Physics*, 34, 323 25

Hurford, G. J., Schmahl, E. J., Schwartz, R. A., et al. 2002, Solar Physics, 210, 61 70, 71, 72, 73, 74

Hurford, G. J., Schmahl, E. J., Schwartz, R. A., et al. 2002, *Solar Physics*, 210, 61 107

Infeld, E. 2001, Journal of Plasma Physics, 66, 363 55

Inglis, A. R., Ireland, J., Dennis, B. R., Hayes, L., & Gallagher, P. 2016, *Astrophysical Journal*, 833, 284 34

Kane, S. R., Kai, K., Kosugi, T., et al. 1983, *Astrophysical Journal*, 271, 376 33, 34

Karlický, M., Bárta, M., Mészárosová, H., & Zlobec, P. 2005, *Astronomy & Astrophysics*, 432, 705 34

Kitchin, C. R. 2007, Astronomy Now, 21, 76 25, 26

Kivelson, M. G. & Russell, C. T. 1995, Introduction to Space Physics 45

Kliem, B., Karlický, M., & Benz, A. O. 2000, *Astronomy & Astrophysics*, 360, 715 66

Konovalenko, A., Sodin, L., Zakharenko, V., et al. 2016, Experimental Astronomy, 42, 11 81

Kontar, E. P., Yu, S., Kuznetsov, A. A., et al. 2017, Nature Communications, 8, 1 86

Kopp, G., Lawrence, G., & Rottman, G. 2005, Solar Physics, 230, 129 23

Kopp, R. A. & Pneuman, G. W. 1976, *Solar Physics*, 50, 85 25

Krucker, S. & Battaglia, M. 2014, *Astrophysical Journal*, 780, 107 27

Krucker, S., Hurford, G. J., Grimm, O., et al. 2020, *Astronomy & Astrophysics*, 642, A15 75, 76, 77

Kumar, P., Nakariakov, V. M., & Cho, K.-S. 2016, *Astrophysical Journal*, 822, 7 35

Kumari, A., Ramesh, R., Kathiravan, C., & Wang, T. J. 2017, *Solar Physics*, 292, 161 13

Kupriyanova, E., Kolotkov, D., Nakariakov, V., & Kaufman, A. 2020, Solar-Terrestrial Physics, 6, 3 33

Kupriyanova, E. G., Kashapova, L. K., Reid, H. A. S., & Myagkova, I. N. 2016, *Solar Physics*, 291, 3427 34

Lang, K. R. 2001, The Cambridge Encyclopedia of the Sun 9, 11, 14, 15, 17, 18

Lemen, J. R., Title, A. M., Akin, D. J., et al. 2012a, *Solar Physics*, 275, 17 78, 79, 80, 102

Lemen, J. R., Title, A. M., Akin, D. J., et al. 2012b, *Solar Physics*, 275, 17 104

Li, D., Kolotkov, D. Y., Nakariakov, V. M., Lu, L., & Ning, Z. J. 2020, *Astrophysical Journal*, 888, 53 34

Li, D., Ning, Z. J., & Zhang, Q. M. 2015, The Astrophysical Journal, 807, 72 34

Lin, R. P., Dennis, B. R., Hurford, G. J., et al. 2002, *Solar Physics*, 210, 3 27, 70, 102

Litvinenko, Y. E. 1996, *Astrophysical Journal*, 462, 997 56

Magdalenić, J., Marqué, C., Fallows, R. A., et al. 2020, *Astrophysical Journal Letters*, 897, L15 138

Magdalenić, J., Vršnak, B., Zlobec, P., Hillaris, A., & Messerotti, M. 2006, The Astrophysical Journal, 642, 6 28

Mann, G., Jansen, F., MacDowall, R. J., Kaiser, M. L., & Stone, R. G. 1999, *Astronomy & Astrophysics*, 348, 614 132, 133

McConnell, D. 1982, Solar Physics, 78, 253 29, 30, 31, 89, 91, 92, 99, 136, 137

McLaughlin, J. A., De Moortel, I., Hood, A. W., & Brady, C. S. 2009, *Astronomy & Astrophysics*, 493, 227 67

McLaughlin, J. A., Nakariakov, V. M., Dominique, M., Jelínek, P., & Takasao, S. 2018, *Space Science Reviews*, 214, 45 35

McLaughlin, J. A., Verth, G., Fedun, V., & Erdélyi, R. 2012, *Astrophysical Journal*, 749, 30 67, 119

McLean, D. J. D., Dulk, G. A. G., & McLean, D. J. D. 1978, Solar Physics, 57, 279 13, 21, 22, 65, 87, 97, 98

Meegan, C., Lichti, G., Bhat, P. N., et al. 2009, *Astrophysical Journal*, 702, 791 77, 102

Melnik, V. N., Konovalenko, A. A., Rucker, H. O., et al. 2010, Solar Physics, 264, 103 30, 31, 63, 64, 65, 86, 87, 89, 90, 91, 92, 93, 94, 95, 96, 97, 98, 99, 100, 137

Melnik, V. N., Shevchuk, N. V., Konovalenko, A. A., et al. 2014, Solar Physics, 289, 1701 28

Melrose, D. B. 1982, in Solar Radio Storms, CESRA Workshop #4, ed. A. O. Benz & P. Zlobec, 182 63

Melrose, D. B. 1991, Annual Review of Astronomy and Astrophysics, 29, 31 57, 58

Melrose, D. B. 2017, Reviews of Modern Plasma Physics, 1, 5 119

Melrose, D. B., Harding, J., & Cairns, I. H. 2021, *Solar Physics*, 296, 42 57, 59

Mitalas, R. & Sills, K. R. 1992, *Astrophysical Journal*, 401, 759 8

Morosan, D. E. E., Gallagher, P. T. T., Zucca, P., et al. 2015, Astronomy & Astrophysics, 65, 1 29, 30, 31, 32, 64, 85, 86, 88, 89, 92, 99, 136

Morosan, D. E. E., Zucca, P., Bloomfield, D. S. S., & Gallagher, P. T. T. 2016, Astronomy & Astrophysics, 589, L8 65

Morosan & Gallagher. 2018, Planetary Radio Emissions VIII, Austrian Academy of Sciences Press [[arXiv]1802.10460] 91, 92, 99, 137

Murray, M. J., van Driel-Gesztelyi, L., & Baker, D. 2009, *Astronomy & Astrophysics*, 494, 329 67

Nakariakov, V. M., Foullon, C., Myagkova, I. N., & Inglis, A. R. 2009, The Astrophysical Journal, 708, L47 34

Nakariakov, V. M. & Melnikov, V. F. 2009, Space Science Reviews, 149, 119 33, 35, 36, 66, 67

Nakariakov, V. M. & Zimovets, I. V. 2011, *Astrophysical Journal Letters*, 730, L27 36, 66

Neupert, W. M. 1968a, *Astrophysical Journal Letters*, 153, L59 26, 78

Neupert, W. M. 1968b, *Astrophysical Journal Letters*, 153, L59 104

Newkirk Jr., G. 1961, The Astrophysical Journal, 133, 983 21, 22, 61, 87, 96, 97, 132, 133

Newkirk Jr., G. 1967, Annual Review of Astronomy and Astrophysics, 5, 213 87, 96, 97, 105, 108, 109, 120

Nindos, A. 2020, Frontiers in Astronomy and Space Sciences, 7, 57 57

Ning, Z., Ding, M. D., Wu, H. A., Xu, F. Y., & Meng, X. 2005, *Astronomy & Astrophysics*, 437, 691 34

Parker, E. N. 1963, *Astrophysical Journal Supplemental Series*, 8, 177 53

Parks, G. K. & Winckler, J. R. 1969, *Astrophysical Journal Letters*, 155, L117 130

Pesnell, W. D., Thompson, B. J., & Chamberlin, P. C. 2012, *Solar Physics*, 275, 3 78

Peterson, L. & Winckler, J. R. 1958, , 1, 205 37

Phillips, K. J. H. 1992, Guide to the Sun (Cambridge University Press) 4, 7

Priest, E. 2014, Magnetohydrodynamics of the Sun 14, 15, 17

Priest, E. R. & Forbes, T. G. 2002, *Astronomy & Astrophysics Review*, 10, 313 24

Reid, H. A. S. & Kontar, E. P. 2018, *Astrophysical Journal*, 867, 158 38, 39, 130, 132, 142

Reid, H. A. S. & Ratcliffe, H. 2014, Research in Astronomy and Astrophysics, 14, 773 28, 104, 108

Roudier, T., Malherbe, J. M., November, L., et al. 1997, *Astronomy & Astrophysics*, 320, 605 8, 10

Saito, K., Poland, A. I., & Munro, R. H. 1977, *Solar Physics*, 55, 121 132, 133

Scherrer, P. H., Schou, J., Bush, R. I., et al. 2012, *Solar Physics*, 275, 207 78

Schrijver, C. J. & De Rosa, M. L. 2003, Solar Physics, 212, 165 13, 20, 87, 117

Schwartz, R., Csillaghy, A., Tolbert, K., et al. 2002, Solar Physics, 210, 165 74

Simões, P. J., Hudson, H. S., & Fletcher, L. 2015, Solar Physics, 290, 3625 34

Smerd, S. F., Sheridan, K. V., & Stewart, R. T. 1974, in Coronal Disturbances, ed. G. A. Newkirk, Vol. 57, 389 138

Stansby, D., Yeates, A., & Badman, S. T. 2020, Journal of Open Source Software, 5, 2732 117

Stappers, B. W., Hessels, J. W. T., Alexov, A., et al. 2011, Astronomy & Astrophysics, 530, A80 82

Sturrock, P. A. 1968, in Structure and Development of Solar Active Regions, ed. K. O. Kiepenheuer, Vol. 35, 471 25

Sweet, P. A. 1958, in Electromagnetic Phenomena in Cosmical Physics, ed. B. Lehnert, Vol. 6, 123 53

Tajima, T., Sakai, J., Nakajima, H., et al. 1987, *Astrophysical Journal*, 321, 1031 35

Tan, B., Zhang, Y., Tan, C., & Liu, Y. 2010, The Astrophysical Journal, 723, 25 34

The SunPy Community, Barnes, W. T., Bobra, M. G., et al. 2020, The Astrophysical Journal, 890, 68 124

Thomas, J. H. & Weiss, N. O. 2004, *Annual Review of Astronomy & Astrophysics*, 42, 517 5

Thompson, M. J., Christensen-Dalsgaard, J., Miesch, M. S., & Toomre, J. 2003, *Annual Review of Astronomy & Astrophysics*, 41, 599 8

Thurgood, J. O., Pontin, D. I., & McLaughlin, J. A. 2017, *Astrophysical Journal*, 844, 2 67

Torrence, C. & Compo, G. P. 1998, Bulletin of the American Meteorological Society, 79, 61 106

Turck-Chièze, S. & Couvidat, S. 2011, Reports on Progress in Physics, 74, 086901 7

Van Doorsselaere, T., Kupriyanova, E. G., & Yuan, D. 2016, *Solar Physics*, 291, 3143 33, 35

Vršnak, B., Magdalenić, J., Aurass, H., & Mann, G. 2002, *Astronomy & Astrophysics*, 396, 673 138

White, S., Benz, A., Christe, S., et al. 2011, Space Science Reviews, 159, 225 120

Wild, J. P. 1963, Radiotekhnika, 1 28

Woods, T. N., Eparvier, F. G., & Mason, J. P. 2015, Proceedings of the International Astronomical Union, 11, 27–40 78

Wu, H., Emadi, A., Graaf, G., Leijtens, J., & Wolffenbuttel, R. 2011, Procedia Engineering, 25, 527 3

Yurchyshyn, V., Yashiro, S., Abramenko, V., Wang, H., & Gopalswamy, N. 2005, The Astrophysical Journal, 619, 599 24

Zaitsev, V. & Zlotnik, E. 1986, Soviet Astronomy Letters, 12, 311 63, 64, 65, 87, 93, 94, 99, 100, 137

Zharkova, V. V. & Gordovskyy, M. 2004, *Astrophysical Journal*, 604, 884 56

Zimovets, I. V., McLaughlin, J. A., Srivastava, A. K., et al. 2021, *Space Science Reviews*, 217, 66 37, 140

Zucca, P., Carley, E. P. E. P., Bloomfield, D. S., et al. 2014, Astronomy & Astrophysics, 564, A47 87, 96, 97